ARCHITECTURAL VARIATIONS AND THEIR CONTROLS IN CARBONATE CLINOFORM SYSTEMS

A Dissertation

by

PHILIPP TESCH

Submitted to the Office of Graduate and Professional Studies of
Texas A&M University
in partial fulfillment of the requirements for the degree of

DOCTOR OF PHILOSOPHY

Chair of Committee,	Michael C. Pope
Co-Chair of Committee,	Robert S. Reece
Committee Members,	Juan Carlos Laya
	Walter B. Ayers
Head of Department,	Michael C. Pope

August 2018

Major Subject: Geology

ABSTRACT

Focus of this dissertation was to employ seismic geomorphology in the subsurface of the Browse Basin (Australia) and digital outcrop modeling in the Last Chance Canyon (New Mexico) outcrops to develop new analytical quantification and visualization techniques in the investigation of carbonate clinoform systems in 3D and 4D to extract information on the interplay of allogenic and autogenic controls that shape carbonate system architecture and evolution.

Integration of seismic geomorphology and trajectory analysis of the Oligo-Miocene distally steepened carbonate ramp system in the subsurface Browse Basin of the Northwest Shelf of Australia introduces a new way to parameterize carbonate slope channel systems and their stability. We introduce the cumulative channel cross sectional area parameter as the product of number of slope channels, slope channel depth, and slope channel width. This parameter quantifies the capability of the slope channel system to transport sediment basinward, highlights phases of autogenic slope system re-organization in response to changes in relative sea level, and can be used as a proxy for slope system stability. Introduction of our shelf break rugosity and shelf break trajectory rugosity parameters revealed the role of large-scale and intermediate scale controls on the system architecture and evolution: allogenic forcing through regional tectonics and relative sea level changes serve as main control on basin architecture and large-scale progradation and aggradation in the system. The autogenic response of the carbonate factory serves as main control on intermediate-scale and small-scale by the incision of

channels into the slope and the smoothing effect of carbonate deposition on areas that are highly rugose.

Based on our modeling results, the mixed carbonate-siliciclastic clinoform system in Last Chance Canyon, NM represents a paleo-topographic low that served as a preferential pathway for siliciclastic sediment during fifth-order relative sea level lowstands. In contrast to the traditional model of reciprocal sedimentation that infers a basin-wide carbonate factory shut-off during third-order relative sea level lowstand, we propose a modification to the reciprocal sedimentation model that integrates our outcrop observations and modeling results of the fifth-order parasequences and includes uninterrupted carbonate production in a “refugio” position, away from the avenues of sand input.

DEDICATION

To incrementalism and humility

ACKNOWLEDGEMENTS

I would like to thank my co-advisor, Dr. Mike Pope, for his trust and support to take me on as his student and to provide me the opportunity to follow my passion for carbonate sedimentology. I deeply appreciate Bobby Reece for his honest and constructive feedback, being an outstanding mentor and academic role model. Thanks go to Jim Markello for all his help in long discussions and in the field, as well as his willingness to pass on his knowledge to the next generation of geoscientists.

I want to thank Carlos Dengo for his interpersonal support and guidance. I thank Juan Carlos Laya for actively helping me to become a part of the carbonate sedimentology community and for his dedication and enthusiasm towards the field. I would also like to thank Walt Ayers for sharing his insight into a plethora of geological concepts. Special thanks go to Suzanne Rosser and Trisha Fike for their help, support, and dedication.

Thanks go to my friends, colleagues, and the department faculty and staff at the Department of Geology & Geophysics and for making my time at Texas A&M University a great experience.

I would also like to thank my undergrad professor Dr. Deutschbeg, who inspired me to pursue my graduate studies in Texas and to aim for a career in the US petroleum industry. He was an outstanding teacher but also the best role model for showing me and others how not to behave interpersonally if you want to be considered a respected mentor and colleague. More special thanks go to my high school teacher Mr. Dettman,

who always supported my endeavors and helped me lay the foundation for a successful transition into living in the US.

Finally, I want to thank my family for their love and unwavering support, for their patience when I lectured geology after an amazing field trip, for their lack of understanding why I always have to take photos of my rock hammer when I am in the field (it's for scale!), for their eventual appreciation of my late musical endeavors, for their moral support in good and bad times, and for helping me to follow my dreams and passion.

CONTRIBUTORS AND FUNDING SOURCES

Contributors

This work was supervised by a dissertation committee consisting of Professor Mike Pope [co-advisor], Professor Bobby Reece [co-advisor], and Professor Juan Carlos Laya of the Department of Geology & Geophysics and Professor Walt Ayers of the Department of Petroleum Engineering.

All work for the dissertation was completed by the student, under the advisement of Professor Mike Pope, Professor Bobby Reece, and Professor of Practice Jim Markello of the Department of Geology & Geophysics.

Funding Sources

This research was supported by multiple fellowships from the Berg-Hughes Center in the Department of Geology & Geophysics at Texas A&M University, by the Dissertation Fellowship of the Office of Graduate and Professional Studies at Texas A&M University, by the Hal S. Dean Memorial Scholarship of the West Texas Geological Society, by the Shoemaker Scholarship of the American Institute of Professional Geologists, Texas Section, by the James E. Hooks Memorial Grant of the American Association of Petroleum Geologists, by the National Scholarship of the American Institute of Professional Geologists, by the IAS Travel Grant of the International Association of Sedimentologists, and a College of Geosciences Scholarship from Texas A&M University.

TABLE OF CONTENTS

Page

ABSTRACT ii

DEDICATION iv

ACKNOWLEDGEMENTS v

CONTRIBUTORS AND FUNDING SOURCES vii

TABLE OF CONTENTS viii

LIST OF FIGURES x

LIST OF TABLES xviii

I - INTRODUCTION TO DISSERTATION 1

II - QUANTIFICATION OF ARCHITECTURAL VARIABILITY AND CONTROLS IN AN UPPER OLIGOCENE TO LOWER MIOCENE CARBONATE RAMP, BROWSE BASIN, AUSTRALIA 4

- II.1 Synopsis 4
- II.2 Introduction 5
- II.3 Geological Setting 7
- II.4 Data 11
  - II.4.1 3D Seismic Data 11
  - II.4.2 Well Data and Stratigraphy 12
- II.5 Results 14
  - II.5.1 Seismic Sequences 14
  - II.5.2 Seismic Stratigraphy 18
  - II.5.3 Depositional Slope Angles and Slope Channels 25
  - II.5.4 Progradation and Aggradation 32
  - II.5.5. Seismically-Derived Subsidence Rates 37
  - II.5.6. Seismically-Derived Relative Sea Level 39
  - II.5.7. Depositional Geometries 42
- II.6. Discussion 45
  - II.6.1. Ramp Geometry Evolution 45
  - II.6.2. Seismically Derived Parameters 48
  - II.6.3. External Controls and Internal Response 52

II.7. Summary and Conclusions 58

III - MODIFICATION OF THE RECIPROCAL SEDIMENTATION MODEL IN PERMIAN UPPER SAN ANDRES MIXED CLASTIC-CARBONATE CLINOFORMS, LAST CHANCE CANYON, NM 60

III.1 Synopsis 60
III.2 Introduction 61
III.3 Geological Setting 64
III.4 Data and Methods 68
III.4.1 Stratigraphic Framework and Clinoform Definition 68
III.4.2 Photogrammetry 71
III.4.3 3D Surface Modeling and Geometric Analysis of Clinoforms 72
III.5 Results and Discussion 74
III.5.1 Clinoform Geometries 74
III.5.2 Progradation and Aggradation 78
III.5.3 Modification to the Reciprocal Sedimentation Model 81
III.6 Summary and Conclusion 88

IV - ADDING THE MISSING THIRD AND FOURTH DIMENSIONS TO TRAJECTORY ANALYSIS IN CARBONATE SYSTEMS 90

IV.1 Synopsis 90
IV.2 Introduction 91
IV.3 Data and Methods 94
IV.3.1 Browse Basin Seismic Data 94
IV.3.2 Shelf Break Parameterization 96
IV.4 Results 103
IV.5 Discussion 109
IV.6 Summary and Conclusion 113

V – DISSERTATION SUMMARY 116

REFERENCES 120

APPENDIX A 140

APPENDIX B 145

APPENDIX C 147

LIST OF FIGURES

Page

Figure 1: Location of Browse Basin on the North West Shelf of Australia after Struckmeyer et al. (1998). Note the location of the Brecknock South 3D seismic survey at the intersection of the Caswell, Barcoo and Seringapatam sub-basins. Offset wells B#1 = Brecknock #1 and NSR#1 = North Scott Reef #1 provided well data for stratigraphic correlations (Rosleff-Soerensen et al., 2012; Woodside Energy, 2007). Regional bathymetric contours (GEBCO_2014) in meters below sea level (mbsl) are displayed on an ESRI National Geographic Basemap and indicate the present-day southwest-northeast strike of the shelf. 9

Figure 2: Geological composite chart of the Cenozoic in the Browse Basin. The study interval covers the Oligocene through Lower Miocene. During the Upper Eocene, a major change in depositional environments occurred in the study area with a shift from siliciclastic-dominated to carbonate-dominated. Extent and duration of the Paleocene-Eocene and Eocene-Oligocene unconformities vary throughout the basin and are only approximated in the figure. The tectonic regime transitioned from low-rate thermal subsidence to increased-rate foreland loading due to the collision of the Australian plate with the Banda Arc and development of the Timor Trough in the Oligocene. Beginning in the Oligocene, Arctic and Antarctic ice sheets established. 10

Figure 3: Overview map of the seismic data displaying a coherency slice through the depth-migrated seismic volume at 2200 m with location of Calliance #1, #2, and #3 wells. Solid yellow lines indicate dip (Fig. 5) and strike (Fig. 7) sections. Stippled line marks the shelf edge in SW-NE orientation. Survey location shown in Fig. 1. 13

Figure 4: Use of stratal terminations to identify sequence boundaries and seismic sequences. Reflectors truncate or toplap below a sequence boundary and onlap or downlap above a sequence boundary. Seismic sequence SS7 is bound at the base by sequence boundary SB7 and bound at the top by sequence boundary SB8. 16

Figure 5: Depth migrated dip directional cross section DL5 (see Fig. 3 for location). A – uninterpreted seismic section. B – interpreted seismic section with the 12 identified seismic sequences (SS1-12) and 13 sequence boundaries (SB1-13) from the Eocene through Lower Miocene in yellow. Triangles = shelf break; circles = toe of slope. 3x vertical exaggeration. The study interval comprises the distally steepened carbonate ramp phase from the Oligocene through Lower Miocene. The Paleocene-Eocene unconformity

marks the transition from underlying fluvio-deltaic clastic deposits to overlying carbonate dominated deposits. Middle Miocene reef complexes overlie the ramp and are capped by Pliocene to Recent hemipelagic carbonate deposits. 17

Figure 6: Overview of main seismic reflector geometries in the dataset. A – parallel and sub-horizontal reflectors typically occur on the shelf; B – oblique reflectors are common along the shelf, truncations by an overlying reflector indicate a sequence boundary; C – chaotic reflectors occur in basinal settings, near the toe of slope; D – large-scale sigmoidal reflectors are characteristic of prograding clinoforms; E – convergent reflectors occur at the transition from shelf to slope. 3x vertical exaggeration. 19

Figure 7: Strike directional cross section through the seismic data (see Fig. 3 for location). A - uninterpreted section. B - Interpreted section. Reflector geometries are determined by their position along the depositional profile: shelf reflectors are sub-parallel and horizontal; slope reflectors are u-shaped, truncate underlying reflectors and are either vertically stacked or filled with onlapping reflectors; basinal reflectors are rugose. 3x vertical exaggeration. 20

Figure 8: Depth-converted horizon slices of sequence boundaries SB5 (A) and SB6 (B) visualizing the transition from slope system phase I (SB5) to phase II (SB6). This transition is characterized by a distinct increase in the total number of slope channels from three to fourteen, average slope angles greater than 9°, and a decrease in average channel width from 1,100 m to 375 m. Slope channels are readily identifiable along the slope and more elusive basinward due to decreased seismic reflector continuity. Vertical offset along minor slope faults is few decameters. 21

Figure 9: Schematic dip section of clinoforms and their geomorphic parameters for calculation of slope angles, progradation, and aggradation. In the dataset, reflectors on the shelf are usually inclined less than 2°. The marked increase in reflector dip from less than 2° landward to more than 6° along the slope marks the position of the shelf break or ramp margin. A transition of reflector dip from more than 6° along the slope to less than 3° in the basin marks the toe of slope. Slope angles were measured as the dip of a straight line from shelf break to toe of slope. The basinward shift of the ramp margin between two sequence boundaries quantifies progradation. The vertical difference in ramp margin position between two sequence boundaries quantifies aggradation. 26

Figure 10: Average slope angles for seismic sequences SS3-12 measured on depth converted seismic as inclination from shelf edge to toe of slope. Error bars

are the maximum and minimum slope angles along strike for each sequence, respectively. Minimum slope angles for seismic sequences 5 and 11 and maximum slope angles for seismic sequences 7 and 9 coincide with average values. Horizontal black line marks a critical slope angle of 10 degrees. Average slope angles in excess of 10 degrees occur between SS5&6 and SS9&10 (yellow boxes) and coincide with a re-organization in slope channel properties (Fig. 11). 28

Figure 11: Compilation of channel properties for seismic sequences SS3-12. Yellow boxes mark the re-organization of the slope channel system between phases I, II, and III. Channel properties were identified from multiple strike directional seismic cross sections and 3D seismic surfaces. A – Average number of slope channels per seismic sequence. SS6 marks a distinct transition in channel properties to an overall increased number of slope channels. B – Average depth and width of slope channels per seismic sequence. SS6 marks a distinct drop in average channel width. C - Cumulative channel cross sectional area (CCCSA) per seismic sequence. CCCSA is a measure of the average available area of the channel system for basinward sediment transport. When CCCSA falls to about 50,000 m^2 and subsequently increased drastically (e.g. during SS5-SS6 and SS9-SS10; black arrows), the slope system established more channels in the subsequent seismic sequence. Therefore, we consider CCCSA a measure of slope system stability. D - Cross-plot of average channel width and depth against total number of channels. The falling trendline with an R^2 value of 0.74 indicates an inverse relationship between total number of channels and channel width. Channel depth correlates poorly with number of channels ($R^2 = 0.12$). Note the separation between the cluster of deep and wide channels (left half) vs shallower and narrower channels (right half). 30

Figure 12: Progradation and aggradation behavior of the shelf edge during seismic sequences SS4-12 derived from depth converted seismic volume. A – Individual dip line aggradation (IDA) amplitude of vertical component of shelf edge trajectory for all ten dip lines DL1-10 (colored curves) and their system average aggradation (SAA; bold black curve). Values above 0 represent aggradation, values below 0 represent downstepping. B – Individual dip line progradation (IDP) amplitude of lateral component of shelf edge trajectory for all ten dip lines DL1-10 (colored curves) and their system average progradation (SAP; bold black curve). Values above 0 represent progradation, values below 0 represent retrogradation. C&D – internal IDA and IDP amplitude variation is a measure of how uniformly the shelf edge aggrades and progrades along strike. Note that the system experienced high lateral variability between SS5-6 and SS9-10, as denoted by coincident out of phase behavior of IDA and IDP amplitude and high internal IDA and IDP amplitude variation (yellow boxes). E - System

average aggradation (SAA) plotted against system average progradation (SAP). The falling trendline with an R2 value of 0.54 indicates an inverse relationship between progradation and aggradation. 36

Figure 13: Cumulative aggradation for seismic sequences SS4-12 along dip lines DL1-10 from vertical component of shelf edge trajectory as proxy for basement subsidence. DL 1-10 = values for dip directional cross sections; AVG = average of all ten dip directional cross sections. Vertical black line marks the transition from time period 1 with lower cumulative aggradation of 19 m/Myr during SS2-8 to time period 2 with increased cumulative aggradation of 30 m/Myr during SS8-12. This corresponds to the transition from Early Tertiary thermal subsidence to Late Tertiary foreland loading (Fig. 17). 38

Figure 14: Seismically-derived relative sea level curve for seismic sequences SS4 through SS12. The seismically-derived sea level curve is derived from the aggradational component of the ramp margin trajectory (Fig. 12) under consideration of basement subsidence for the Oligocene and Lower Miocene (Fig. 2). Phases of sea level rise during SS5 through SS6 and SS8 through SS11 are highlighted by the yellow boxes. 41

Figure 15: Isopach maps for seismic sequences SS5 and SS6. Low slope angles during SS5 coincide with thick, more laterally continuous slope deposits. Subsequent steepening of slope angles beyond 9° during SS6 (Fig. 10) initiates slope channel incision. Slope channel incision during SS6 partitioned the line source and decreased the amount of sediment deposited along the slope due to erosion and basinward sediment transport.....43

Figure 16: Thickness profile, not a Wheeler diagram, of seismic sequences SS3-12, illustrating sediment thickness variability for each sequence from the shelf into the basin. Profile is derived from reflector geometries in dip sectional profile DL5 (Fig. 5). Note that the lower boundary of the overlying sequence is the same as the upper boundary of the underlying sequence, e.g. base of SS12 = SB12 = top of SS11. Shelfal deposits are relatively thin compared to deposits along the slope and the basin. The northwest shift of facies in the seismic sequences indicates the progradation of the carbonate ramp through time.....44

Figure 17: Composite results of seismically derived sea level and subsidence signals compared to reference data from the literature for the Upper Oligocene through Lower Miocene. A – seismically derived sea level curve in black with stippled gray uncertainty envelope (this study), regional reference curve in red (Woodside Energy, 2007) and eustatic sea level curve in blue (Haq et al., 1987). The correlation coefficient between our seismically-

derived relative sea level curve and the regional reference curve is 0.81. The seismically derived sea level curve has a lower frequency and amplitude than the reference curves but captures the major sea level rise and fall trends of the regional reference curve. Uncertainty envelope is derived from strike directional variability of the seismically derived sea level curve. B – Browse Basin subsidence with 28 Ma marking the transition from Early Tertiary thermal subsidence to Late Tertiary foreland loading, modified from Kennard et al. (2003). Grey curve = basement subsidence after Kennard et al. (2003); black curve = inferred basement subsidence from cumulative aggradation (this study). TS = thermal subsidence, FL = foreland loading. Good match between inferred subsidence from seismic and the reference curve indicates a good preservation of the subsidence signal in the data and a strong impact of the basement subsidence signal on the system geometries. 51

Figure 18: Base map of the Last Chance Canyon study area in southeast New Mexico with outline of photogrammetry data coverage, location of strike and dip profiles (yellow lines), measured sections from Sonnenfeld (1991), and measured sections from this study as ground truth for the reconstruction of 3D clinoform geometries. 65

Figure 19: Paleogeographic map of the Permian Basin (modified from Sarg et al., 1999). The study area of Last Chance Canyon is located on the Northwest Shelf of the Delaware Basin in a shallow marine depositional environment. .. 66

Figure 20: Stratigraphic framework of the Upper San Andres Formation in the Permian Basin (after Sonnenfeld and Cross, 1993; Kerans and Kempter, 2002). Note that the San Andres Fm age boundaries are approximated due to a lack of high-resolution age constraints. 67

Figure 21: Simplified dip profile through the prograding mixed carbonate-siliciclastic clinoforms in Last Chance Canyon (modified from Sarg et al., 1997; original cross section by Sonnenfeld, 1991). The individual clinoforms represent 5th-order parasequences of the Upper San Andres Formation. 70

Figure 22: Reconstructed clinoform geometries indicate a large-scale paleo-topographic low that served as preferential sediment pathway for siliciclastic units during fifth-order relative sea level lowstands in the study area. A) Dip profile through LCC hung on the base of the Hayes sandstone as datum and showing the facies partitioning between carbonate topsets and siliciclastic bottomsets with sand-on-sand contacts in our model. 5x vertical exaggeration. B) Strike section through LCC with the Hayes sandstone as datum, showing the trough geometry of clinoforms with siliciclastic fill onlapping the flanks of the chute in our model. 5x vertical exaggeration. C)

3D reconstruction of top Clinoform 3 with a scoop-shaped geometry; clinoform height contour interval = 10 m; present day surface elevation contour interval = 20 m.....76

Figure 23: Comparison of clinoform slope angles from this study (black) and Sonnenfeld & Cross (1993; gray). The range of the upper (max) and lower (min) horizontal bars indicates the along-strike variability of slope angles within the individual clinoforms. Note the systematically increasing slope angles from the MFS to Top Clinoform C6.....77

Figure 24: Clinoform progradation and aggradation from this study (in black) calculated along ten dip profiles to visualize the lateral variability. Sonnenfeld & Cross (1993) progradation and aggradation rates (in gray) were derived from their projected 2D dip profile.....79

Figure 25: Strike-parallel view of Panorama Point location in the photogrammetry-derived high-resolution digital elevation model. A) Uninterpreted view. B) Interpreted channel geometries and clinoform contacts on the canyon wall. These intermediate-scale channels are located on the upper slope, just below the clinoform rollover. Strike-oriented outcrop cuts of the slope channels have a width of up to 370 m and a depth of up to 25 m. 80

Figure 26: Example of inherited topography and evidence of the large-scale chute in Last Chance Canyon being a paleo-topographic low for preferred siliciclastic bypass. A) Thickness map of the “Lower Gray Sand” below the third-order maximum flooding surface (re-drawn from Sarg et al., 1997). CI = 1 m. B) Clinoform 5 sand thickness. CI = 3 m. The axes of both sand bodies are parallel to depositional dip (WNW-ESE) as indicator for inherited topography.....83

Figure 27: Strike section of LCC indicating thinning and pinch-out of siliciclastic facies towards west-southwest (modified from Sarg et al., 1997, Fig. 3-IV-3).....84

Figure 28: Proposed depositional model of the greater Last Chance Canyon area in oblique view and with dip profile through the axis of the large-scale LCC chute. A) Carbonate-dominated shelf with laterally continuous carbonate factory during HST with antecedent topography of LCC in the axis of a reentrant. B) Incision of siliciclastics into the carbonate factory and preferred basinward sand transport through the large-scale LCC chute with development of basinal siliciclastic lobes during LST, and lateral and downward migration of the carbonate factory into "refugio" position. C) Backfill and onlapping of siliciclastic deposits during TST, lateral and upward migration of the carbonate factory filling the paleo-topographic low of LCC from the chute flanks. 87

Figure 29: Location of Browse Basin on the North West Shelf of Australia with location of the Brecknock South 3D Seismic Survey in red (from Tesch et al., 2018). 95

Figure 30: Block diagram illustrating the three-dimensionality of clinoform shelf breaks and shelf break trajectories (SBT). X vs. Y map view visualizes the shelf break evolution through time and along strike. Shelf break trajectories are calculated as the difference in Y values between two successive shelf breaks to quantify the rugosity or along-strike variability in progradation and aggradation of the margin between consecutive time intervals A and B. Y vs. Z side view represents a dip profile and depicts the s- or z-shaped geometry of clinoforms. We collapsed 3D shelf breaks onto the Y vs. Z plane (e.g. Fig. 6) as another way to visualize lateral and vertical variability in the shelf break. This provides a detailed insight into 3D shelf break complexity, unlike traditional 2D profiles. 97

Figure 31: Map view of interpreted shelf break SB3. A – original shelf break orientation with average strike direction of 31.7 degrees. B – shelf break rotated by 58.3 degrees to align mean strike line in a horizontal direction. This rotation simplifies the calculation of progradation relative to a previous position in x/y space. C – shelf break binned laterally into 200 bins of 50 m size covering the full 10 km transect to ensure a normalized sampling rate along the profile. 98

Figure 32: A) Map view of two successive shelf breaks (shelf break A and Shelf break B). B) Shelf break B with visualized mean Y value ($\bar{Y}$) and shelf break rugosity (RSB) as average deviation from the mean line. C) Map view of shelf break trajectory between shelf break A and shelf break B. D) Shelf break trajectory A-B with visualized mean Y value and shelf break trajectory rugosity (RSBT). 102

Figure 33: Average strike direction of shelf breaks SB3 to SB12 progressively decreased from ~60° to ~55°. We attribute the progressive shift in average strike direction to allogenic tectonic forcing from the collision of Australia with the Timor Plate and resulting differential subsidence in the Browse Basin during the Oligo-Miocene. 104

Figure 34: SB and SBT diagrams with error bars indicate basinward and vertical minimum and maximum values. Shorter error bars indicate lower rugosity. A) Side-view (Y vs Z) of the ten shelf break positions SB3 to SB 12 through time. B) Side-view (Y vs Z) of the nine shelf break trajectories SBT 3-4 to SBT 11-12. The 0, 0 coordinate origin designates the position of the previous shelf break for each of the shelf break trajectories. Quadrant designate: I – progradation and aggradation; II – retrogradation and

aggradation; III – retrogradation and downstepping; IV – progradation and downstepping. If the error bars are crossing sector boundaries, contradictory along-strike stratal stacking patterns can be expected. 105

Figure 35: Map view of shelf break trajectories color coded by aggradation (blue) and downstepping (red). Dashed horizontal lines mark the approximate progradation distance at which the shelf break trajectory transitions from aggrading to downstepping. Solid horizontal line marks the zero progradation line. Shelf break trajectories with relatively low progradation tend to be almost entirely aggradational (e.g. B, G, I); some shelf break trajectories display concurrent progradation and retrogradation (e.g. C and G); in general, a divide between aggradational (blue) and downstepping (red) data points in the shelf break trajectories occurs at progradation values of ~900 - 1,500 (e.g. A, D, E, F). 107

Figure 36: The rugosity value of all shelf breaks and shelf break trajectories ranges between 250 – 100m. 108

Figure 37: Map view and seismic dip lines visualizing differential progradation of SBT7-8 along bin 60 and bin 100 (= 2 km lateral separation). A) Map view of SB7 and SB8. B) Map view of SBT 7-8 color-coded for aggradation (blue) and downstepping (red). C) Uninterpreted depth-converted seismic dip line along bin 60. Vertical exaggeration = 3x. D) Uninterpreted depth-converted seismic dip line along bin 100. E) Interpreted depth-converted seismic dip line along bin 60 with shelf breaks SB7 and SB8, indicating an aggrading shelf break trajectory with minor progradation. F) Interpreted depth-converted seismic dip line along bin 100 with shelf breaks SB7 and SB8, indicating a prograding shelf break trajectory with minor aggradation. 112

LIST OF TABLES

Page

Table 1: Overview of seismic reflector properties for the twelve seismic sequences separated into shelf, slope and basin positions. 23

I - INTRODUCTION TO DISSERTATION

Clinoforms are a record of the spatial and temporal evolution of sedimentary systems. Clinoform evolution is controlled by complex interactions between tectonics, eustasy, sediment supply, antecedent topography and climate (Henriksen et al., 2011). The resulting sedimentary system architecture physically responds to and preserves the combined signal of allogenic and autogenic controlling processes. This complex interplay of processes defines sedimentary packaging, and thus where and how much sediment is deposited and preserved in the stratigraphic record. It is this direct feedback between allogenic and autogenic controls and the system response that enables geoscientists to solve the inverse problem of extracting paleoenvironmental conditions from the rock record (Dalrymple, 2010). Therefore, quantification of system architecture, can provide an improved understanding of the individual signals of allogenic and autogenic controls. The sequence stratigraphic method, for example, uses seismic reflection terminations, reflection geometries, and stratal stacking to reconstruct depositional systems, predict lithologies (Vail et al., 1977), and make inferences on relative sea level (Mitchum et al., 1977b).

Carbonate systems are significant from an economic perspective, as they contain an estimated 60% of global oil reserves (Burchette, 2012; Choquette and Roehl, 1985). The key challenge in the study and exploitation of carbonate systems is their inherently complex porosity-permeability distribution (Burchette, 2012) in three dimensions. However, traditional 2D investigations and models yield limited insight into the

allogenic and autogenic controls that determine this porosity-permeability distribution in carbonate systems. In addition, decades of sequence stratigraphic research in a variety of depositional systems led to the development of a nomenclature that mixes observations with interpretations, which Catuneanu et al. (2009) eventually reconciled to standardize the sequence stratigraphic method. The accommodation succession method (Neal et al., 2016) and trajectory analysis (Helland-Hansen & Hampson, 2009; Henriksen *et al.*, 2009) introduce more objectivity in the analysis of clinoform systems by clearly separating observation from interpretations in using geometric relationships of strata and tracing the 2D vertical and lateral shelf break or clinoform rollover position through time to gain insight into sequence boundary formation. Although previous studies recognized along-strike variability in stacking (Wehr, 1994) and character of bounding surfaces (Martinsen and Helland-Hansen, 1995), 2D dip sections remain the leading method of interpretation in trajectory analysis (Henriksen et al., 2009) and few studies quantified the effect of along-strike variability on interpreted systems tracts and rollover trajectories in 3D (e.g. Gill and Cobban, 1973; Helland-Hansen and Hampson, 2009; Madof et al., 2016).

Goal of this dissertation was to gain new insight and understanding of carbonate system architecture and paleo-environmental controls by developing improved quantification and visualization methods in 3D and 4D for field data in outcrops and for seismic data in the subsurface. To this end, we investigated two carbonate systems in the subsurface of Western Australia and in outcrops in New Mexico. We chose two study areas that would allow us to reveal insight into carbonate clinoform systems in different

spatial and temporal scales: In the 3D seismic volume of the Browse Basin (Western Australia), we investigated 12 third-order depositional sequences on a large to intermediate scale (287 km^2) in the Oligo-Miocene interval. In contrast, the outcrops in Last Chance Canyon (New Mexico) enabled us to study seven fifth-order parasequences on an intermediate to small scale (2 mi^2) of Late Paleozoic (Guadalupian) age. Developing new 3D and 4D quantification and visualization methods, we met our research goal and achieved to: 1) introduce a modification to the reciprocal sedimentation model in Last Chance Canyon, NM; 2) develop a new parameter to identify stages of autogenic slope system re-organization in the Browse Basin; and 3) develop new parameters and a workflow to quantify 3D and 4D lateral shelf break variability in clinoform systems.

II - QUANTIFICATION OF ARCHITECTURAL VARIABILITY AND CONTROLS IN AN UPPER OLIGOCENE TO LOWER MIOCENE CARBONATE RAMP, BROWSE BASIN, AUSTRALIA[1]

II.1 Synopsis

Integration of seismic geomorphology and trajectory analysis of the Oligocene through Lower Miocene distally-steepened carbonate ramp system in the subsurface Browse Basin of the Northwest Shelf of Australia introduces a new way to parameterize carbonate slope channel systems and their stability, and sheds light on how basinward sediment transport is influenced by allogenic and autogenic controls. Seismic geomorphologic analysis identified large-scale prograding clinoforms with an extensive slope channel system and slope angles of up to 12°. Clinoforms have an average slope angle of 8°, a height of ~500 m, and prograded 9 km during the Upper Oligocene through the Lower Miocene. Relative sea level changes overprinted the effect of intermediate-scale and small-scale antecedent topography, and determined progradation, aggradation and slope angles of the system. We introduce cumulative channel cross sectional area (CCCSA) as the product of number of slope channels, slope channel depth, and slope channel width. CCCSA quantifies the capability of the slope channel

[1] Published article in the *Journal of Marine and Petroleum Geology*: Tesch, P., Reece, R., Pope, M., Markello, J. 2018. Quantification of Architectural Variability and Controls in an Upper Oligocene to Lower Miocene Carbonate Ramp, Browse Basin, Australia. Marine and Petroleum Geology. DOI: 10.1016/j.marpetgeo.2018.01.022.

system to transport sediment basinward and highlights phases of autogenic slope system re-organization in response to changes in relative sea level. Abruptly increasing values of CCCSA correlate with slope sediment bypass through the incision of new slope channels during system re-organization phases at slope angles of 10°. Thus, we propose that CCCSA can be used as a proxy for slope system stability. Incision of new slope channels into the ramp margin created strike-parallel variability of the ramp margin trajectory. Our seismically-derived relative sea level curve and subsidence rates of 9-30 m/Myr indicate a good preservation of the subsidence and sea level signal in the data.

II.2 Introduction

Clinoforms are one type of record of the spatial and temporal evolution of sedimentary systems. Their evolution is controlled by a complex interplay between tectonics, eustasy, sediment supply, antecedent topography and climate (Henriksen et al., 2011). The combined signal of allogenic and autogenic controlling processes is preserved as a physical response in the sedimentary system architecture. It is this complex interplay of processes that defines the sedimentary packaging, and thus where and how much sediment is deposited and preserved in the stratigraphic record. This direct feedback between controls and the system response enables geoscientists to solve the inverse problem of extracting paleoenvironmental conditions from the rock record (Dalrymple, 2010). The quantification of system architecture, therefore, can provide a better understanding of the individual signals of allogenic and autogenic controls.

Geomorphometry is the quantitative description of landforms, their processes, geometries and sediments at the Earth's surface. It is used to derive parameters about slope and curvature and to extract information about morphometric features (Pike et al., 2009; Pike, 2000). In modern depositional environments, geomorphometry is used to quantitatively describe and understand sedimentologic feedbacks. Seismic geomorphology is the application of this approach to extract geomorphic insights using dominantly 3D seismic data. The petroleum industry extensively uses 3D seismic data to identify geobodies, such as channels, mounds etc., and to identify prospective drilling targets (Posamentier et al., 2007).

The well imaged subsurface clinoforms of the Oligocene – Miocene carbonate ramp system of the Australian North West Shelf (NWS) were previously studied to investigate their evolution and controls in the Carnarvon Basin (e.g. Cathro and Austin, 2001; Cathro et al., 2003). Research on the evolution of the overlying Middle – Late Miocene carbonate shelf in the adjacent Browse Basin utilized high-resolution seismic geomorphology, lithological information from well logs, sidewall cores, ditch cuttings, stable isotope ($\delta^{18}O$, $\delta^{13}C$) data, and Rb/Sr age-dating methods to reconstruct the paleo-environmental changes in the Browse Basin during the Miocene (Rosleff-Soerensen et al., 2012).

This study presents novel techniques to quantitatively resolve geometries, along-strike variability, and to delineate paleoenvironmental signals of the Oligocene – Lower Miocene carbonate ramp system in the Browse Basin. Use of 3D seismic data allows for determination of lateral variability, thereby, reducing the lateral bias and uncertainty of

2D studies. Calculated 3D progradation and sedimentation rates are a better representation of the actual system behavior than their 2D counterparts. This study describes how we reconstructed the signals of tectonics and relative sea level from 3D seismic data. We quantify how relative sea level changes influenced progradation and aggradation in the system. Furthermore, we delineate the interaction between relative sea level and the slope system to show how lateral variability in the ramp margin trajectory evolves.

II.3 Geological Setting

The Browse Basin (Fig. 1) is part of the Westralian Superbasin (Yeates et al., 1987) that comprises the Carnarvon, Canning, Browse and Bonaparte Basins (Stephenson and Cadman, 1994) on the Australian North West Shelf (NWS). A significant amount of fluvio-deltaic siliciclastic, passive margin sediments accumulated in the Browse Basin (Woodside Energy, 2007, 2008, 2009) during a prolonged period of little or no tectonic activity in the Cretaceous (Apthorpe, 1988). Basin sedimentation changed from siliciclastic to carbonate-dominated in the Eocene (Apthorpe, 1988; Stephenson and Cadman, 1994). During the Paleocene – Eocene (Fig. 2), the NWS of Australia migrated north from 40° S to 32° S, into climatic conditions more favorable for carbonate systems (McGowran et al., 2004). A non-tropical, heterozoan carbonate ramp developed during the Eocene-Oligocene, overlying Paleocene and older siliciclastic strata (Reuning et al., 2009; Rosleff-Soerensen et al., 2012). Foreland loading related to the collision of the Australian plate with the Banda Arc and development of the Timor

Trough caused increased basement subsidence beginning in the late Oligocene, and resulting in minor structural deformation in the study area (Baillie et al., 1994; Kennard et al., 2003). The Australian NWS shifted farther north from 30°S to 25°S during the Oligocene-Miocene (McGowran et al., 2004), and a warm climatic optimum was reached by the Middle Miocene (Feary and James, 1995; Savin et al., 1985; Tripati et al., 2009).

The transition into a tropical photozoan rimmed shelf occurred at the time of transition from Early to Middle Miocene, and is associated with a eustatic sea level fall (Reuning et al., 2009). The Browse Basin Middle Miocene barrier reefs, patch reefs and atolls drowned during the Early Tortonian relative sea level rise associated with the collision of the Australian Plate with the Banda Arc (Baillie et al., 1994; Stephenson and Cadman, 1994; Willis, 1988). This drowning event initiated the transition to Late Miocene-Recent hemipelagic carbonate sedimentation across the NWS (Rosleff-Soerensen et al., 2012).

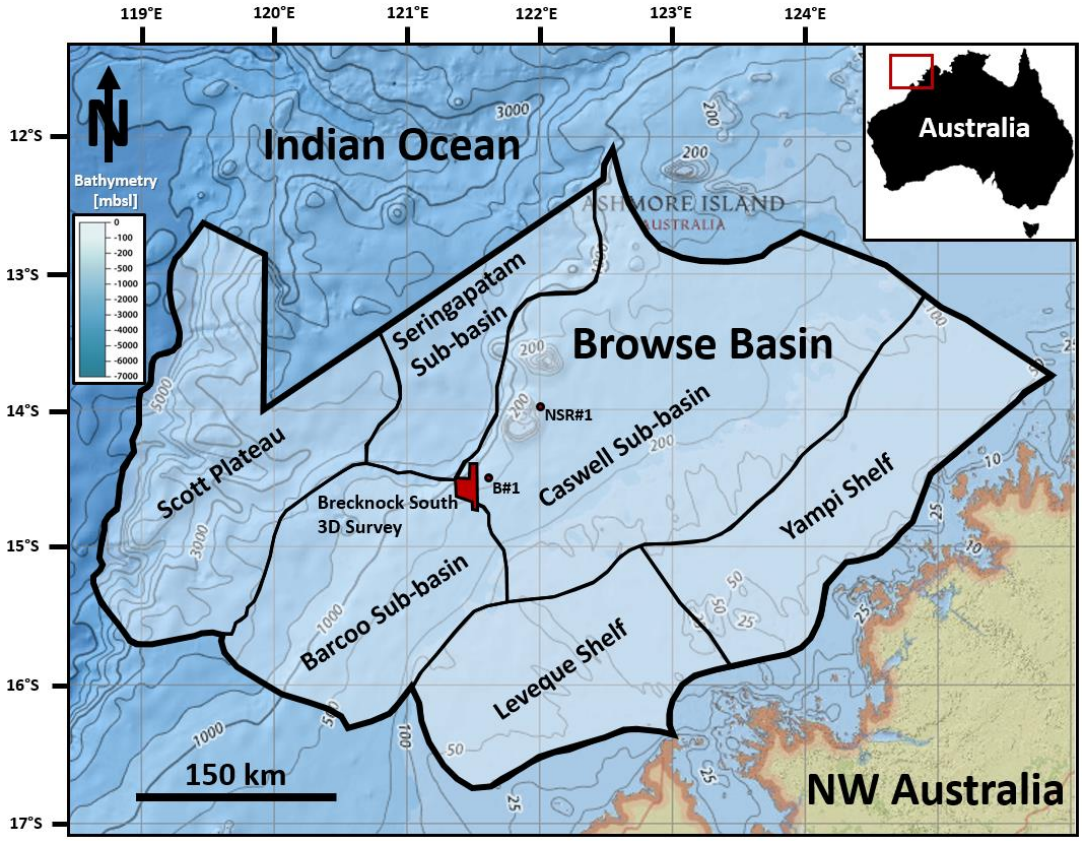

Figure 1: Location of Browse Basin on the North West Shelf of Australia after Struckmeyer et al. (1998). Note the location of the Brecknock South 3D seismic survey at the intersection of the Caswell, Barcoo and Seringapatam sub-basins. Offset wells B#1 = Brecknock #1 and NSR#1 = North Scott Reef #1 provided well data for stratigraphic correlations (Rosleff-Soerensen et al., 2012; Woodside Energy, 2007). Regional bathymetric contours (GEBCO_2014) in meters below sea level (mbsl) are displayed on an ESRI National Geographic Basemap and indicate the present-day southwest-northeast strike of the shelf.

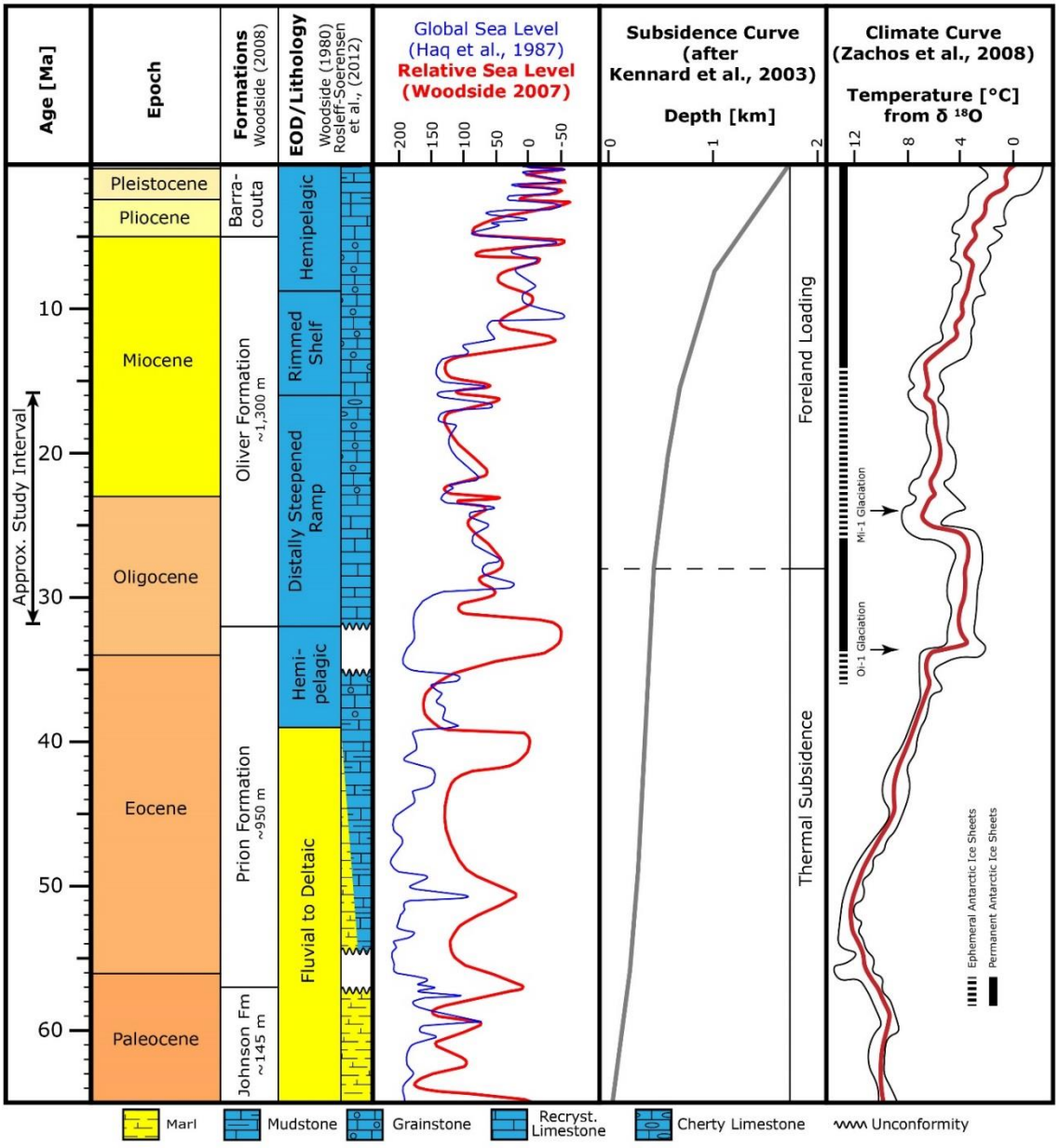

Figure 2: Geological composite chart of the Cenozoic in the Browse Basin. The study interval covers the Oligocene through Lower Miocene. During the Upper Eocene, a major change in depositional environments occurred in the study area with a shift from siliciclastic-dominated to carbonate-dominated. Extent and duration of the Paleocene-Eocene and Eocene-Oligocene unconformities vary throughout the basin and are only approximated in the figure. The tectonic regime transitioned from low-rate thermal subsidence to increased-rate foreland loading due to the collision of the Australian plate with the Banda Arc and development of the Timor Trough in the Oligocene. Beginning in the Oligocene, Arctic and Antarctic ice sheets established.

Lithologies of Eocene through Early Miocene strata are partly calcisiltic grainstone with 95-98 % carbonate content of dominantly low-Mg calcite and no aragonite or high-Mg calcite. Planktonic foraminifera were abundant during the Eocene and the clay mineral content of lithologies is 5-15 % with trace amounts of chert and Gamma Ray (GR) readings between 20-40 API. In the Oligocene through Lower Miocene interval, benthic foraminifera were abundant and the clay mineral content decreases to less than 5 % and GR readings are less than 20 API. Lithologically, this interval is dominated by strongly re-crystallized limestone with up to 25 % carbonate mudstone that can have up to 5 % vuggy porosity (Rosleff-Soerensen et al., 2012).

II.4 Data

II.4.1 3D Seismic Data

We utilized the Brecknock South 3D Marine Seismic Survey for this study, which is available through the Geoscience Australia *Western Australian Petroleum and Geothermal Information Management System* (WAPIMS), a commercial petroleum exploration database. Baker Hughes and Western Geophysical acquired the 287.3 km^2 multichannel survey in the southeastern part of the Caswell sub-basin in the Browse Basin on the NWS of Australia (Figs. 1 and 3) for Woodside Energy (Western Geophysical, 1999). The seismic data are time-migrated, zero-phase and follow SEG European polarity (Veritas, 2000). Rosleff-Soerensen et al. (2012) used this dataset in combination with the adjacent Brecknock 3D Marine Seismic Survey for the seismic geomorphology study of the overlying Miocene rimmed shelf succession.

We created synthetic seismograms using DT and GR logs from the Calliance #1, #2, and #3 wells to tie the Oligocene – Miocene boundary encountered in the wells to the corresponding reflector in the 3D seismic volume. In order to measure slope angles, we performed a time-depth conversion of the seismic data. For the time-depth conversion, we created a laterally homogeneous velocity model based on the time-depth relationship of the Calliance #3 well. The final depth converted seismic volume places the Oligocene-Miocene boundary along the Calliance #1 and #2 well paths within +/- 75 m of their reported depths (~2,150 m) encountered in the wells (Woodside Energy, 2007, 2008). We recognize that the laterally homogeneous velocity model introduces uncertainty to geometries in the depth domain, affecting calculated dip angles. Slope angle measurements vary less than 1° with the use of velocity models based on time-depth relationships of the Calliance #1 and #2 wells. The limits of vertical and horizontal resolution at the Oligocene-Miocene boundary are ~15 m and ~30 m, respectively.

II.4.2 Well Data and Stratigraphy

Woodside Energy drilled three wells in the area of the Brecknock South 3D seismic survey (Figs. 1 and 3): Calliance Well #1 (2005), Well #2 (2007), and Well #3 (2008). The wells targeted fluvial to deltaic sandstone reservoirs in the Jurassic Plover Formation (Woodside Energy, 2007, 2008, 2009). For our seismic well tie and the petrophysical characterization of Eocene through Lower Miocene strata, we downloaded gamma ray (GR), resistivity (RES) and compressional slowness (DT) well logs of the Calliance Wells #1, #2, and #3 from WAPIMS.

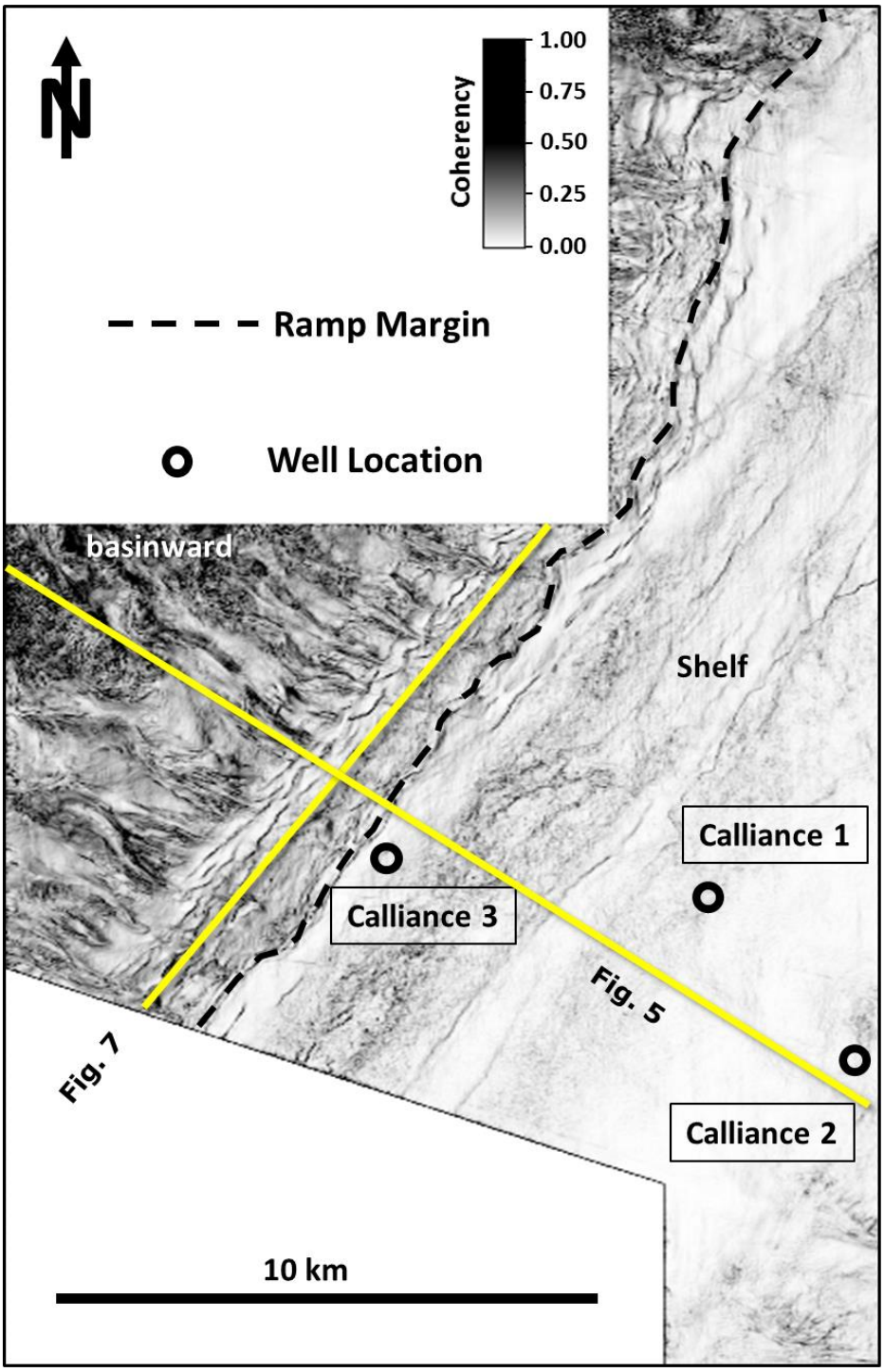

Figure 3: Overview map of the seismic data displaying a coherency slice through the depth-migrated seismic volume at 2200 m with location of Calliance #1, #2, and #3 wells. Solid yellow lines indicate dip (Fig. 5) and strike (Fig. 7) sections. Stippled line marks the shelf edge in SW-NE orientation. Survey location shown in Fig. 1.

Previous workers inferred Cenozoic stratigraphic subdivisions using regional seismic reflector extrapolation and GR log correlation from the North Scott Reef #1 well, about 80 km NE of the study area (Woodside Energy, 2007, 2008, 2009) (Fig. 1). Rosleff-Soerensen et al. (2012) refined the subsurface stratigraphy in the Browse Basin using micropaleontological analyses and $^{87}Sr/^{86}Sr$ dating of sidewall cores and ditch cuttings from the offset Brecknock #1 well, about 10 km NE of this study area (Fig. 1). Belde et al. (2017) assigned the Top Paleocene, Top Eocene, Top Oligocene and Top Lower Miocene ages to seismic reflectors in the Brecknock survey with an accuracy of +/- 1 Myr. We used this updated subsurface stratigraphy to constrain ages of reflectors in the Browse Basin seismic data.

II.5 Results

II.5.1 Seismic Sequences

We adapted standard sequence stratigraphic analysis methods, including reflector geometries, stratal terminations, nomenclature, and hierarchical orders (Catuneanu et al., 2009; Mitchum et al., 1977a; Mitchum and Van Wagoner, 1991) to identify depositional sequences (Fig. 4). We identified thirteen medium to high amplitude, continuous reflectors that could be mapped throughout the volume. These reflectors are seismic surfaces (Bertram and Milton, 1996), and were used to define and establish relative geological age (Hart, 2013). Below each of these thirteen continuous reflectors, other reflectors toplap or truncate, and above each of these continuous reflectors, other reflectors onlap and/or downlap (Fig. 4). Therefore, the seismic surfaces represent third-

order depositional sequence boundaries (e.g. Mitchum et al., 1977a), SB1 through SB13 (Fig. 5).

These interpreted depositional sequence boundaries bound twelve seismic sequences, SS1 through SS12, that we identified in the Eocene through Lower Miocene section of the seismic data. Sequence boundary 1 (SB1) marks the base of the study interval and SB13 marks the top of the study interval. Seismic sequence 1 (SS1) is defined as the oldest and stratigraphically lowest unit, bound at the base by SB1 and at the top by SB2, and seismic sequence 12 (SS12) is defined as the youngest and stratigraphically highest unit, bound by SB12 at the base and at the top by SB13 (Fig. 5).

We assigned absolute ages to four seismic surfaces (Fig. 5a) using age constraints from previous work (Belde et al., 2017; Rosleff-Soerensen et al., 2012), following the chronostratigraphy established by Gradstein et al. (2012): Paleocene-Eocene boundary (56.0 Ma; SB1), Eocene-Oligocene boundary (33.9 Ma; SB2), Oligocene-Miocene boundary (23.0 Ma; SB8), and Lower Miocene-Middle Miocene boundary (16.0 Ma; SB13). These four seismic surfaces are described seismically, lithologically and petrophysically in more detail below.

For the nine seismic surfaces in the Oligocene and Lower Miocene sections that were not assigned an absolute age, we allocated each seismic sequence a roughly equal amount of time within the defined epoch boundaries. The Oligocene spans 10.9 Myr and contains 6 seismic sequences, thus we calculate an average time duration of ~1.8 Myr for each of seismic sequences SS2 through SS7 in the Oligocene. In the same manner, seismic sequences SS8 through SS12 of Lower Miocene age represent ~1.4 Myr for each

sequence. In addition to stratal terminations, the time duration of 1.4 – 1.8 Myr per seismic sequence conforms with the temporal magnitude of third-order depositional sequences of 1 – 10 Myr duration (Van Wagoner, 1988), and serves as another line of evidence to treating the seismic sequences as depositional sequences.

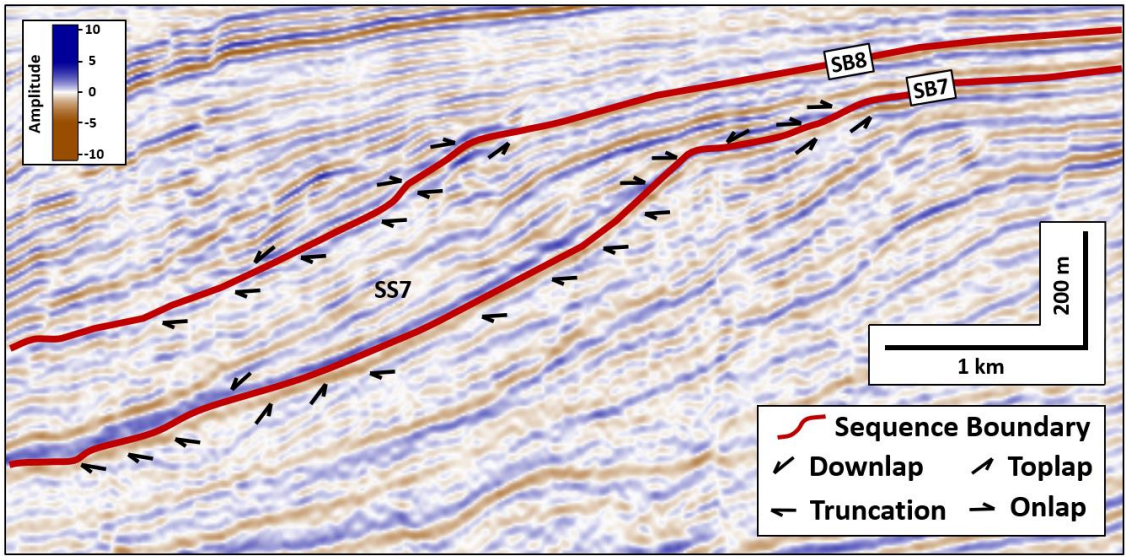

Figure 4: Use of stratal terminations to identify sequence boundaries and seismic sequences. Reflectors truncate or toplap below a sequence boundary and onlap or downlap above a sequence boundary. Seismic sequence SS7 is bound at the base by sequence boundary SB7 and bound at the top by sequence boundary SB8.

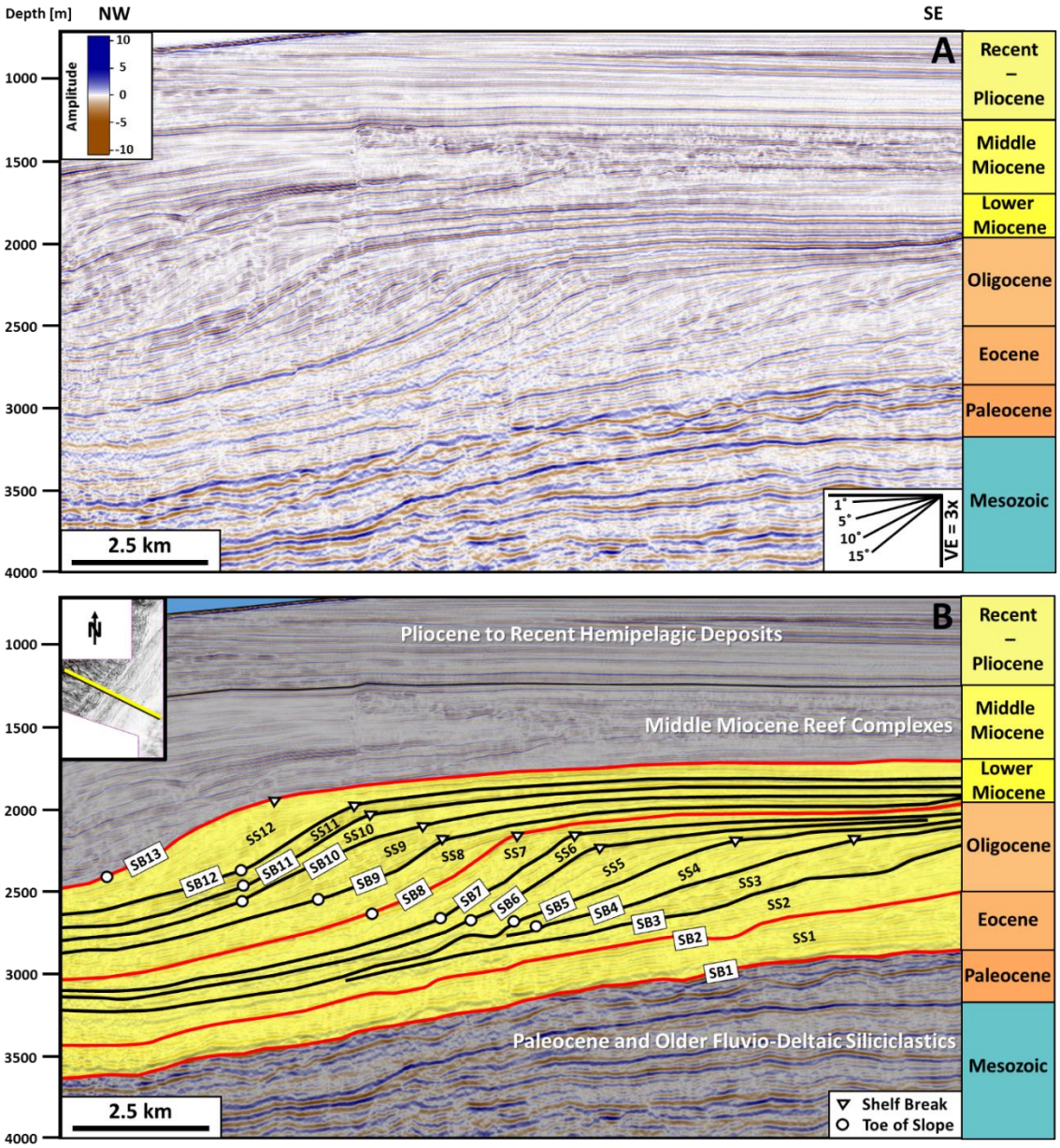

Figure 5: Depth migrated dip directional cross section DL5 (see Fig. 3 for location). A – uninterpreted seismic section. B – interpreted seismic section with the 12 identified seismic sequences (SS1-12) and 13 sequence boundaries (SB1-13) from the Eocene through Lower Miocene in yellow. Triangles = shelf break; circles = toe of slope. 3x vertical exaggeration. The study interval comprises the distally steepened carbonate ramp phase from the Oligocene through Lower Miocene. The Paleocene-Eocene unconformity marks the transition from underlying fluvio-deltaic clastic deposits to overlying carbonate dominated deposits. Middle Miocene reef complexes overlie the ramp and are capped by Pliocene to Recent hemipelagic carbonate deposits.

II.5.2 Seismic Stratigraphy

Reflector configurations that compose the seismic sequences are parallel, divergent, oblique, sigmoidal and chaotic (Fig. 6). Reflectors of the twelve seismic sequence boundaries are best expressed between the ramp margin and toe of slope. Each seismic sequence has an average of 14 internal reflectors. Along the slope, reflectors within sequences onlap the basal sequence boundary, and are truncated by the top sequence boundary (Figs. 4 and 5). Reflector amplitudes along the slope are medium to high; reflectors are continuous to semi-continuous, and express sigmoidal to divergent geometry. In strike directional cross sections of the slope, reflectors are continuous to semi-continuous and have regularly spaced "u"-shaped sections. These concave-up sections truncate underlying reflectors, are filled with bi-directionally onlapping reflectors, and are overlain by more reflectors of the same geometry (Fig. 7). We interpret these u-shaped reflectors as stacked slope channels. They range from 19-53 m in depth and 240-1,200 m in width. In 3D seismic horizon slices, we identified channels as downcutting, sinusoidal features originating at the ramp margin and extending into the basin. The extracted seismic variance attribute of the horizon slice, in combination with an adjustable artificial light source in the seismic interpretation software, highlighted geometries that aided channel identification (Fig. 8).

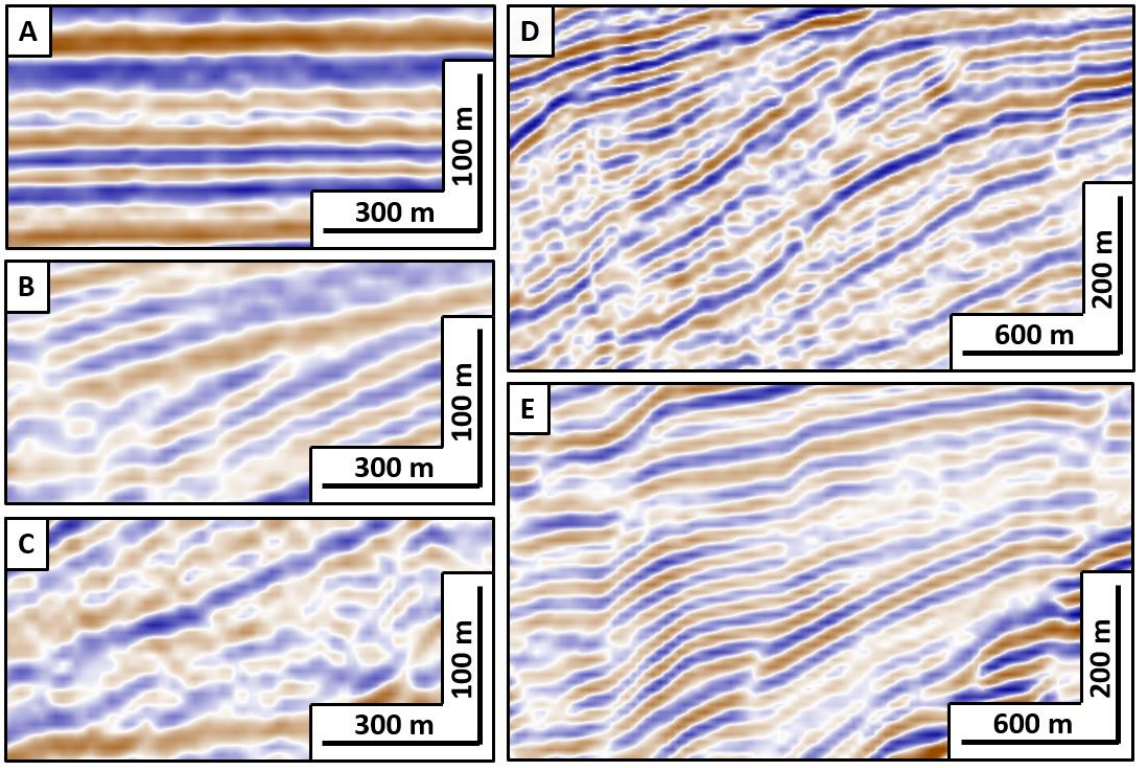

Figure 6: Overview of main seismic reflector geometries in the dataset. A – parallel and sub-horizontal reflectors typically occur on the shelf; B – oblique reflectors are common along the shelf, truncations by an overlying reflector indicate a sequence boundary; C – chaotic reflectors occur in basinal settings, near the toe of slope; D – large-scale sigmoidal reflectors are characteristic of prograding clinoforms; E – convergent reflectors occur at the transition from shelf to slope. 3x vertical exaggeration.

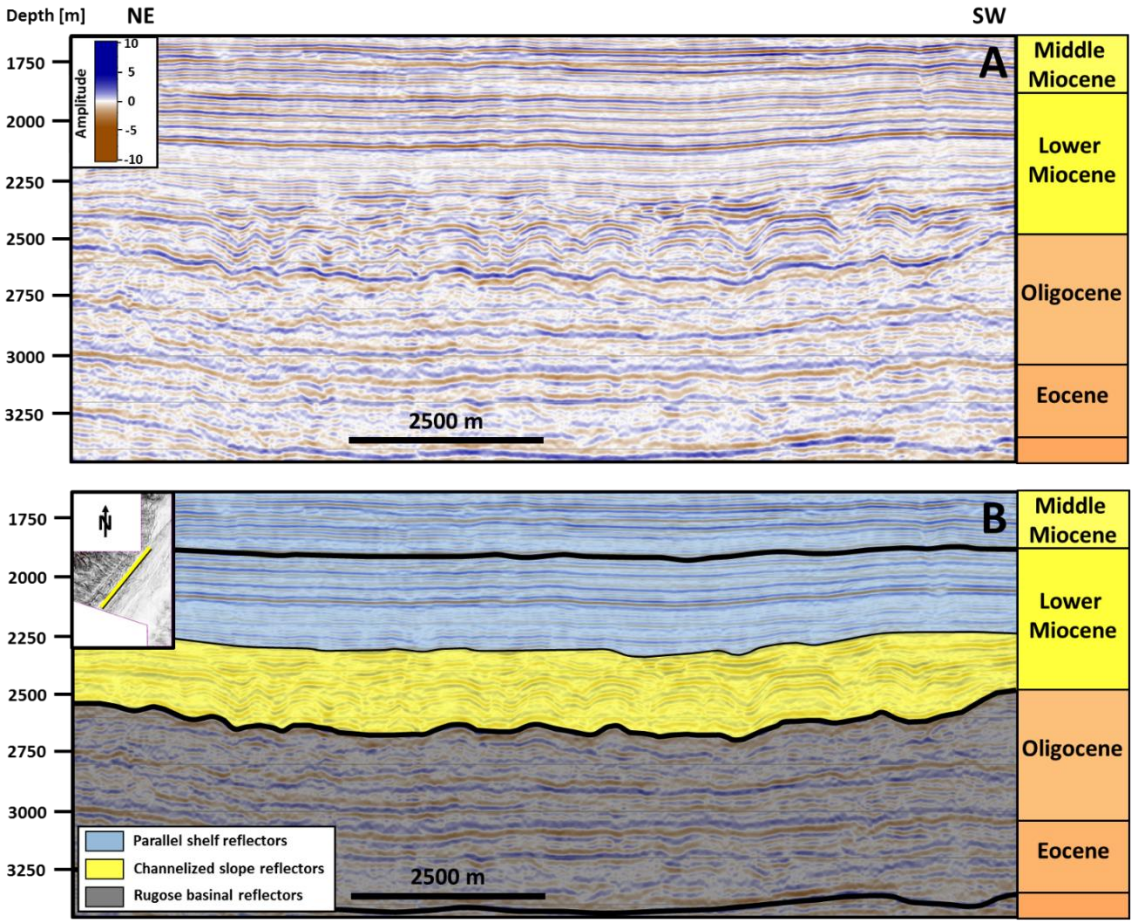

Figure 7: Strike directional cross section through the seismic data (see Fig. 3 for location). A - uninterpreted section. B - Interpreted section. Reflector geometries are determined by their position along the depositional profile: shelf reflectors are sub-parallel and horizontal; slope reflectors are u-shaped, truncate underlying reflectors and are either vertically stacked or filled with onlapping reflectors; basinal reflectors are rugose. 3x vertical exaggeration.

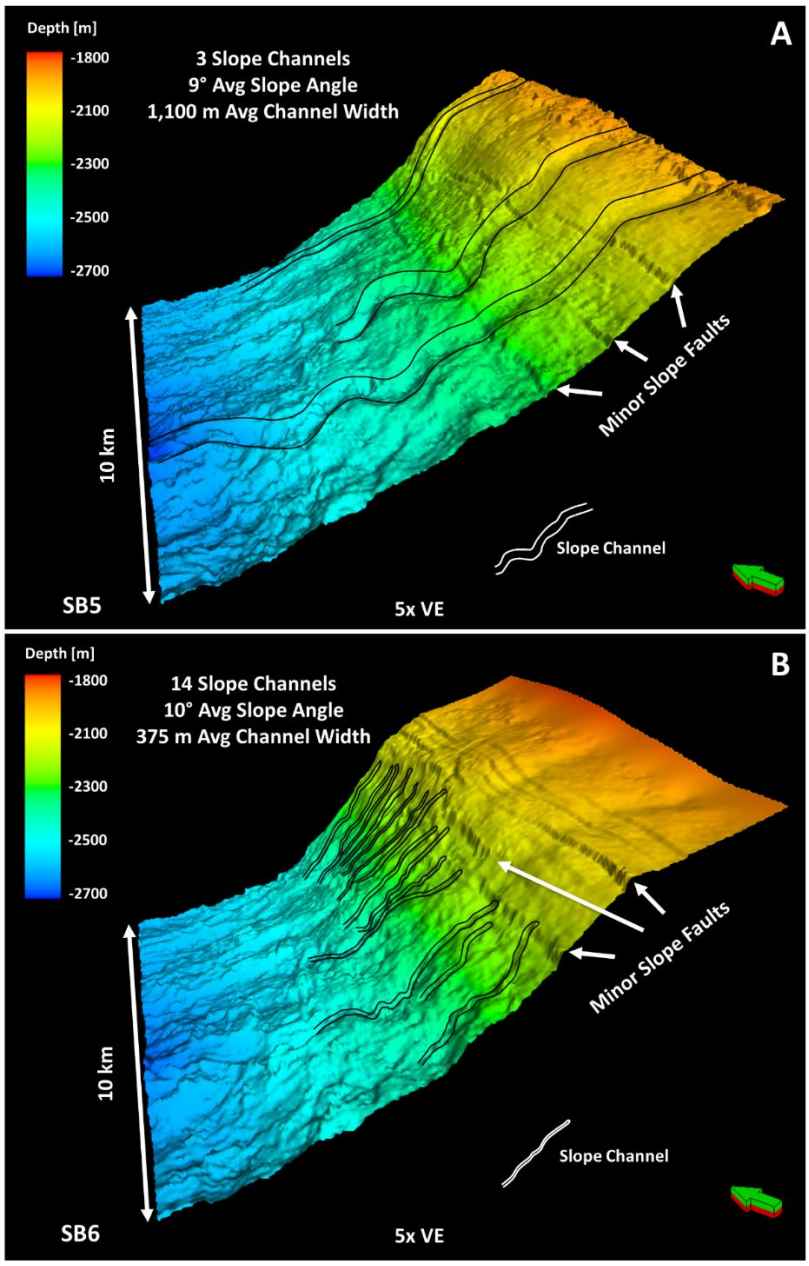

Figure 8: Depth-converted horizon slices of sequence boundaries SB5 (A) and SB6 (B) visualizing the transition from slope system phase I (SB5) to phase II (SB6). This transition is characterized by a distinct increase in the total number of slope channels from three to fourteen, average slope angles greater than 9°, and a decrease in average channel width from 1,100 m to 375 m. Slope channels are readily identifiable along the slope and more elusive basinward due to decreased seismic reflector continuity. Vertical offset along minor slope faults is few decameters.

Along the shelf break, many seismic reflectors abruptly terminate and are vertically offset in a downthrown position towards the basin. In a seismic horizon slice with the extracted variance attribute, these features are readily identifiable as shelf-parallel, low-variance features that form a sub-vertical plane or scarp (Fig. 8). We interpret these features as small-scale normal faults that are common at the ramp margin. Vertical offset of reflectors in the Oligocene through Lower Miocene interval along these faults is ~15 m. In general, slope channels originate at the small-scale fault scarps along the shelf break.

Updip, toward the shelf, reflectors onlap onto basal sequence boundaries, and decrease in number to an average of two reflectors per seismic sequence (Fig. 5). On the shelf, reflectors are high amplitude, continuous and subparallel horizontal. Downdip, toward the basin, reflectors downlap onto basal sequence boundaries, are truncated by top sequence boundaries, and decrease in number to an average of three reflectors per seismic sequence. In the basin, reflectors are medium amplitude, semi-continuous, and have wavy to chaotic geometry (Table 1).

Table 1: Overview of seismic reflector properties for the twelve seismic sequences separated into shelf, slope and basin positions.

Position	Property	SS1	SS2	SS3	SS4	SS5	SS6
Shelf	Amplitude	-	-	-	high	high	high
	Continuity	-	-	-	contiunuous	continuous	continuous
	Geometry	-	-	-	parallel sub-horizontal	parallel to convergent	convergent
Slope	Amplitude	med - high	low - med	low - high	low - med	med	low - med
	Continuity	semi-continuous	semi-continuous	semi-continuous	semi-continuous	semi-continuous	semi-continuous
	Geometry	sub-parallel inclined	sub-parallel inclined	sub-parallel to convergent	convergent to slightly chaotic	sigmoidal to slightly chaotic	sub-parallel sigmoidal
Basin	Amplitude	med - high	med	-	med	med	med
	Continuity	semi-continuous	semi-continuous	-	continuous	discontinuous	semi-continuous
	Geometry	sub-parallel to slightly chaotic	sub-parallel to slightly chaotic	-	rugose	chaotic	sub-parallel to slightly chaotic
Position	**Property**	**SS7**	**SS8**	**SS9**	**SS10**	**SS11**	**SS12**
Shelf	Amplitude	med - high	med - high	low - high	low - med	high	med - high
	Continuity	continuous	continuous	semi-continuous	semi-continuous	continuous	semi-continuous
	Geometry	parallel to convergent	parallel sub-horizontal	parallel to convergent	parallel sub-horizontal	sub-parallel to convergent	sub-parallel horizontal
Slope	Amplitude	med - high	med - high	med - high	med	high	low - med
	Continuity	semi-continuous	semi-continuous	continuous	continuous	continuous	continuous
	Geometry	sigmoidal to convergent	sigmoidal to convergent	sigmoidal to convergent	sigmoidal to slightly chaotic	parallel inclined	sigmoidal to convergent
Basin	Amplitude	low - med	med - high	low - med	med - high	high	med - high
	Continuity	semi-continuous to chaotic	semi-continuous	semi-continuous	semi-continuous	semi-continuous	semi-continuous
	Geometry	sub-parallel rugose	sub-parallel rugose	convergent to chaotic	sub-parallel to chaotic	sub-parallel rugose	sub-parallel to slightly chaotic

The Paleocene - Eocene (P-E) boundary (SB1; Fig. 5) serves as base of the study interval and represents the transition from siliciclastic-dominated shelf deposition to carbonate, cool-water, heterozoan carbonate ramp deposition (Apthorpe, 1988; Reuning et al., 2009; Rosleff-Soerensen et al., 2012) (Fig. 2). Seismically, the P-E boundary is a high amplitude, wavy, continuous trough that truncates reflectors below and is downlapped by overlying reflectors. Petrophysically, the youngest underlying Paleocene beds exhibit high GR of ~75 API and resistivity of ~4 ohm-m. This contrasts with the oldest overlying Eocene beds that have lower GR of ~45 API and lower resistivity of ~1

ohm-m. DT values for this interval were not available. The P-E boundary marks the contact between siliciclastic rocks below and carbonate rocks above (Woodside Energy, 2008). This lithological transition is seismically expressed by the truncation of underlying reflectors and the strong impedance contrast between the overlying and underlying lithologies resulting in a high amplitude reflector.

SB2, the top of SS1, represents the Eocene - Oligocene (E-O) boundary and is seismically characterized as a high-amplitude, rugose, continuous peak that truncates reflectors below and is downlapped by overlying reflectors. The peak represents the strong impedance contrast of slower, low density calcisiltic limestone above and the faster, higher density re-crystallized limestone below (Woodside, 1980). The E-O boundary records an unconformity created by a Middle Oligocene eustatic fall in sea level, resulting in basin-wide exposure of the shelf (Blevin, 1997) and concurrent erosion of the Upper Eocene and most of the Lower Oligocene strata (Woodside Energy, 2008). Thus, the seismic sequences SS2 through SS7 are Upper Oligocene strata. In the well logs, the underlying youngest Eocene beds exhibit high GR of ~50 API, resistivity of ~1 ohm-m, and sonic velocities of ~270 μs/ft. Overlying oldest Upper Oligocene beds have lower GR of ~10 API, higher resistivity of ~20 ohm-m, and higher sonic velocities of ~200 μs/ft.

The Oligocene - Miocene (O-M) boundary (SB8) is a high-amplitude, sigmoidal, continuous trough that truncates reflectors below and is downlapped by reflectors above. The peak represents the strong impedance contrast of slower, less dense calcisiltic limestone above and the faster, higher density cherty, re-crystallized limestone below

(Woodside, 1980). Petrophysically, the underlying youngest Oligocene beds exhibit low GR of ~20 API, resistivity of ~4 ohm-m, and sonic velocities of ~210 µs/ft. This contrasts with the overlying oldest Miocene beds that have higher GR of ~55 API, lower resistivity of ~2 ohm-m, and slower sonic velocities of ~300 µs/ft. These contrasting petrophysical values allow for easy identification of the O-M boundary on well logs.

Sequence Boundary SB13 represents the Lower - Middle Miocene (LM-MM) boundary, and is the surface across which the transition from heterozoan carbonate ramp deposition to photozoan rimmed shelf deposition occurs (Rosleff-Soerensen et al., 2012). For mapping within the seismic dataset, we utilized the previously defined LM-MM boundary as inferred from GR correlations between offset wells and extrapolation from regional seismic lines by Woodside Energy (2007, 2008, 2009). The LM-MM boundary represents the top of the interval of interest for this study. Seismically, the LM-MM boundary is a medium to high-amplitude, sigmoidal, continuous peak that truncates underlying reflectors and is onlapped by overlying reflectors. In well logs, the underlying youngest Lower Miocene beds exhibit GR of ~20 API, resistivity of ~1 ohm-m, and sonic velocities of ~260 µs/ft. Overlying oldest Middle Miocene beds that have higher GR of ~30 API, higher resistivity of ~2 ohm-m, and equal sonic velocities of ~260 µs/ft.

II.5.3 Depositional Slope Angles and Slope Channels

The ramp margin, or shelf break, and toe of slope in the dataset were identified by a marked change in reflector dip angle (e.g. Wiseman and Ovey, 1953). Seismic

reflectors increase in dip angle from < 2º to > 6º from the shelf towards the basin for the ramp margin, and markedly decrease in dip angle from > 6º to < 3º from the slope towards the basin at the toe of slope (Fig. 9). Manual identification of shelf break and toe of slope, combined with vertical reflector offset along minor faults and areas of more gradual change in slope angle, introduced subjectivity and uncertainty in the position of the picked shelf break and the subsequent analysis of progradation and aggradation.

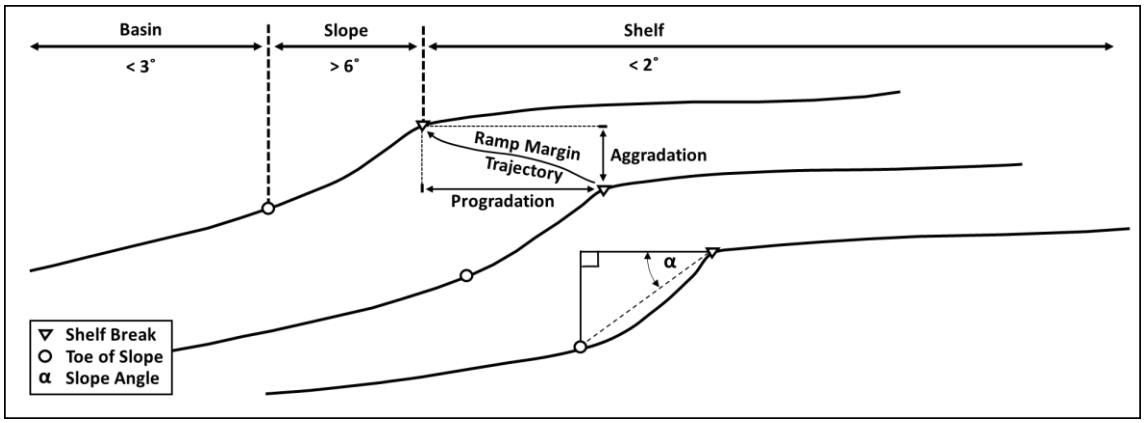

Figure 9: Schematic dip section of clinoforms and their geomorphic parameters for calculation of slope angles, progradation, and aggradation. In the dataset, reflectors on the shelf are usually inclined less than 2°. The marked increase in reflector dip from less than 2° landward to more than 6° along the slope marks the position of the shelf break or ramp margin. A transition of reflector dip from more than 6° along the slope to less than 3° in the basin marks the toe of slope. Slope angles were measured as the dip of a straight line from shelf break to toe of slope. The basinward shift of the ramp margin between two sequence boundaries quantifies progradation. The vertical difference in ramp margin position between two sequence boundaries quantifies aggradation.

We calculated slope angles as the inclination of a plane from the shelf break to the toe of slope (Fig. 9) and accounted for the effect of differential compaction by flattening the seismic volume at the top of the Miocene reefs that are overlain by hemipelagic sediments. The flattening decreased reflector dip angles by less than 1º. Moreover, we did not correct carbonate clinoform geometries for compaction, subsidence and isostasy. Although simple compaction can result in a decrease of slope angles, correcting for the complex interplay of rotation induced by differential loading, compaction, and thermal subsidence, tends to result in an overall increase in calculated clinoform slope angles (Steckler et al., 1993). Thus, calculated slope angles in this study represent minimum slope angles.

A shelf break is not apparent in seismic sequences SS1 and SS2; the dataset covers only their foreset and bottomset portions (Fig. 5). Hence, slope angles were calculated for only SS3–12 (Fig. 9). Slope angles for each individual sequence were calculated using 10 depth-converted, dip directional seismic profiles. The lateral range of slope angles for any given seismic sequence did not exceed 3°. Slope angle for each seismic sequence is reported as the arithmetic mean of slope angles for the ten dip-directional seismic profiles. Minimum and maximum slope angles for each seismic sequence are visualized as lower and upper error bars, respectively (Fig. 10).

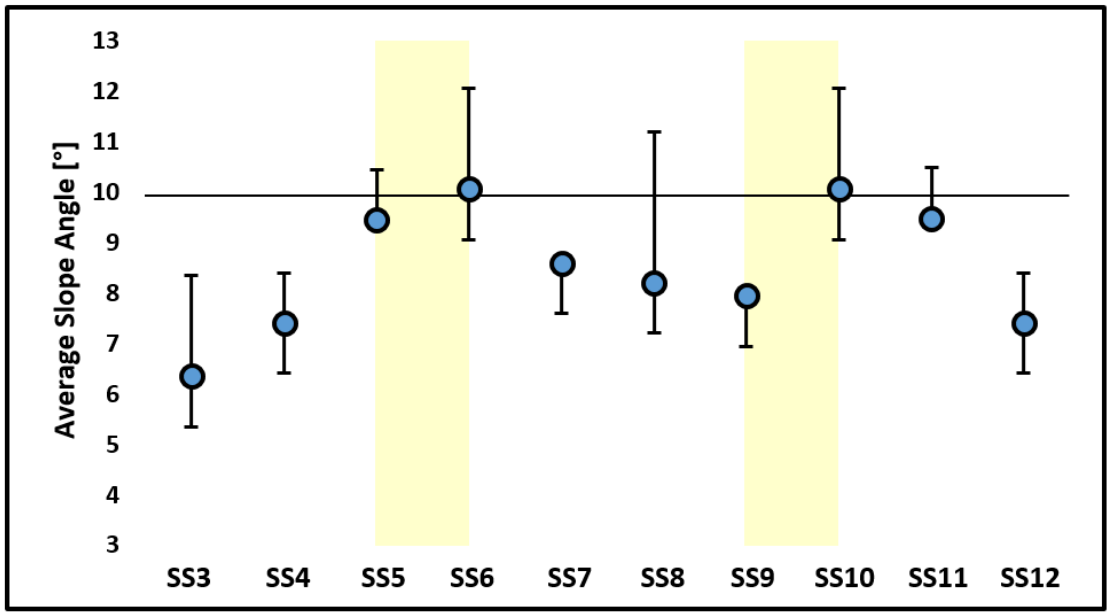

Figure 10: Average slope angles for seismic sequences SS3-12 measured on depth converted seismic as inclination from shelf edge to toe of slope. Error bars are the maximum and minimum slope angles along strike for each sequence, respectively. Minimum slope angles for seismic sequences 5 and 11 and maximum slope angles for seismic sequences 7 and 9 coincide with average values. Horizontal black line marks a critical slope angle of 10 degrees. Average slope angles in excess of 10 degrees occur between SS5&6 and SS9&10 (yellow boxes) and coincide with a re-organization in slope channel properties (Fig. 11).

The average slope angles for seismic sequences SS3 through SS12 range from a minimum of 6º in SS3 to a maximum of 10º in SS6 and SS10 (Fig. 10). Along the individual dip directional seismic profiles, the minimum slope angle is 5º (in DL5 of SS3), and the maximum slope angle is 12º (in DL1 of SS6 and in DL2 of SS10). Average slope angles initially increased from 6º in SS3 to 10º in SS6. Subsequently, average slope angles decreased from 9º in SS7 to 8º in SS9. A marked increase in

average slope angles to 10º in SS10 was followed by a decrease in average slope angles to 7º in SS12.

The slope channel properties were measured and/or calculated on a per seismic sequence basis and include: average number of channels, average channel depth, average channel width, and cumulative channel cross sectional area (CCCSA) (Fig. 11). We designed the CCCSA parameter of slope channels as a new measurement to quantify the capacity of basinward sediment transport through coeval slope channels during the time represented by one seismic sequence. CCCSA approximates the channel cross sectional area as a half ellipse:

Equation 1:

$$CCCSA = \frac{1}{4} * channel\ number * channel\ width * channel\ depth * \pi$$

The slope system evolved through three time intervals or phases that we defined by distinct changes in slope channel properties: Phase I) Middle – Upper Oligocene (SS3 – SS5); Phase II) Upper Oligocene – Lower Miocene (SS6 – SS9); and Phase III) Lower Miocene (SS10-SS12) (Fig. 11). The boundaries of these three phases correlate with peaks in slope angles during SS6 and SS10 (Fig. 10).

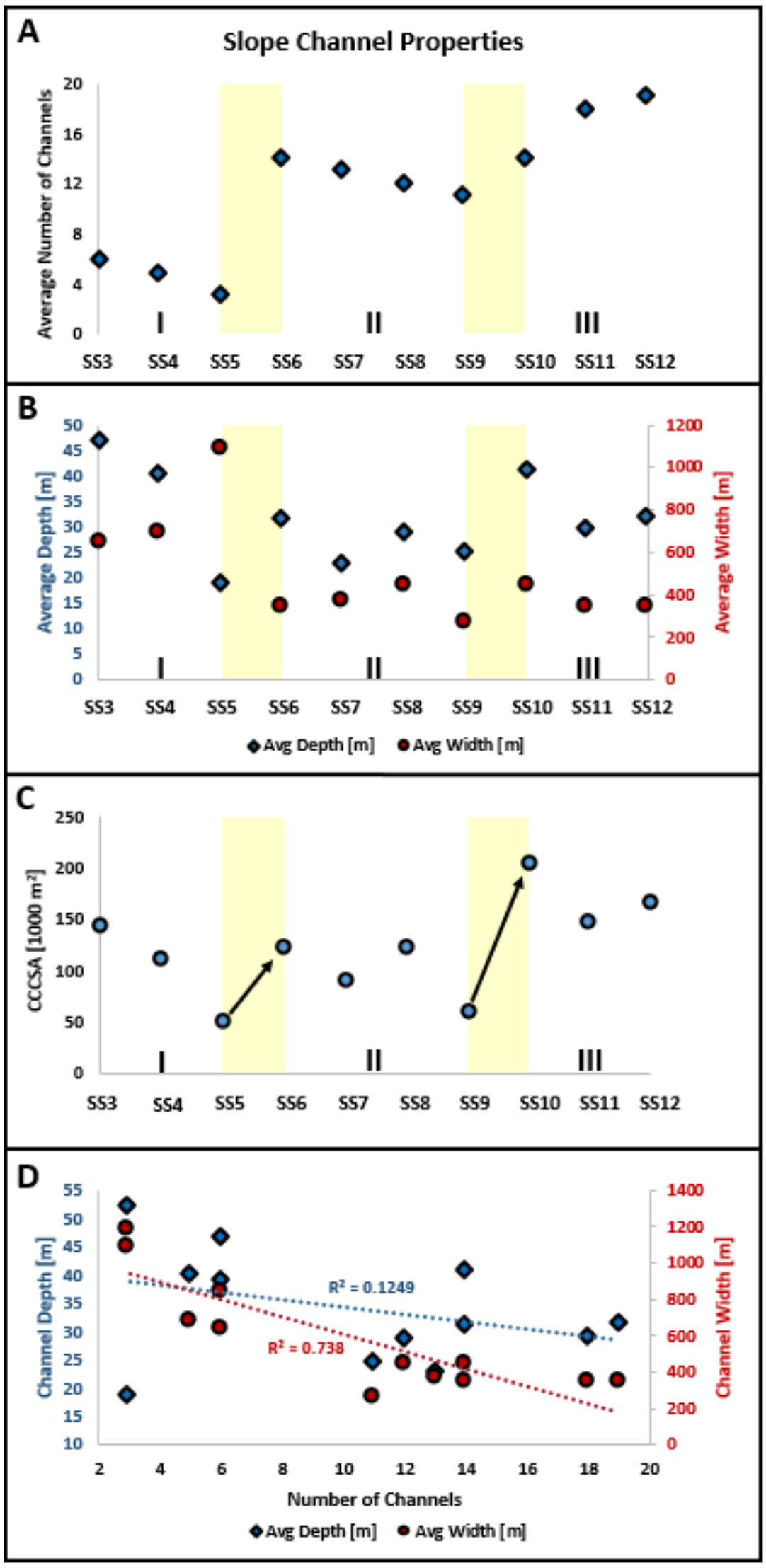

Figure 11: Compilation of channel properties for seismic sequences SS3-12. Yellow boxes mark the re-organization of the slope channel system between phases I, II, and III. Channel properties were identified from multiple strike directional seismic cross sections and 3D seismic surfaces. A – Average number of slope channels per seismic sequence. SS6 marks a distinct transition in channel properties to an overall increased number of slope channels. B – Average depth and width of slope channels per seismic sequence. SS6 marks a distinct drop in average channel width. C - Cumulative channel cross sectional area (CCCSA) per seismic sequence. CCCSA is a measure of the average available area of the channel system for basinward sediment transport. When CCCSA falls to about 50,000 m^2 and subsequently increased drastically (e.g. during SS5-SS6 and SS9-SS10; black arrows), the slope system established more channels in the subsequent seismic sequence. Therefore, we consider CCCSA a measure of slope system stability. D - Cross-plot of average channel width and depth against total number of channels. The falling trendline with an R^2 value of 0.74 indicates an inverse relationship between total number of channels and channel width. Channel depth correlates poorly with number of channels (R^2 = 0.12). Note the separation between the cluster of deep and wide channels (left half) vs shallower and narrower channels (right half).

During slope channel phase I, the average number of channels decreases from six in SS3 to three in SS5, with channel widths increasing from 650 m in SS3 to 1,100 m in SS5 and channel depths decreasing from 47 m in SS3 to 19 m in SS5, while CCCSA decreased from 144,000 m^2 in SS3 to 49,000 m^2 in SS5 (Fig. 11). Slope channel phase II is characterized by a distinct increase in number of slope channels per seismic sequence compared to phase one. Within phase II, the number of slope channels decreases from 14 in SS6 to 11 in SS9, but are more than double the average number of channels in phase one. Slope channel average widths in phase II distinctly decrease relative to those in phase I, and range from 275 m to 450 m (Fig. 11). Phase II slope channel average depths exhibit a slight decrease from 32 m in SS6 to 25 m in SS9, with a minimum average slope channel depth of 23 m in SS7. CCCSA decreases from 121,000 m^2 in SS6 to 59,000 m^2 in SS9. In slope channel phase III, the average number of slope channels increases from 14 in SS10 to 19 in SS12. Average channel widths decrease from about 450 m in SS10 to 350 m in both SS11 and SS12, while average channel depths similarly decrease from 41 m in SS10 to 30 m and 31 m in SS11 and SS12, respectively (Fig. 11). Lastly, the CCCSA values for seismic sequences of phase III are greater than those in phases I and II. However, as with the average slope channel widths and depths in phase III, the CCCSA decreases from 204,000 m^2 in SS10 and to 150,00 m^2 and 167,000 m^2 in SS11 and SS12, respectively.

In general, slope channel width inversely correlates with number of channels (Fig. 11d; $R^2 = 0.74$) and slope channel depth poorly correlates with number of slope channels (Fig. 11d; $R^2 = 0.12$) for any given seismic sequence. Slope channel width is an

order of magnitude higher than slope channel depths (Fig. 11b). Cumulative channel cross sectional area (CCCSA) is therefore more sensitive to changes in slope channel width than to changes in slope channel depth. The main control on CCCSA is the inverse relationship between channel width and number of channels.

It is important to note that there is a large increase in average number of channels and slope channel depth between SS5 and SS6 (3 vs. 14 channels; 19 m vs. 32 m channel depth), as well between SS9 and SS10 (11 vs. 14 channels; 25 m vs. 41 m channel depth). These significant changes mark the boundaries between slope channel phases I and II and phases II and III. The distinct increase in CCCSA between SS5 and SS6 (49,000 m^2 vs. 121,000 m^2), as well as between SS9 and SS10 (55,000 m^2 vs. 204,000 m^2) also marks the boundary between phases I, II, and III (Fig. 11).

II.5.4 Progradation and Aggradation

Aggradation and progradation are measured on profiles perpendicular to strike and calculated as the vertical and horizontal components, respectively, of the ramp margin trajectory between two seismic sequence boundaries (Fig. 9). We used ten dip-directional, depth-converted seismic profiles (dip lines: DL1 through DL10) with a spacing of 900 m to quantify along-strike variability of ramp margin trajectories in the system. We differentiate between progradation and aggradation across the entire *system* as a whole and along *individual dip lines*. Individual dip line progradation (IDP) and aggradation (IDA) capture lateral variability of ramp margin evolution on an intermediate scale of 100s m. System average progradation (SAP) and system average

aggradation (SAA) are derived parameters, calculated as arithmetic mean of IDP and IDA of the ten dip-directional seismic profiles. SAP and SAA capture the ramp margin evolution of the system through time as a whole on a larger scale of kilometers. Amplitude of IDP and IDA is a measure of the direction and intensity of ramp margin progradation, aggradation, retrogradation and degradation (down-stepping) along each of the ten dip-directional seismic profiles. We define lateral variability as along-strike differences in progradation and aggradation of the ramp margin trajectory. To parameterize lateral variability, we considered four derivative parameters: 1. IDA trajectory, 2. IDP trajectory, 3. Internal IDA amplitude variation, and 4. Internal IDP amplitude variation.

IDA and IDP trajectories describe whether or not the system, within a given seismic sequence, is uniformly prograding or aggrading relative to the previous seismic sequence. For example, if individual dip line aggradation (IDA) trajectories for all 10 seismic profiles of seismic sequence SS7 do not follow the same trend of aggradation or downstepping, then they are considered out of phase with each other. These are termed "non-uniform" IDA trajectories, and their occurrence means that the system aggrades along some dip lines, whereas it downsteps along other dip lines. The same applies to IDP trajectories. If IDP trajectories for all 10 dip profiles do not follow the same trend of progradation or retrogradation, they are considered out of phase and non-uniform, meaning that the system progrades along some dip lines, whereas it retrogrades along other dip lines.

Internal IDA and IDP amplitude variation quantify how strongly the system progrades, aggrades, retrogrades or degrades within a given seismic sequence:

Equation 2:

$$Internal\ IDA\ Amplitude\ Variation_{SSn} = Maximum\ IDA\ Amplitude_{SSn} - Minimum\ IDA\ Amplitude_{SSn}$$

Equation 3:

$$Internal\ IDP\ Amplitude\ Variation_{SSn} = Maximum\ IDP\ Amplitude_{SSn} - Minimum\ IDP\ Amplitude_{SSn}$$

$$where\ SS = Seismic\ Sequence, and\ n = 3 \rightarrow 12$$

When internal IDA and IDP amplitude variation are low, the system geometries evolve uniformly along strike. When internal IDA and IDP amplitude variation are high, the system experiences greater aggradation and/or progradation along some dip lines, and lesser aggradation and/or progradation along other dip lines. Lateral variability in the system, for any given seismic sequence, is low when IDA and IDP trajectories are uniform, and internal IDA and IDP amplitude variations are low. However, if IDA and IDP trajectories are out of phase and IDA and IDP amplitude variations are high for a given seismic sequence, then the lateral variability within that seismic sequence is deemed to be high.

The cumulative system average progradation (SAP) for the Oligocene - Lower Miocene interval is ~9 km during 20 million years, or about 450 m/Myr. SAP per

seismic sequence for the Oligocene - Lower Miocene strata (Fig. 12) ranges from a minimum of 199 m during SS11 to a maximum of 1,809 m during SS5. Individual dip line progradation (IDP) per seismic sequence varied from a minimum of -190 m (retrogradation in DL1 of SS11) to a maximum of 2,400 m (progradation in DL1 of SS5). Plotting IDA amplitude per seismic sequences (Fig. 12), individual dip line seismic profiles are in phase with the exception of SS5-6 and SS9-10. Internal IDA amplitude variation peaks between SS5-6, SS7-8, and SS9-10. IDP amplitude along the dip lines is out of phase during SS5-6, and SS7-10. Internal IDP amplitude variation peaks between SS5-6, SS7-8, and SS9-10 (Fig.12).

In general, progradation is an order of magnitude higher than aggradation in the studied succession and there is an inverse relationship between progradation and aggradation (Fig. 12e; $R^2 = 0.54$). When progradation rates are high, aggradation rates are low and vice versa. Cumulative system average aggradation (SAA) rate for the Oligocene - Lower Miocene interval amounts to ~320 m during 20 Million years or about 16 m/Myr. SAA per seismic sequence ranged from 74 m for SS6 and -12 m for SS5. Individual dip line aggradation (IDA) ranged from a minimum of -50 m (down-stepping in DL 1 of SS8) to a maximum of 100 m (in DL7 of SS6).

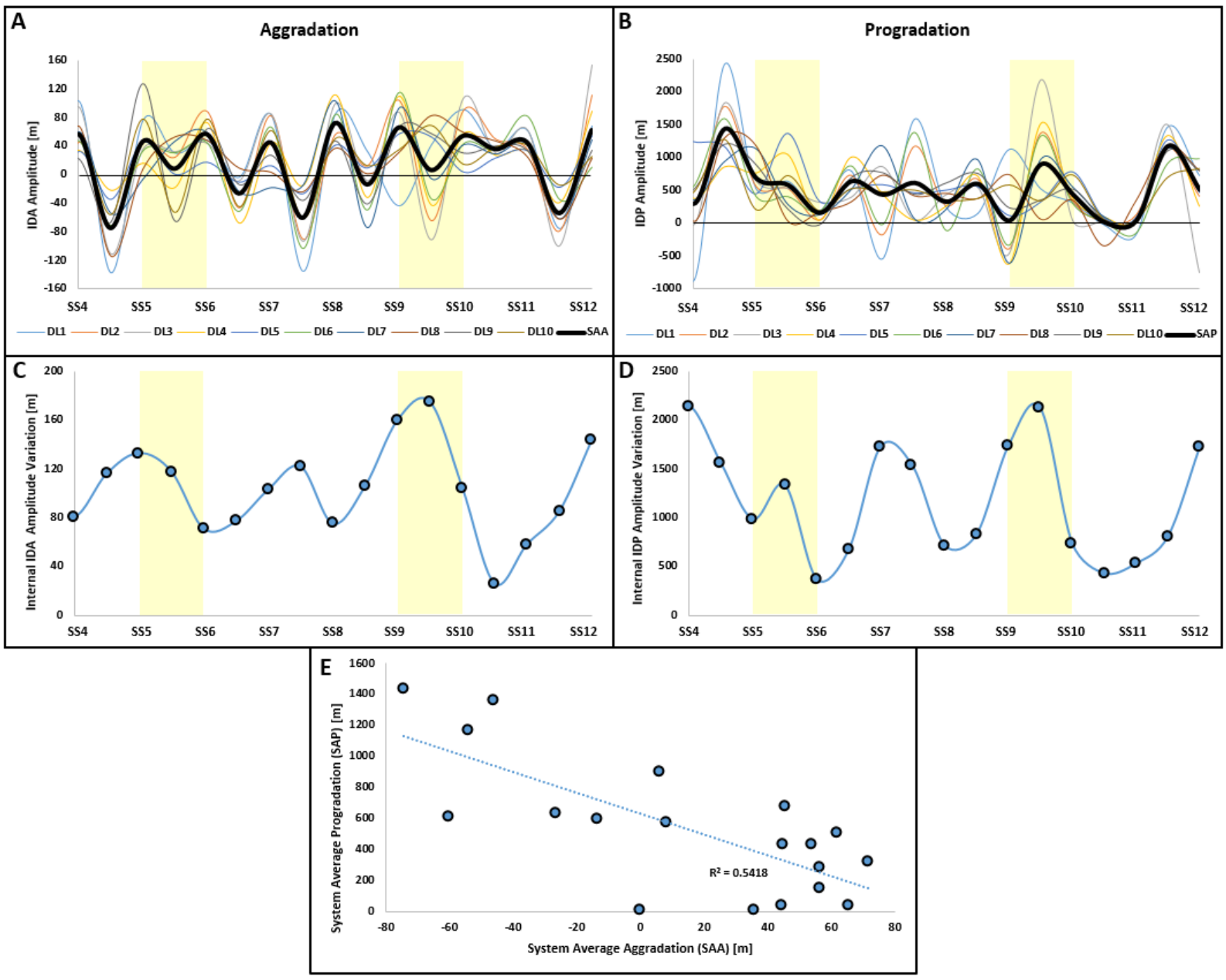

Figure 12: Progradation and aggradation behavior of the shelf edge during seismic sequences SS4-12 derived from depth converted seismic volume. A – Individual dip line aggradation (IDA) amplitude of vertical component of shelf edge trajectory for all ten dip lines DL1-10 (colored curves) and their system average aggradation (SAA; bold black curve). Values above 0 represent aggradation, values below 0 represent downstepping. B – Individual dip line progradation (IDP) amplitude of lateral component of shelf edge trajectory for all ten dip lines DL1-10 (colored curves) and their system average progradation (SAP; bold black curve). Values above 0 represent progradation, values below 0 represent retrogradation. C&D – internal IDA and IDP amplitude variation is a measure of how uniformly the shelf edge aggrades and progrades along strike. Note that the system experienced high lateral variability between SS5-6 and SS9-10, as denoted by coincident out of phase behavior of IDA and IDP amplitude and high internal IDA and IDP amplitude variation (yellow boxes). E - System average aggradation (SAA) plotted against system average progradation (SAP). The falling trendline with an R2 value of 0.54 indicates an inverse relationship between progradation and aggradation.

II.5.5. Seismically-Derived Subsidence Rates

The cumulative aggradation plot (Fig. 13) displays the cumulative aggradation of the ten individual dip lines DL1 through DL10 and SAA for seismic sequences SS4 through SS12. We used cumulative aggradation, in combination with relative sea level changes, as a proxy for subsidence, under the assumption that the carbonate system can fill accommodation faster than sea level can rise eustatically. This assumption is supported by previous work on cool-water carbonate-ramp growth potential, with calculated growth rates of 25 – 50 m/Myr or higher (e.g. James and Bone, 2010; Schlager, 2000). For our analyses, the allogenic input of siliciclastic material into the system is considered negligible. Accommodation is the space for potential sediment accumulation, and is a combination of subsidence, eustasy, sedimentation, and compaction (Jervey, 1988), and changes in accommodation are expressed as changes in relative sea level. Carbonate systems react to accommodation increase by aggradational growth (Sarg, 1988). If an accommodation increase is related to subsidence increase, and the carbonate system fills that new accommodation via aggradation, then the cumulative aggradation height can be used as a proxy for the amount of subsidence (Kendall and Schlager, 1981). In this study, we relate deviations from a constant slope in the cumulative aggradation plot to changes in subsidence. These deviations are not ascribed to changes in climate-driven eustasy, since eustasy during the Upper Oligocene through Lower Miocene averages 100 m +/- 50 m above present sea level, with no drastic long-term increase or decrease over more than 3 Myr (Haq et al., 1987; Miller et al., 2005).

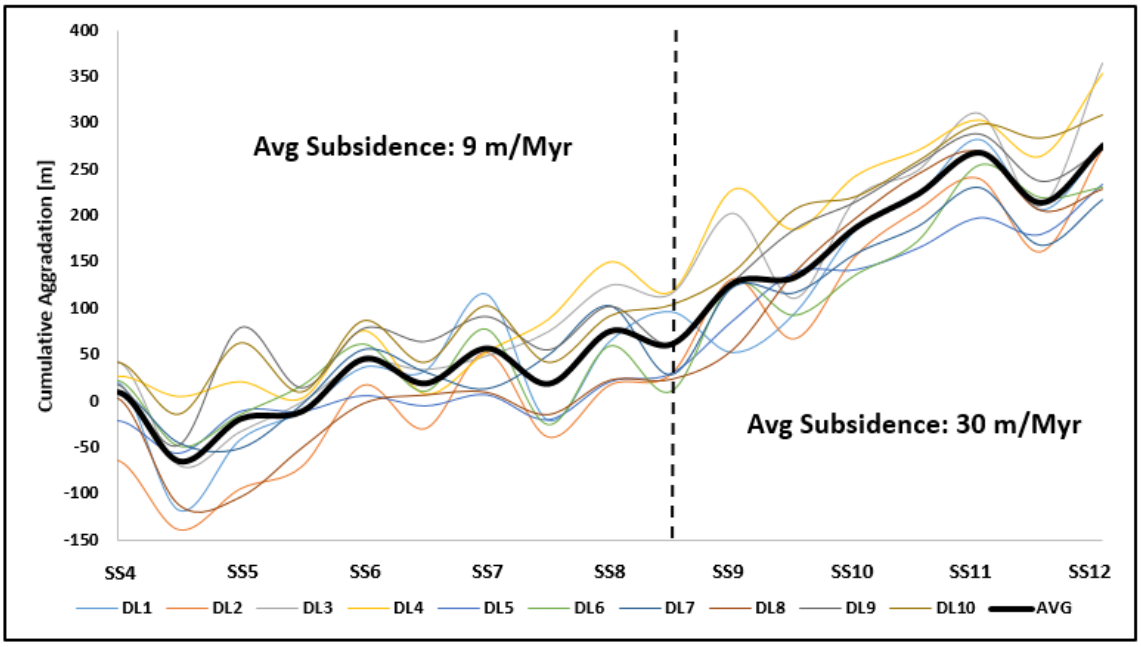

Figure 13: Cumulative aggradation for seismic sequences SS4-12 along dip lines DL1-10 from vertical component of shelf edge trajectory as proxy for basement subsidence. DL 1-10 = values for dip directional cross sections; AVG = average of all ten dip directional cross sections. Vertical black line marks the transition from time period 1 with lower cumulative aggradation of 19 m/Myr during SS2-8 to time period 2 with increased cumulative aggradation of 30 m/Myr during SS8-12. This corresponds to the transition from Early Tertiary thermal subsidence to Late Tertiary foreland loading (Fig. 17).

Based on the cumulative aggradation rates, age constraints and estimated absolute ages for the seismic sequences, we calculated subsidence rates for the system during the Upper Oligocene through Lower Miocene. In the cumulative aggradation plot (Fig. 13), a transition in derived subsidence occurs after seismic sequence SS8. During SS4 through SS8, cumulative aggradation is 64 m over 7.3 Myr, resulting in an average subsidence rate of ~9 m/Myr. During SS9 through SS12, cumulative aggradation is 212 m over 7.1 Myr, resulting in an average subsidence rate of ~30 m/Myr.

II.5.6. Seismically-Derived Relative Sea Level

The shelf edge trajectory of a sedimentary system describes the vertical and lateral migration of the shelf edge through time, and can be used as proxy of relative sea level (Helland-Hansen and Hampson, 2009; Henriksen et al., 2009; Johannessen and Steel, 2005; Mellere et al., 2002; Steel and Olsen, 2002). For this study, we translated changes in the vertical component of the distally-steepened ramp margin trajectory in the Oligocene-Lower Miocene section (SS3-12; Figs. 5 and 9) into changes in relative sea level under simplified boundary conditions. These boundary conditions are: 1) Clinoform shelf breaks develop at a constant depth below sea level, and thus, are indicative of changes in relative sea level when compared to overlying or underlying seismic sequences and their corresponding clinoform shelf breaks; 2) Carbonate sediment production rates were constant and allogenic siliciclastic influx was negligible across the shelf during the Upper Oligocene through Lower Miocene; 3) Changes in aggradation and progradation through time are caused by the response of the carbonate factory growth to accommodation (as described above); and 4) Non-deposition/erosion account for lost time but are not represented in the seismic. In order to compensate for basement subsidence in the calculation of the seismically-derived relative sea level curve, we subtracted subsidence rates for the Browse Basin of 10 m/Myr for the Oligocene and 25 m/Myr for the Miocene (Kennard et al., 2003) from the aggradational component of the ramp margin trajectory. For example, the average ramp margin position of SS5 was 74 m below the average ramp margin position of SS6. Accounting

for Oligocene subsidence with 10 m/Myr during the 1.8 Myr between SS5 and SS6, we infer a seismically derived relative sea rise of 56 m between SS5 and SS6 (Fig. 14).

Ten relative sea level curves were derived from the ten dip-directional seismic profiles DL1 to DL10 (Fig. 14). A new, local Upper Oligocene and Lower Miocene relative sea level curve for the study area was derived by averaging the ten dip-directional seismic profile-derived relative sea level curves (Fig. 14). For the study, this new curve is termed “System Average Relative Sea Level Curve”. The System Average Relative Sea Level Curve ranges from a minimum of –84 m between seismic sequence SS4 through SS5 to a maximum of 72 m in SS11. A marked increase in relative sea level occurred during SS5 through SS6 with relative sea level increase by 91 m, and from SS 9 through SS11 relative sea level increased by 115 m, whereas relative sea level fell by 20 m during SS6-9. Note that relative sea level along the dip profiles can vary significantly. For example, relative sea level during SS9 can vary laterally from a maximum of ~100 m for dip line DL4 (yellow curve) to a minimum of ~-75 m for adjacent DL5 (blue curve).

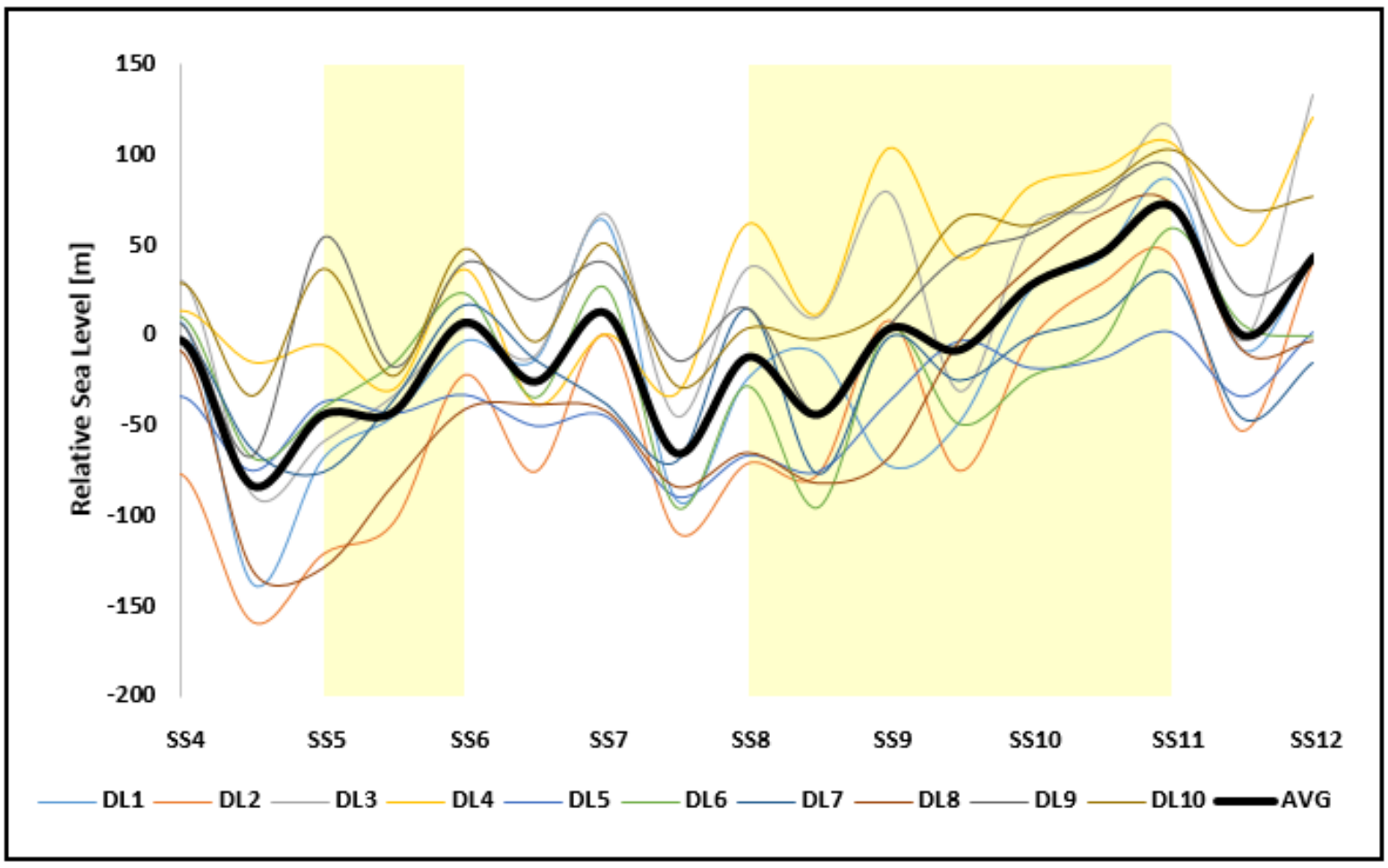

Figure 14: Seismically-derived relative sea level curve for seismic sequences SS4 through SS12. The seismically-derived sea level curve is derived from the aggradational component of the ramp margin trajectory (Fig. 12) under consideration of basement subsidence for the Oligocene and Lower Miocene (Fig. 2). Phases of sea level rise during SS5 through SS6 and SS8 through SS11 are highlighted by the yellow boxes.

II.5.7. Depositional Geometries

The prograding carbonate clinoforms of the Upper Oligocene through Lower Miocene are identified as large-scale sigmoidal reflectors between 1,700 – 3,200 m depth (Fig. 5). Vertical thickness of a typical clinoform, from topset to bottomset for the sigmoidal reflectors, is on the order of 500 m in our depth-converted volume. The average lateral extent from shelf break to toe of slope of a typical clinoform is 6 km, and average slope angle is 8º. No carbonate boundstone rim or barrier was identified in the ten individual dip-directional seismic profiles (DL1 to DL10) at the shelf break positions for any of the 12 seismic sequences or boundaries (Fig. 5). We calculated isopach maps for each of the 12 seismic sequences to identify main depocenters with thick sediment deposition, and slope bypass channels with thin sediment deposition (Fig. 15). Furthermore, we created a thickness profile for SS3-SS12 from DL5 to visualize the thickness distribution from shelf to basin within the seismic sequences (Fig. 16).

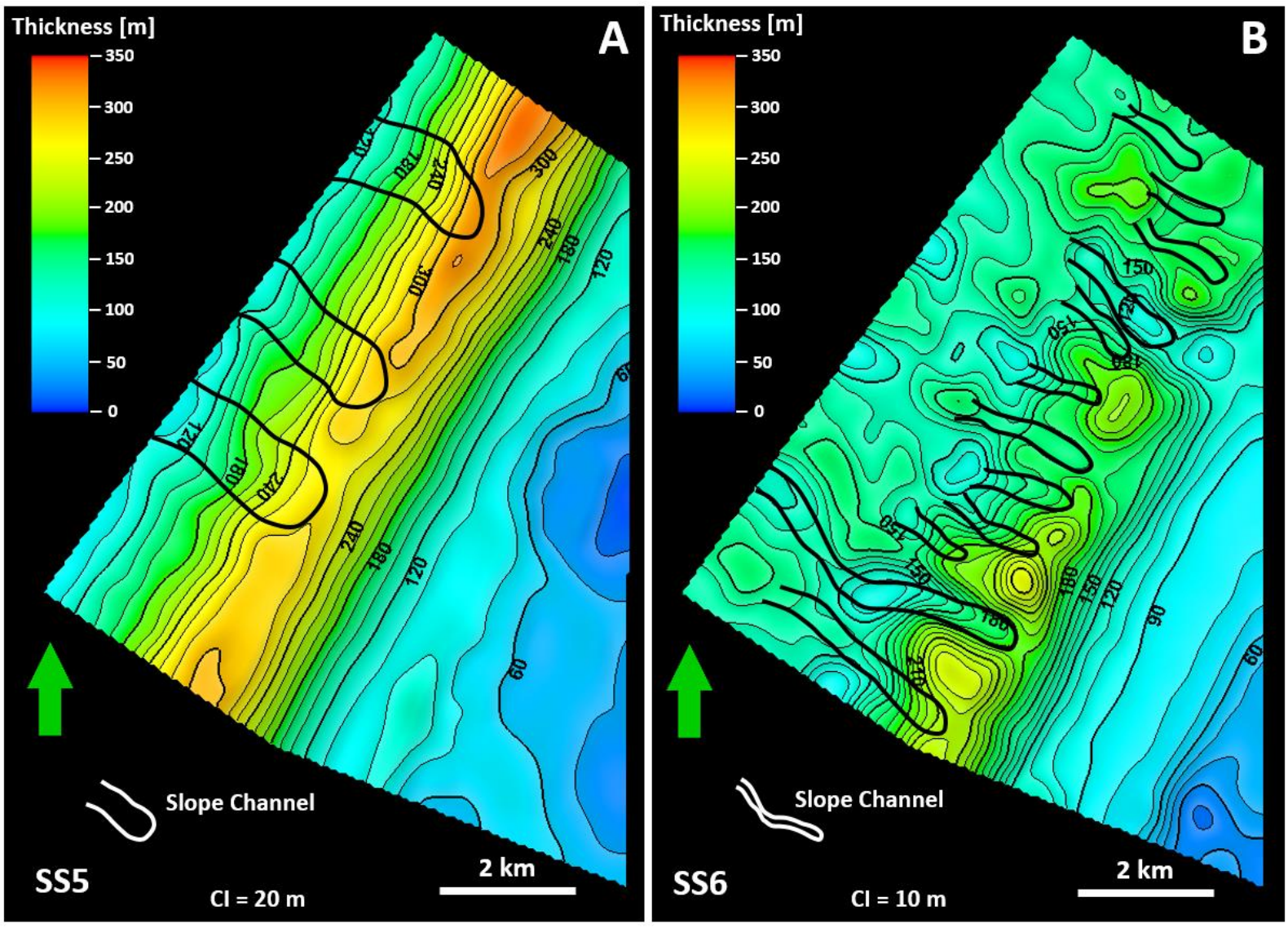

Figure 15: Isopach maps for seismic sequences SS5 and SS6. Low slope angles during SS5 coincide with thick, more laterally continuous slope deposits. Subsequent steepening of slope angles beyond 9° during SS6 (Fig. 10) initiates slope channel incision. Slope channel incision during SS6 partitioned the line source and decreased the amount of sediment deposited along the slope due to erosion and basinward sediment transport.

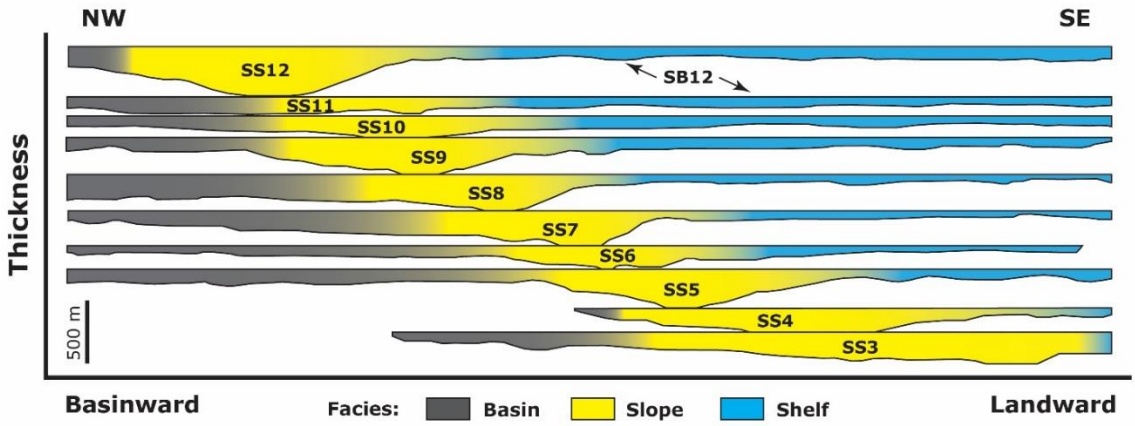

Figure 16: Thickness profile, not a Wheeler diagram, of seismic sequences SS3-12, illustrating sediment thickness variability for each sequence from the shelf into the basin. Profile is derived from reflector geometries in dip sectional profile DL5 (Fig. 5). Note that the lower boundary of the overlying sequence is the same as the upper boundary of the underlying sequence, e.g. base of SS12 = SB12 = top of SS11. Shelfal deposits are relatively thin compared to deposits along the slope and the basin. The northwest shift of facies in the seismic sequences indicates the progradation of the carbonate ramp through time.

The thickest sediment volumes that are represented by numerous reflectors are preserved along the slope (Figs. 5 and 16). Contrastingly, the number of reflectors decreases by lapout shelfward and basinward, and fewer reflectors represent thinner sediment accumulations. Generally, shelf deposits within the seismic sequences are relatively thin (~50 m) compared to slope deposits (~150-350 m) and basinal deposits (~50-150 m) (Figs. 15 and 16). Maximum isopach thicknesses for seismic sequences SS1 to SS12 ranges from 160 m (in SS11) to 450 m (in SS12). The depocenters of SS3 to SS12 are oriented parallel to the ramp margin, which for each of these seismic sequences, strikes southwest-northeast. Basinal sediment lobes are relatively symmetrical and elongated perpendicular to the ramp margin. SS5 and SS9 have thick

(up to 350 m), laterally continuous slope deposits. However, SS6 ,SS10 , and SS11 have relatively thin (~150-250 m) and laterally discontinuous slope deposits. Coincident with slope angles greater than 9°, SS6, SS10, and SS11 are also relatively thin across the entire shelf to basin profile.

II.6. Discussion

II.6.1. Ramp Geometry Evolution

The Oligocene through Lower Miocene carbonate system of the Browse Basin is a distally-steepened heterozoan carbonate ramp with steep slopes and slope channels that display a distinctly different morphology from that of the underlying Paleocene and overlying Middle and Late Miocene deposits. The underlying Paleocene and older fluvial-deltaic clastic deposits display a rugose, low-angle (<1º) ramp seismic geomorphology (Fig. 5). By Late Oligocene, the depositional profile had changed into a distally-steepened (6-9º) carbonate ramp with three to six slope channels of ~500 – 1,100 m width. During the Latest Oligocene through Early Miocene, the depositional profile remained a distally-steepened (7-10º) ramp, but slope channels markedly increased in abundance to 11-19 and decreased in width to ~350 m (Fig. 11). Based on seismic geomorphology, no carbonate boundstone barrier or rim could be identified that would have formed during the carbonate ramp phase of the system (Figs. 5 and 8). During Middle and Late Miocene, the carbonate system prograded and aggraded basinward towards the northwest and evolved into a carbonate rimmed-shelf with seismically-identifiable geomorphic boundstone barriers (Fig. 5).

Within the context of a carbonate ramp, the outer ramp environment lacks a pronounced slope break, and submarine gravity-driven mass wasting deposits are assumed to be absent (Ahr, 2011). However, distally-steepened ramps exhibit easily recognizable and seismically-definable breaks-in-slope that define a "ramp-margin". Typically, well defined depositional clinoforms form at these distally-steepened ramp-margins. When such clinoforms exceed 100 m in height, they are deemed to be "continental-scale" clinoforms (Helland-Hansen and Hampson, 2009). Due to the ~500 m vertical height of the Browse Basin Oligo-Miocene clinoforms of this study, they are classified as continental scale clinoforms (i.e., Helland-Hansen and Hampson, 2009). Furthermore, fine-grained foramol carbonate ramp systems, such as the study system, tend to build distally steepened ramps (Kenter, 1990; Pomar, 2001). The Oligocene to Lower Miocene carbonate system in the Browse Basin clearly exceeds the usual 1º ramp inclination, and there is no seismically-identifiable geomorphic barrier or reef complex. Lastly, we identified a clear change in seismic reflector geometry at the ramp-margin. Shelfward sub-horizontal, parallel reflectors transition into basinward dipping and sigmoidal channelized slope reflectors, back to basinal sub-horizontal rugose reflectors. This distinct change in reflector geometries demonstrates that the depositional profile for the Browse Basin Late Oligocene to Early Miocene carbonate system is a distally-steepened ramp. The fact that most of the sediment volume in the clinoforms is preserved along the slope indicates that this Late Oligocene to Early Miocene margin in the Browse Basin, was not a bypass margin (e.g., Read, 1985) where all sediment

bypassed the slope through slope channels and canyons from the shelf, where it was produced, and into the basin where it was deposited.

Previous research regarding the effect of ocean currents on the evolution of Neogene carbonates of the Maldives and Holocene carbonates of the Great Bahama Bank reveals that ocean currents can significantly influence the geometry of carbonate deposits by causing asymmetrical drift deposits, sediment wedges or sediment waves (Betzler et al., 2013; Betzler et al., 2014), thus causing lateral variability in depositional geometries. The Leeuwin Current is a moderately strong ocean current that was established by Early Oligocene time (Wyrwoll et al., 2009), and today, transports warm, low salinity, tropical water from Indonesia southward along the northwestern and western margin of Australia (Cresswell, 1991).

Lateral variability in the ramp margin trajectory along the ten individual dip-directional seismic profiles indicates that the carbonate depositional system does not uniformly record progradation and aggradation over time. However, in seismic horizon slices and strike directional seismic profiles, we did not identify asymmetrical drift deposits, sediment wedges or sediment waves. Slope channel geometries are of low sinuosity and basinal sediment lobes are not asymmetrically redirected in a preferred orientation.

While the Leeuwin Current was established during the time of Late Oligocene to Early Miocene deposition in the Browse Basin carbonate ramp system (Wyrwoll et al., 2009), we did not interpret any depositional products resultant of Leeuwin geostrophic current. We suggest that lateral variability in the ramp margin trajectory parameters for

SS1 to SS12 and the stratigraphic architecture were neither caused by nor significantly affected by lateral geometric modifications to depositional bodies by geostrophic currents.

II.6.2. Seismically Derived Parameters

II.6.2.1. Subsidence

Kennard et al. (2003) identified two distinct phases of tectonic subsidence for the Browse Basin from Cretaceous through Recent times. The first phase ranged from 141 Ma (Early Cretaceous, Berriasian) to 28 Ma (Early Oligocene), and is characterized by progressively slower subsidence of ~10 m/Myr due to thermal cooling of the Browse Basin after Late Jurassic volcanism and seafloor spreading in the adjacent Argo Abyssal Plain. The second phase ranged from 28 Ma (Middle Oligocene) to 0 Ma (Present), and is characterized by accelerated subsidence of ~25 m/Myr that is associated with foreland loading due to collision of the Australian plate with the Banda Arc (Baillie et al., 1994; Kennard et al., 2003). Subsidence rates for the Browse Basin tectonic phases were modeled from multiple pseudo-wells, which demonstrated that the first subsidence phase of relative tectonic quiescence allowed the basin to be effectively decoupled from older fault systems (Kennard et al., 2003).

Our seismically-derived subsidence rates for seismic sequences SS3 through SS12 of ~9-30 m/Myr (Fig. 13) are in general agreement with the modeled tectonic subsidence rates by Kennard et al. (2003). While previous work by Kennard et al. (2003) calculated this shift from lower tectonic subsidence to higher tectonic subsidence to start

at the Early – Late Oligocene boundary (28 Ma), the subsidence curve from our study has a marked change in derived tectonic subsidence starting somewhat later in SS8 (Lower Miocene, ~23 Ma). This delay in signal could be attributed to the relative inboard/outboard position of our study area to the pseudo-well locations that Kennard et al. (2003) used for their subsidence model.

The reasonable match between our seismically derived Browse Basin subsidence rates and subsidence rates modeled by Kennard et al. (2003) indicates that 1) The signal of subsidence is preserved in the dataset; and 2) Our application of trajectory analysis and cumulative aggradation analysis was a suitable way to reconstruct subsidence information from seismic data.

II.6.2.2. Relative Sea Level

We relate the observed inverse relationship between aggradation and progradation in SS1 through SS12 (Figure 12e) of $R^2 = 0.54$ to relative sea level changes. At constant subsidence and sediment production rate, a rise of relative sea level creates accommodation, resulting in increased aggradational carbonate system growth, whereas a decrease in accommodation results in increased progradation of the system (Sarg, 1988; Schlager, 2000; Van Wagoner, 1988). During phases of high relative sea level, most sediment is used for the vertical growth of the system, as is visible in the high cumulative aggradation parameter values. During phases of low sea level, accommodation is limited, and excess sediment that cannot aggrade is transported basinward and contributes to system progradation.

Browse Basin regional (Woodside Energy, 2007) and global (Haq et al., 1987) sea level curves were compared to the seismically-derived System Average Relative Sea Level Curve (Fig. 17) in order to see how well the paleo sea level signal is preserved in the data. The comparison between the seismically-derived System Average Relative Sea Level Curve and the reference curves is considered a good match when both curves are synchronized in phase and have equal amplitude. We used maximum and minimum values from the ten individual dip-directional seismic profile-derived relative sea level curves to create an uncertainty envelope around the System Average Relative Sea Level Curve to visually account for lateral variability.

Plotting the seismically-derived relative sea level curve against the regional reference curve of Woodside Energy (2007) yields a correlation coefficient of 0.81 (Fig. 17) and provides three key insights: 1) The resolution of the seismically-derived sea level curve is slightly coarser and does not capture the higher frequency signals of the Woodside reference curve. This is because we based the seismically-derived sea level curve on 19 data points of the average ramp margin position during SS4-12, which corresponds to one data point every 0.9 Myr and 0.7 Myr for the Oligocene and Lower Miocene, respectively. A higher sampling rate of the ramp margin position could resolve higher frequency signals in the seismically-derived sea level curve and converge to a similar frequency content as the reference curve.

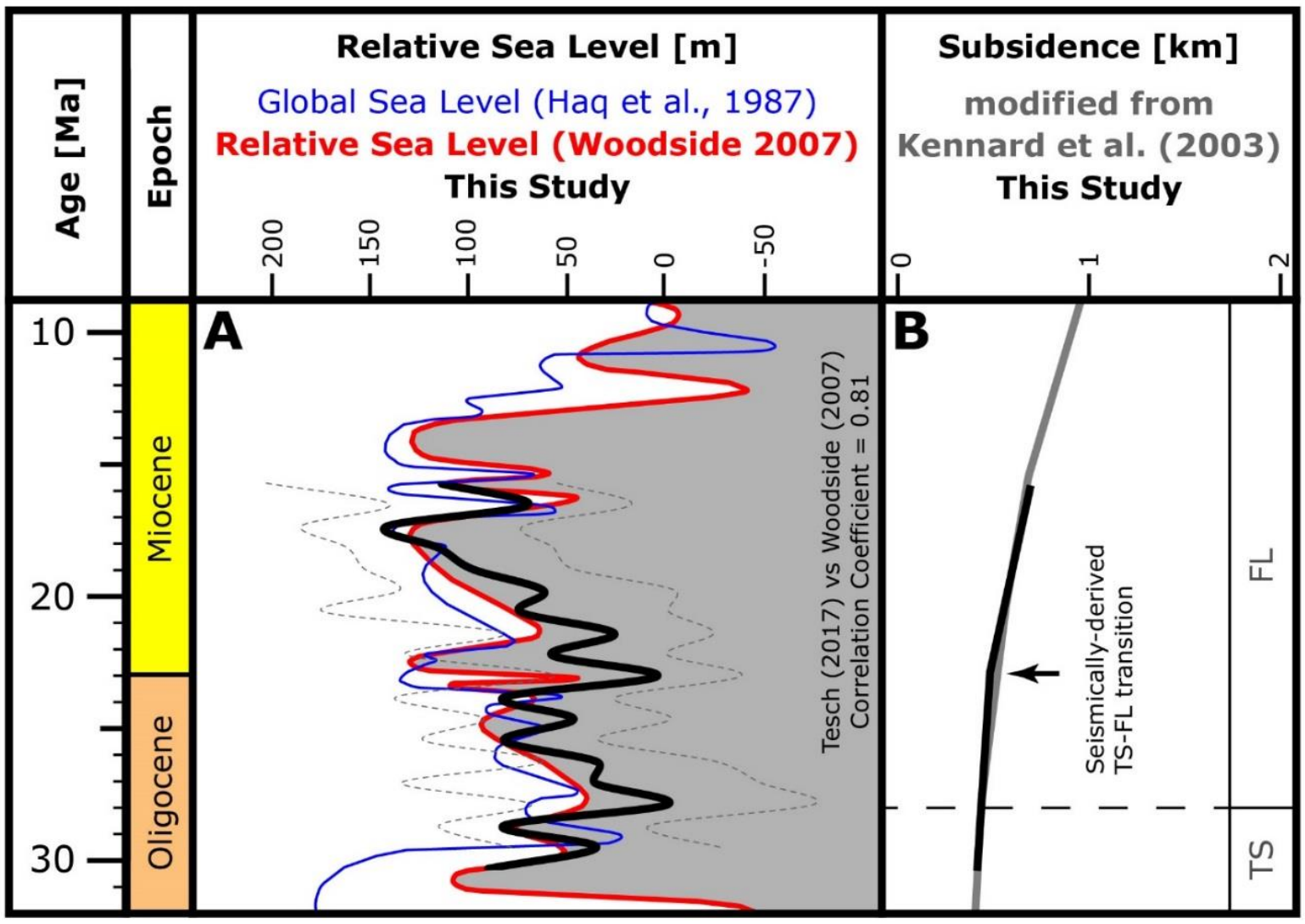

Figure 17: Composite results of seismically derived sea level and subsidence signals compared to reference data from the literature for the Upper Oligocene through Lower Miocene. A – seismically derived sea level curve in black with stippled gray uncertainty envelope (this study), regional reference curve in red (Woodside Energy, 2007) and eustatic sea level curve in blue (Haq et al., 1987). The correlation coefficient between our seismically-derived relative sea level curve and the regional reference curve is 0.81. The seismically derived sea level curve has a lower frequency and amplitude than the reference curves but captures the major sea level rise and fall trends of the regional reference curve. Uncertainty envelope is derived from strike directional variability of the seismically derived sea level curve. B – Browse Basin subsidence with 28 Ma marking the transition from Early Tertiary thermal subsidence to Late Tertiary foreland loading, modified from Kennard et al. (2003). Grey curve = basement subsidence after Kennard et al. (2003); black curve = inferred basement subsidence from cumulative aggradation (this study). TS = thermal subsidence, FL = foreland loading. Good match between inferred subsidence from seismic and the reference curve indicates a good preservation of the subsidence signal in the data and a strong impact of the basement subsidence signal on the system geometries.

2) The amplitude of our seismically-derived sea level curve is lower (~35 m) than the amplitude of the reference curve (~50 m) in the Oligocene through Lower Miocene interval. The muted amplitude signal of the seismically-derived sea level curve can be explained by averaging the ten relative sea level curves from dip-directional seismic profiles DL1-DL10 into a System Average Relative Sea Level Curve (Fig. 14). Averaging the values results in a smoothing of the extreme ups and downs in the identified ramp margin positions. 3) The seismically derived sea level curve captures each up and down trend of the reference curve throughout the Oligocene and Lower Miocene interval. The correlation coefficient of 0.81 between our seismically derived relative sea level curve and reference data from Woodside Energy (2007) indicates that the signal of relative sea level is preserved in the dataset.

II.6.3. External Controls and Internal Response

II.6.3.1 Slope Angles and Slope Channels

With few exceptions, slope channels do not commonly develop in carbonate ramp systems due to their low angle depositional profiles (Gómez-Pérez et al., 1998; Rankey, 2003). However, in the Browse Basin dataset, slope channels are prominent features throughout the depositional history of the Late Oligocene to Early Miocene distally-steepened ramp (cf. Figs. 8 and 11). The steep slope angles (5-12º) of the Browse Basin ramp favorably compare to an Upper Miocene, distally steepened ramp in Menorca, with ramp slope angles up to 20º (Pomar et al., 2002). The distally steepened Menorca ramp contains large-scale troughs trending basinward within the slope. These

troughs have widths of up to 1 km and thicknesses of up to 60 m, making them comparable in size to the slope channels identified in seismic sequences SS3 to SS5 of the Browse Basin Oligo-Lower Miocene distally-steepened ramp.

We suggest that lateral variability of the ramp margin in the system was determined by the erosional process of slope channel incision, which, in turn, was controlled by relative sea level changes. The relative sea level rise during seismic sequences SS5 through SS6 and during SS8 through SS11 increased accommodation, resulting in increased vertical growth and decreased progradation of the ramp margin during these times. This caused a steepening of slope angles to a maximum of 10° during SS6 and SS10 (Fig. 10). Coincident with average slope angles in excess of 9°, the slope system re-organized and transitioned from phase I-II between SS5-SS6 and from phase II-III between SS9-SS10 (Fig. 11). Moreover, lateral variability of the ramp margin trajectory was high during transitions between phases I, II, and II, as indicated by simultaneous out of phase behavior of IDA and IDP amplitude and high internal IDA and IDP amplitude variation (Fig. 12).

New slope channel incision during a re-organization of the slope system creates lateral ramp margin variability by affecting individual dip line aggradation (IDA) and individual dip line progradation (IDP) amplitude, as well as internal IDA and IDP amplitude variability. Channel incision causes a localized decrease in progradation and aggradation of the ramp margin, relative to areas that prograde and aggrade without geometrical modification of the ramp margin from slope channel incision. The localized geometrical modification of the ramp margin increases internal IDA and IDP amplitude

variability and creates a non-uniform IDA and IDP amplitude response. Thus, lateral variability of the ramp margin is high. Once the slope system re-organized, the newly established channel pathways caused subsequent slope channels to be stacked on older channels. This stable position of channel pathways along the slope resulted in decreased geometrical modification of the ramp margin and thus low lateral variability. Furthermore, we attribute the transition from thick and laterally continuous slope deposits in SS5 and SS9 to relatively thin and laterally discontinuous slope deposits in SS6 and SS10, respectively, to slope channel incision into the shelf at slope angles greater than 9°. Slope channel incision partitioned the line source and decreased the amount of sediment deposited along the slope due to erosion and sediment bypass into the basin.

Maximum average slope angles of 10° in this study conform with maximum slope angles in the Oligocene through Lower Miocene carbonate ramp of the Carnarvon Basin (~500 km southwest of the Browse Basin) range from 5-15° (Cathro et al., 2003). Generally, fine-grained foramol carbonate systems form distally-steepened ramps with slope angles of ~10-15° (Kenter, 1990; Pomar, 2001; Read, 1985). Once the carbonate system approaches the angle of repose, the slope system becomes unstable, initiating mass flow (Kenter, 1990; Lee et al., 2007), and thus increased basinward sediment flux along the slope. We argue that CCCSA captures the re-organization of the slope system in response to increased basinward sediment flux along the slope in excess of the angle of repose.

We consider the CCCSA parameter to be an indicator of slope system stability, similar to the fluvial avulsion threshold parameter in fluvial systems (Slingerland and Smith, 2004). When the fluvial avulsion threshold is reached, a fluvial system reaches a disequilibrium state at low slope angles. Equilibrium is re-established by a shift of the old fluvial pathway from the avulsion node into a new pathway on the floodplain. CCCSA is an expression of the equilibrium between basinward sediment flux and available flux capacity of the channel system. The slope system can be stable at low CCCSA values if the basinward sediment flux is low. A subsequent increase in sediment flux will de-stabilize the slope system. At this disequilibrium state, the slope system re-organizes to increase CCCSA through the incision of more slope channels to reach a new equilibrium state. The slope system will be in equilibrium during increased basinward sediment flux if CCCSA is sufficiently high to accommodate the high flux.

The amalgamation of slope channels decreased the total number of slope channels during SS3 through SS5 from 6 to 3, and during SS7 through SS9 from 14 to 11 (Fig. 11a). This channel amalgamation decreased the CCCSA through a decrease in channel number and channel depth (Fig. 11b, c). Amalgamation also changed the slope morphology from more localized, abundant and narrow pathways to fewer channels that are shallower and wider. Basinward sediment flux during SS3 through SS5 and SS7 through SS9 was relatively low due to vertical growth of the ramp, and was sufficiently accommodated by the low CCCSA. Once aggradational growth of the system raised average slope angles beyond 9° during SS6 and SS10 (Fig. 10), the angle of repose was reached, causing mass flow with increased basinward sediment flux bypassing the slope.

At this point, however, CCCSA was insufficient to accommodate the increased basinward sediment flux. The slope system reacted to this disequilibrium between increased sediment flux and low CCCSA by creating more slope channels and thus increasing CCCSA to accommodate for the increased sediment flux. In both instances, CCCSA is very low at 50,000 m^2 for SS5 and 55,000 m^2 for SS9, and subsequently increases to 120,000 m^2 in SS6 and to 200,000 m^2 in SS10 (Fig. 11). An abrupt increase in CCCSA is therefore indicative of an unstable slope channel system that undergoes re-organization.

CCCSA analysis highlights phases of major re-organization of the Browse Basin slope system, which are ultimately caused by sea level variations and characterized by a drastic change in the number, width and/or depth of slope channels. This technique can be easily applied in other channelized carbonate slope systems throughout geological time to identify stages of autogenic re-organization. Further research is required to test if CCCSA analysis can highlight significant changes in the signal of allogenic controls in other carbonate ramp and rimmed shelf systems.

II.6.3.2. Ramp Morphology

For the Browse Basin Late Oligocene to Early Miocene carbonate system, large-scale antecedent topography of the distally-steepened ramp profile was determined by regional Australian North West Shelf Mesozoic and Tertiary tectonic events, and the consequences of these events defined the location and SW to NE strike of the ramp margin. We attribute subsequent basinward (northwest) progradation of the carbonate

system, and the development of slope channels parallel to dip, to the large-scale basin geometry. An example of intermediate-scale basin geometry is the antecedent depositional profile of the Paleocene and older fluvial-deltaic strata that exhibit seismic reflector dips from 0º to 3º, with an average of 2º. Regardless of the antecedent topography, reflector inclinations of the overlying distally-steepened carbonate ramp consistently range from 5º to 12º for the slope, and less than 2º along the shelf. While Gischler and Lomando (2000) argued that localized antecedent topography can be as important in shaping younger, overlying system architecture as relative sea level changes, we did not interpret any barrier island, lagoon or other intermediate-scale Paleocene topographic features that were inherited by the overlying Late Oligocene to Early Miocene strata in the study area.

Antecedent topography influences localized deposition (Bergman et al., 2010), and thus, the resulting depositional geometries. On the finest seismically resolvable scale of individual channels (10s m), pre-existing topography visibly affected the system. Slope channels are stacked throughout the study interval where the pre-existing topography of a channel is the seed point for the next generation of channels at the same location in x-y space (Fig. 7). We argue that a larger-scale control, such as a change in slope angles, is necessary to overcome the influence of existing sediment avenues and induce abandonment of stacked channel pathways. Low slope angles during SS5 and SS9 correlates with a stable position of vertically stacked channels. Subsequent sea level induced steepening of slope angles beyond 9° during SS6 and SS10 initiated the incision of new slope channels and a shift in the position of sediment avenues (Fig. 15).

Overall, our findings conform to work by Bosence (2005), indicating that both tectonic setting and relative sea level changes are key controls on passive margin carbonate system development. While tectonically-controlled large-scale antecedent topography determines the basin geometry, the signal of relative sea level overprints the effect of intermediate-scale and small-scale antecedent topography in the study area. This is in agreement with work by Hine and Mullins (1983), who attributed major shape and orientation of large-scale features, such as the shelf relief, to tectonism, whereas geometries of smaller scale features, such as channel pathways, were attributed to be mainly controlled by relative sea level changes.

II.7. Summary and Conclusions

The Upper Oligocene through Lower Miocene carbonate system in the Browse Basin is a distally steepened carbonate ramp with steep slopes of up to 12º containing abundant slope channels. The succession of continental-scale clinoforms exhibits thick, laterally continuous slope deposits, which are only bypassed during phases slope system re-organization due to slope channel incision at average slope angles greater than 10º. We reconstructed the signals of subsidence and relative sea level from 3D seismic data by applying seismic geomorphology and ramp margin trajectory analyses. The match between reference data and our seismically derived signals indicates a good preservation of the subsidence and relative sea level signals in the data.

Relative sea level changes ultimately determined the character of basinward sediment transport and lateral variability of the ramp margin of the Upper Oligocene

through Lower Miocene carbonate ramp in the Browse Basin. Progradation, aggradation, and slope angles were controlled by changes in relative sea level. Slope angles greater than the angle of repose initiated the incision of new slope channels, which created lateral variability in the ramp margin trajectory.

We designed the cumulative channel cross sectional area (CCCSA) as a quantitative seismically-derived parameter and interpret it to be a proxy for the equilibrium between basinward sediment flux and available flux capacity of the channel system. CCCSA analysis offers a novel way of parameterizing carbonate slope systems and their stability. Moreover, CCCSA analysis sheds light on how basinward sediment transport reacts to allogenic and autogenic controls by highlighting phases of autogenic slope system re-organization in response to changes in relative sea level.

Large-scale antecedent topography of the basin geometry determined the northwest progradation of the Browse Basin ramp. However, relative sea level overprinted the effect of intermediate-scale and small-scale antecedent topography. Paleocene topographic features were not inherited by the system and the influence of small-scale antecedent topography of the slope channels was ultimately overcome by the effect of relative sea level changes on slope angle.

III - MODIFICATION OF THE RECIPROCAL SEDIMENTATION MODEL IN PERMIAN UPPER SAN ANDRES MIXED CLASTIC-CARBONATE CLINOFORMS, LAST CHANCE CANYON, NM

III.1 Synopsis

Integration of field-based geological data and drone-based photogrammetry produced a 3D digital model of the mixed carbonate-siliciclastic clinoforms of the Upper San Andres Formation (Upper Permian), Last Chance Canyon (LCC), Guadalupe Mountains, NM.

We introduce a modification to the traditional reciprocal sedimentation model in the Permian Basin based on outcrop observations and modeling results with. As opposed to the traditional lowstand siliciclastic and highstand carbonate dichotomy, our modification proposes uninterrupted sediment production of the carbonate factory in a "refugio" position, away from the avenues of sand input during fifth-order relative sea level drops. Our modeling results reveal a locally persistent, large-scale (~2 km wide) paleo-topographic low, the "Wilson Canyon Chute", in Last Chance Canyon that created mixed siliciclastic-carbonate clinoforms whereas coeval carbonates outside the chute entirely lack siliciclastic facies. The Wilson Canyon Chute most likely served as preferred avenue for basinward siliciclastic sediment bypass and deposition during fifth-order relative sea level lowstands.

Clinoform progradational extent was as great as 800 m, and slope angles were as great as 18˚. Our investigation of slope angles, progradation, and aggradation in 3D

reveals, for the first time, the significant along-strike variability in LCC clinoform geometries. Intermediate-scale (~300 m wide, ~25 m deep) slope channels within the lower slope and bottomset portion of the clinoforms served as possible basinward sediment transport pathways for siliciclastic sediment within the fifth-order LST and TST. Clinoform-internal facies partitioning between siliciclastic bottomset and carbonate topset facies was dominantly controlled by low-amplitude (~10 m), fifth-order relative sea level variations, antecedent topography, and slope channel incision.

III.2 Introduction

A key challenge of geological field work is to capture the three-dimensionality of stratigraphic units. Outcrop topography oftentimes presents geometries that are artifacts of the projection of three-dimensional stratigraphic relationships into a two-dimensional cross section. Digital outcrop modeling is a valuable method to visualize complex 3D stratigraphic relationships, which are not apparent in traditional 2D representations (McCormick et al., 2000). Last Chance Canyon (LCC) comprises multiple canyons that expose 2D sections through the prograding mixed carbonate-siliciclastic clinoforms of the Late Permian Upper San Andres Formation (Sonnenfeld, 1991a). The complex geometry of dip-parallel, strike-parallel, and oblique canyon walls in LCC can lead to a distortion in the perceived clinoform geometries in the field. By creating a geological model, we removed this geometrical distortion and reconstructed the 3D geometries of seven clinoforms in LCC.

Since the 1940's, LCC served as a prominent study area in the focus of changing sedimentological and stratigraphic research focus from lithostratigraphic analysis to sequence stratigraphy to digital outcrop analysis. Lithostratigraphic studies with focus on fossil content and age correlation of strata exposed in LCC were conducted by Boyd (1958); Darton and Reeside Jr (1926); Hayes (1959); King (1942); Skinner (1946). Subsequent studies by Harrison (1966); Jacka et al. (1968); McDermott (1983); Naiman (1982); Williams (1969) focused on interpreting depositional environments of the lithologies in LCC. With the rise of the sequence stratigraphic method in the late 1970's, research emphasis shifted towards depositional facies, large-scale stratal geometries and the seismic-scale sequence stratigraphic framework of LCC strata (Sarg and Lehmann, 1986a, b). Sonnenfeld (1991b) provided the foundation of the current understanding of high-resolution sequence stratigraphy, volumetric partitioning, and facies differentiation of the San Andres strata exposed in LCC. Subsequent work modified basic 2D geometries and lithological facies (Sonnenfeld and Cross, 1993), and demonstrated that LCC can serve as analogue for San Andres reservoirs in the Permian Basin (Dutton et al., 2005; Galloway et al., 1983; Kerans et al., 1994). Phelps and Kerans (2007) and Phelps et al. (2008) used LIDAR-based digital outcrop analyses in LCC to study channel levee complexes and lateral facies continuity in the carbonate clinoforms, while geophysical studies investigated the link between depositional geometries and petrophysical properties on seismic response (He et al., 2016; Kenter et al., 2001; Kenter et al., 1997; Stafleu and Sonnenfeld, 1994).

So far, the comprehensive body of research in LCC collapsed field measurements from throughout the study area into 2D profiles that do not capture the along-strike variability of the Upper San Andres mixed siliciclastic-carbonate clinoforms (e.g. Kenter et al., 2001; Sonnenfeld, 1993; Stafleu and Sonnenfeld, 1994). Moreover, previous studies invoke the traditional model of reciprocal sedimentation (carbonate-dominated highstand and siliciclastic-dominated lowstand) in the Permian Basin (Van Siclen and Merriam, 1964; Wilson, 1975) to ascribe the volumetric partitioning between carbonate topsets and siliciclastic foresets and bottomsets in the LCC clinoforms to changes in relative sea level (e.g. Sonnenfeld, 1993; Sonnenfeld and Cross, 1993). However, these approaches do not explain the contemporaneous existence of mixed siliciclastic-carbonate clinoforms and pure carbonate clinoforms in LCC, nor do they capture the 3D complexity of clinoform geometries and facies partitioning.

The objective of this study is to address these shortcomings and augment previous research in LCC to answer two key questions: 1) How did relative sea level changes and antecedent topography affect the 3D geometrical variability and carbonate vs. siliciclastic facies distribution in LCC? 2) How can we reconcile the presence of mixed siliciclastic-carbonate clinoforms in the eastern part of LCC (Wilson Wall) with the presence of coeval, pure carbonate clinoforms in the western part of LCC (Whiteoaks Canyon)? This study integrates traditional geological field work (e.g. rock samples, measured sections, thin sections, hand-held GR profiles, 2D photomosaics) with drone-based photogrammetry to create a 3D geological model of LCC that honors outcrop descriptions and extrapolates realistic 3D clinoform geometries and siliciclastic

vs. carbonate facies distributions. By doing so, we reconciled the existence of coeval mixed siliciclastic-carbonate and pure carbonate clinoforms by introducing a modification to the reciprocal sedimentation model in the Permian Basin. This modification integrates outcrop observations and modeling results of fifth-order parasequences and includes uninterrupted carbonate production in a "refugio" position, away from the avenues of sand input.

III.3 Geological Setting

Last Chance Canyon is located in Eddy County, ~50 km southwest of Carlsbad, NM (Fig. 18). Paleogeographically, the study area represents the shallow marine shelf to slope transition on the Permian Basin Northwest Shelf (Fig. 19). During the Guadalupian, the shelves of the Permian Basin were dominated by autogenic highstand carbonate rocks, whereas the basin fill comprised lowstand siliciclastic rocks that were likely sourced from the ancestral Rocky Mountains (Fischer and Sarnthein, 1988; Gardner, 1992; Kerans and Fitchen, 1995; Kocurek and Kirkland, 1998). The Guadalupian San Andres Formation was deposited on the Northwest Shelf in an arid, subtropical climate within +/- 5° north of the paleo-equator (Fischer and Sarnthein, 1988; Golonka et al., 1994; Kerans and Fitchen, 1995; Meissner, 1972). Time-equivalent basinal siliciclastic deposits in the Delaware Basin (Fig. 20) are the Cherry Canyon and Brushy Canyon sandstones (Gardner, 1992; Harms and Williamson, 1988; Sarg et al., 1997; Sonnenfeld and Cross, 1993).

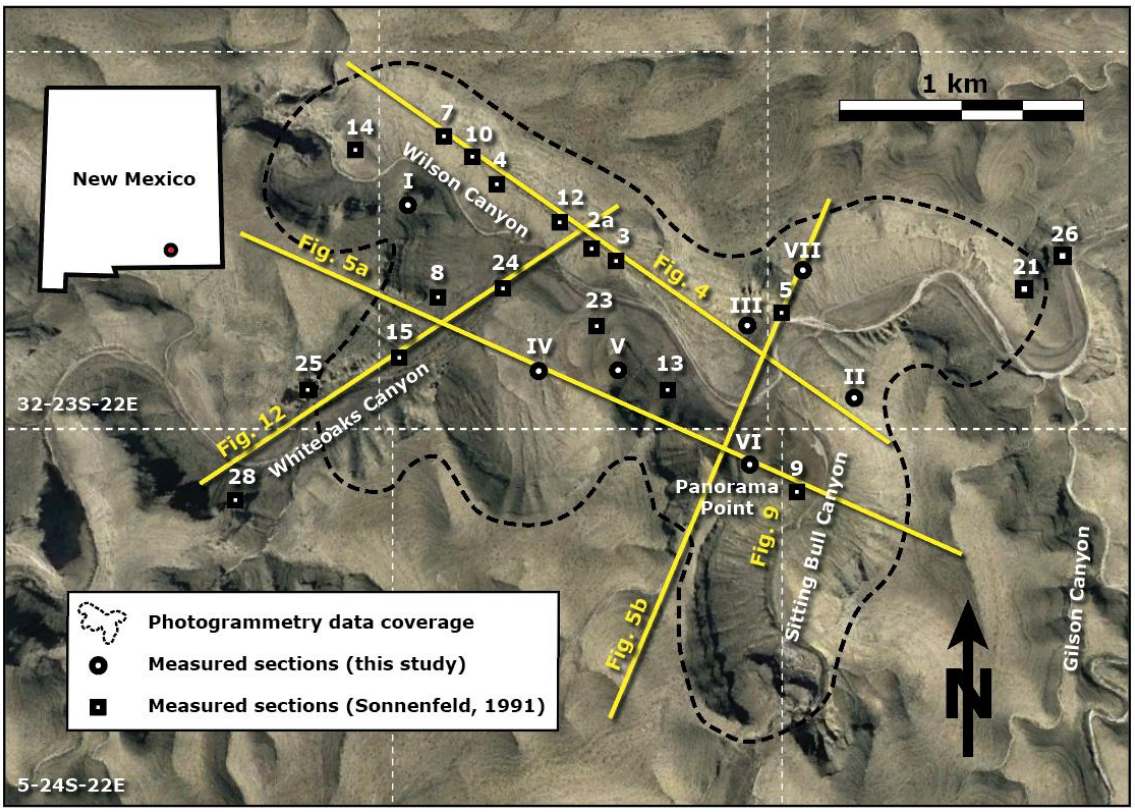

Figure 18: Base map of the Last Chance Canyon study area in southeast New Mexico with outline of photogrammetry data coverage, location of strike and dip profiles (yellow lines), measured sections from Sonnenfeld (1991), and measured sections from this study as ground truth for the reconstruction of 3D clinoform geometries.

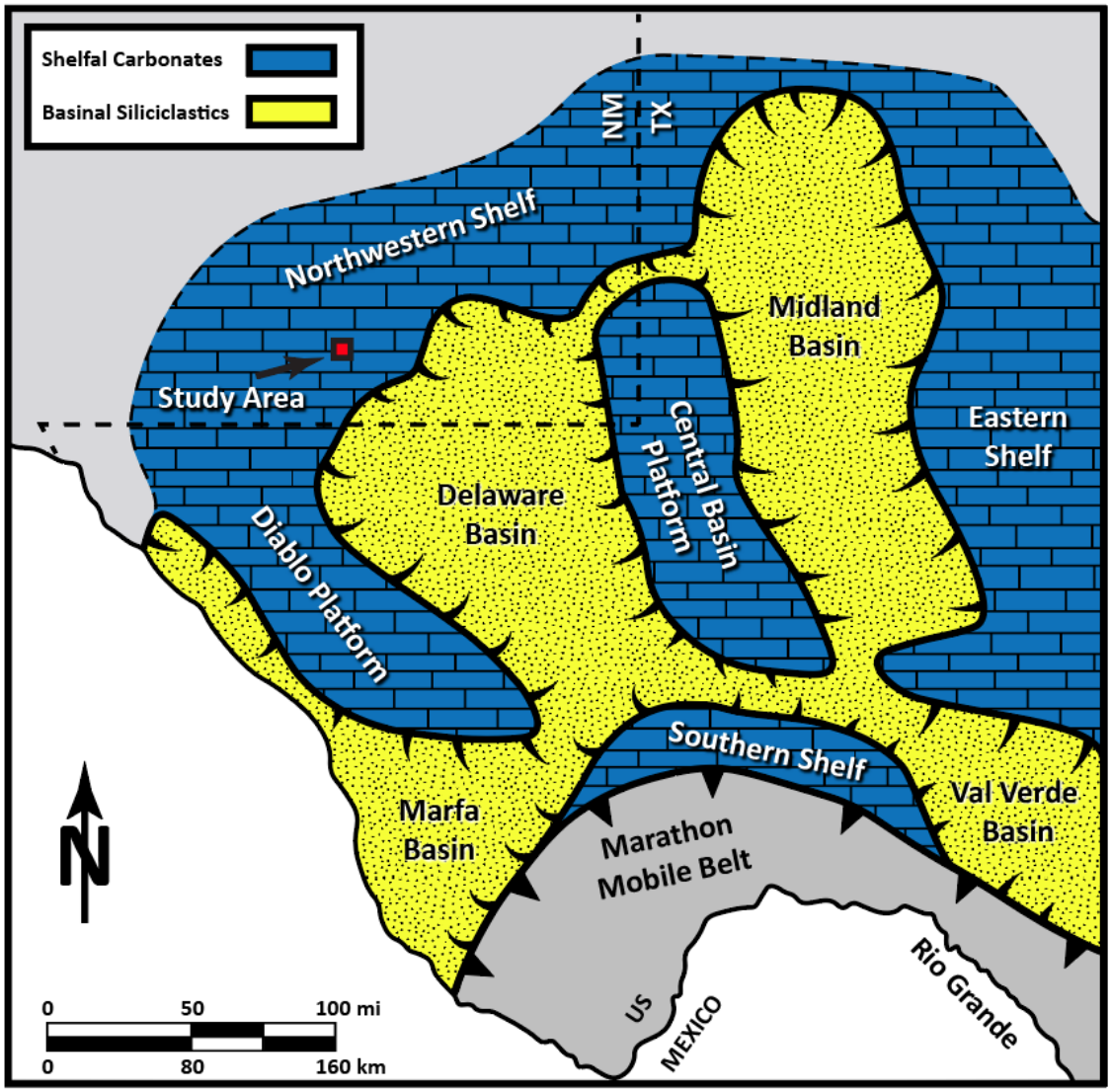

Figure 19: Paleogeographic map of the Permian Basin (modified from Sarg et al., 1999). The study area of Last Chance Canyon is located on the Northwest Shelf of the Delaware Basin in a shallow marine depositional environment.

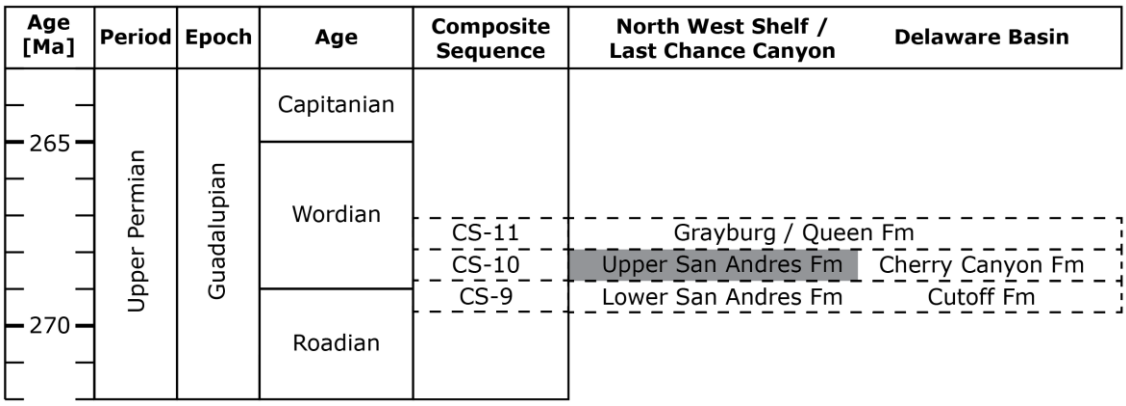

Figure 20: Stratigraphic framework of the Upper San Andres Formation in the Permian Basin (after Sonnenfeld and Cross, 1993; Kerans and Kempter, 2002). Note that the San Andres Fm age boundaries are approximated due to a lack of high-resolution age constraints.

The main structural feature in the study area is the Pennsylvanian Huapache Fault Zone and surface monocline. During the Ouachita-Marathon orogeny, wrench-related compression caused reverse faulting at the Huapache Fault Zone, creating a zone of structural weakness and shaping the paleo-topography (McKnight, 1986). The resulting topography influenced Permian sedimentation patterns and resulted in the east-southeast progradation of the San Andres shelf margin during the Leonardian and Guadalupian (Sonnenfeld and Cross, 1993). Following the Laramide orogeny, Neogene Basin and Range-related normal faulting reactivated the structurally weak Pennsylvanian Huapache Thrust Zone, which formed to the Huapache Monocline but resulted in minimal structural deformation in the easternmost extent of the study area (McKnight, 1983; Phelps and Kerans, 2007).

III.4 Data and Methods

III.4.1 Stratigraphic Framework and Clinoform Definition

We use standard sequence stratigraphic methodology and nomenclature for stratal geometries, stratal terminations, and hierarchical order (Catuneanu et al., 2009; Mitchum et al., 1977a; Mitchum and Van Wagoner, 1991) in our analysis of the mixed siliciclastic-carbonate clinoforms of the Permian San Andres Formation in LCC. Kerans and Kempter (2002) subdivided the Upper Leonardian and Guadalupian strata in the Permian Basin into six "composite sequences" (CS-9 to CS14), which are equivalent to third-order depositional sequences. The Guadalupian Upper San Andres Formation in LCC is of Lower Wordian age (Fig. 20) and represents the carbonate-dominated, fourth-order Guadalupian 8 (G-8) transgressive systems tract (TST) and mixed siliciclastic-carbonate Guadalupian 9 (G-9) highstand systems tract (HST) of CS-10 (Kerans and Fitchen, 1995; Kerans and Kempter, 2002; Sonnenfeld and Cross, 1993). CS-10 marks the transitional stage in the evolution of the Guadalupian Permian Basin carbonate platform from low angle ramp to rimmed shelf geometry. Focuses of this study are six 5^{th}-order G-9 HST parasequences (C1-C6) that form mixed siliciclastic-carbonate clinoforms in LCC (Fig. 21). Our six reconstructed clinoforms are the equivalent of high-frequency cycles 5-10 of Sonnenfeld and Cross (1993). The HST clinoforms are bounded at the base by the third-order CS-10 MFS and are capped by the unconformity (third-order sequence boundary) between the San Andres and overlying Grayburg formations (Kerans and Kempter, 2002). The "Hayes Sandstone" is a prominent white sandstone marker bed near the base of the Grayburg Formation that is considered an

originally near horizontal surface (Sonnenfeld and Cross, 1993) and is thus used as datum for our reconstructed clinoform geometries.

Our field observations are captured in seven measured sections and ten annotated photomosaics that contain stratigraphically relevant information, such as lateral and vertical clinoform boundaries, and major facies contacts. Sonnenfeld (1991b) and Phelps et al. (2008) gave detailed descriptions of the carbonate and siliciclastic facies, facies contacts, and stratal terminations of the LCC clinoforms, which are broadly summarized here:

Fifth-order lowstand systems tract (LST) deposits comprise primarily siliciclastic sediment and carbonate skeletal fragments from channel lag deposits towards the base of the clinoforms that onlap against the lower slope.

Clinoform bottomsets and lower foresets are characterized by sand-on-sand contacts of siltstone to fine sandstone.

Fifth-order TST deposits consist of siliciclastic sediment onlapping against the slope of the clinoforms.

Along the clinoform upper foresets and topsets, the fifth-order maximum flooding surface (MFS) separates siliciclastic sediment below from carbonate sediment above. In the lower slope and bottomset part of the clinoforms, the MFS is challenging to identify due to alluvium and subtle sand-on-sand contacts.

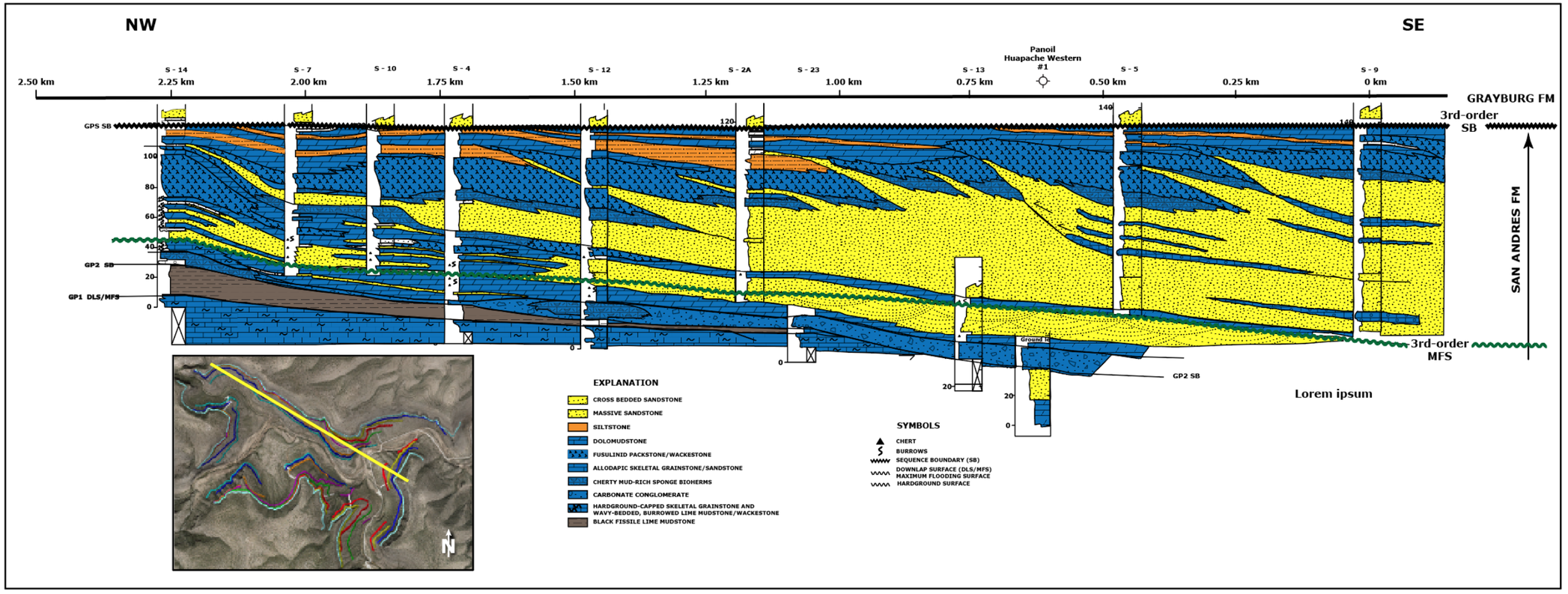

Figure 21: Simplified dip profile through the prograding mixed carbonate-siliciclastic clinoforms in Last Chance Canyon (modified from Sarg et al., 1997; original cross section by Sonnenfeld, 1991). The individual clinoforms represent 5th-order parasequences of the Upper San Andres Formation.

Fifth-order highstand systems tract (HST) deposits comprise primarily subtidal carbonate facies (e.g. fusulinid peloidal packstone, cherty brachiopod-fusulinid wackestone) downlapping onto the fifth-order siliciclastic LST and TST facies.

It is important to note that the mixed siliciclastic-carbonate HST clinoforms are considered fifth-order parasequences (Phelps et al., 2008; Sonnenfeld and Cross, 1993), which are separated by fifth-order sequence boundaries (Sonnenfeld and Cross, 1993). Clinoform geometries are mainly controlled by fifth-order relative sea level variations (Phelps et al., 2008) that tend to have a lower amplitude than third-order sea level variations (Kerans and Tinker, 1997). Since there are no indicators of subaerial exposure in the Upper San Andres Fm strata in the study area (Sonnenfeld and Cross, 1993), we estimate the amplitude of fifth-order relative sea level variation during deposition of the clinoforms to be ~10 m. Furthermore, we argue in this study that clinoform-internal facies partitioning between siliciclastic bottomset and carbonate topset facies is dominantly controlled by fifth-order sea level variations and antecedent topography.

III.4.2 Photogrammetry

We acquired 3,100 drone-based photographs of LCC using a DJI Phantom IV Pro drone and followed a digital outcrop modeling workflow similar to previous studies (e.g. Amour et al., 2013; Hodgetts, 2013; Rarity et al., 2014). The drone-integrated GPS system marked latitude, longitude and elevation of each photograph (lateral accuracy of 2 m and a vertical accuracy of less than 10 m). Camera orientation during photograph acquisition was vertical with a resulting resolution of 5.5 x 5.5 cm per pixel.

Photographs were taken with an overlap of 80 – 90 % to ensure a good stitching result during the photogrammetry processing. We acquired 40 ground control points with a hand-held GPS unit in the field and identified 182 additional ground control points in Google Earth Pro to quality control the accuracy of the resulting photogrammetry-based digital elevation model (DEM). We imported the photographs into the Agisoft photogrammetry software package and generated a DEM of the study area with an overall accuracy of < 0.5 m laterally and < 3 m vertically, relative to Google Earth Pro. The high resolution DEM consists of ~800 million points with x, y, z (latitude, longitude, elevation), and RGB values. In the next stage, we transferred a point cloud of the Agisoft DEM with ~3.5 million points into Petrel to create the digital outcrop model (DOM) that contains geological ground truth from field observations and serves as base for the 3D surface modeling and geometric analysis of the clinoforms. In the final stage of the photogrammetry workflow, we draped a satellite image over the Petrel point cloud to display the present day topography of the DOM in color.

III.4.3 3D Surface Modeling and Geometric Analysis of Clinoforms

In the initial stage of the surface modeling workflow, we transferred the geological ground truth of stratigraphically significant surfaces (e.g. major facies contacts, lateral and vertical clinoform boundaries) from our measured sections, annotated photomosaics, and further 16 measured sections from Sonnenfeld (1991b) into the LCC DOM. Subsequently, we mapped the clinoform boundaries (fifth-order parasequence boundaries) along the canyon walls throughout the area covered by the

DOM as input for the 3D clinoform reconstruction. In addition, we mapped the siliciclastic-carbonate facies contacts in the DOM to reconstruct the volumetric distribution of carbonate and siliciclastic strata in the study area, and to calculate the carbonate/clastic volume ratio for individual clinoforms. All modeling results are based on and limited to outcrop measurements and observations acquired during this project and previous studies, as specified above.

As base surface for the clinoform reconstruction, we created the Upper San Andres third-order maximum flooding surface (MFS) and used it as a trend surface to build the subsequent clinoforms. By using a base surface as trend surface for reconstructing the overlying clinoform surface, we mimicked natural sedimentation that deposits sediment onto antecedent topography. Clinoform break points or rollovers represent the increase in slope angle at the transition from shelf topset to slope foreset and were used to calculate progradation and aggradation of the reconstructed clinoforms. Clinoform rollovers were recognized in the fusulinid peloidal packstone facies of each parasequence (Phelps et al., 2008). The fusulinid peloidal packstone facies served as a proxy for a paleo-water depth of 10-20 m (Ross, 1983; Sonnenfeld and Cross, 1993). To compensate for compaction since deposition of the Hayes Sandstone and minor Tertiary Huapache Fault Zone structural deformation in the eastern part of the study area, we flattened the reconstructed clinoforms on the base of the Hayes Sandstone as datum.

We performed all geometrical calculations (dip angles, dip directions, progradation, aggradation) on the clinoforms after flattening on the overlying Hayes Sandstone datum. Using trajectory analysis (e.g. Helland-Hansen and Hampson, 2009;

Henriksen et al., 2009), we translated the vertical component of the clinoform rollover trajectory as aggradation or downstepping, and the horizontal component of clinoform rollover as progradation or retrogradation. To capture along-strike variability in the clinoform rollover trajectory and clinoform geometries, we measured clinoform progradation and aggradation along 10 dip parallel profiles (DL1- DL10; with a 50-m spacing) that are located between Wilson Wall and Panorama Point.

III.5 Results and Discussion

III.5.1 Clinoform Geometries

Clinoforms C1 to C6 have a height of up to 140 m and exhibit sigmoidal geometry (Fig. 22a). Modeled clinoforms are thickest near the clinoform rollover, with maximum thicknesses ranging from 36 m in C2 to 68 m in C5. Clinoform isopachs thin shelfward to the northwest and basinward to the southeast. Siliciclastic facies onlap against the clinoform foresets. Along strike, our modeling results indicate stacked, large-scale trough geometries of clinoforms C1-C6 with wavelengths of up to 2 km in strike direction and depths as great as 75 m (Fig. 22b). Siliciclastic facies are thickest in the axis of the trough and thin towards the flanks. The axis of the large-scale trough is oriented along Wilson Canyon and dips east-southeast from the northeast end of Whiteoaks Canyon, toward the confluence of Sitting Bull Canyon and Wilson Canyon (Fig. 22c). Average clinoform dip direction changes slightly from ~125˚ in C1-C3 to ~105˚ in C4-C6. Clinoform slope angles for C1-C6 range from a minimum of 4˚ to a maximum of 18˚, with a trend of progressively increasing average slope angles of

subsequent clinoforms from 7˚ in C1 to 12˚ in C6 (Fig. 23). Slope angles for each modeled clinoform vary significantly along strike; for example, the slope angle of C6 varies laterally between 8˚ and 18˚. In strike-oriented outcrops, we identified multiple siliciclastic slope channels that have a maximum width of 370 m and depths of up to 25 m (e.g. Fig. 25). These dimensions are comparable to those identified by (Sonnenfeld, 1991b; his Fig. 7.24) and (Phelps et al., 2008; their Fig. 24).

Extracted clinoform slope angles from this study (Fig. 23) are systematically higher in our analysis (by 1-3˚) compared to Sonnenfeld and Cross (1993). We attribute this result to the fact that we extracted true dip angles from interrogating the entire 3D clinoform surface, as opposed to averaging dip angles from outcrops that are mainly oblique to true dip. While maximum clinoforms slope angles in this study are 18˚, Scott (2007) reported clinoform slope angles of up to 20˚ based on outcrop measurements. This discrepancy can be explained by our flattening of clinoforms on the Hayes sandstone (regional dip of ~5˚ towards east-northeast) to compensate for post-depositional compaction and deformation, and reconstruct depositional slope angles.

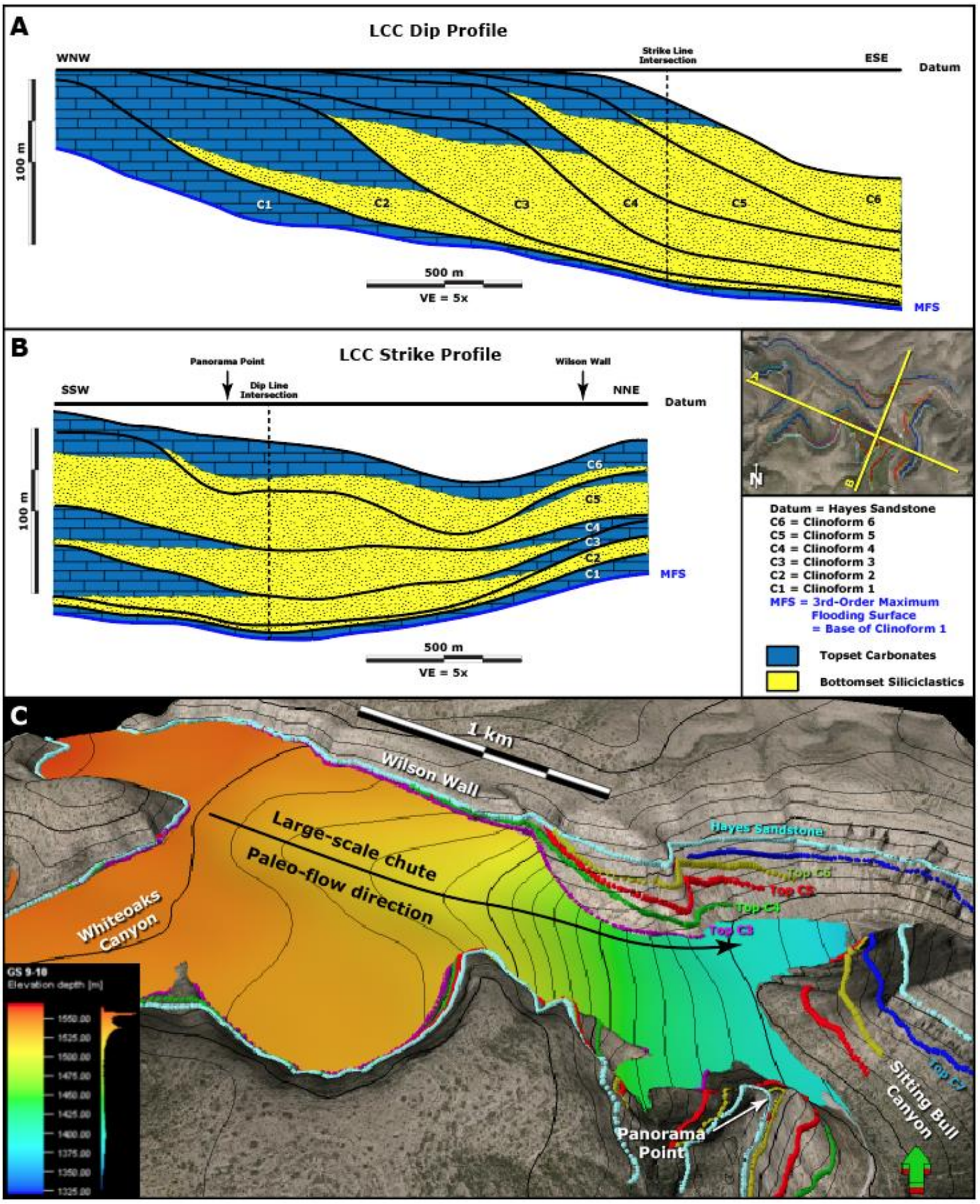

Figure 22: Reconstructed clinoform geometries indicate a large-scale paleo-topographic low that served as preferential sediment pathway for siliciclastic units during fifth-order relative sea level lowstands in the study area. A) Dip profile through LCC hung on the base of the Hayes sandstone as datum and showing the facies partitioning between carbonate topsets and siliciclastic bottomsets with sand-on-sand contacts in our model. 5x vertical exaggeration. B) Strike section through LCC with the Hayes sandstone as datum, showing the trough geometry of clinoforms with siliciclastic fill onlapping the flanks of the chute in our model. 5x vertical exaggeration. C) 3D reconstruction of top Clinoform 3 with a scoop-shaped geometry; clinoform height contour interval = 10 m; present day surface elevation contour interval = 20 m.

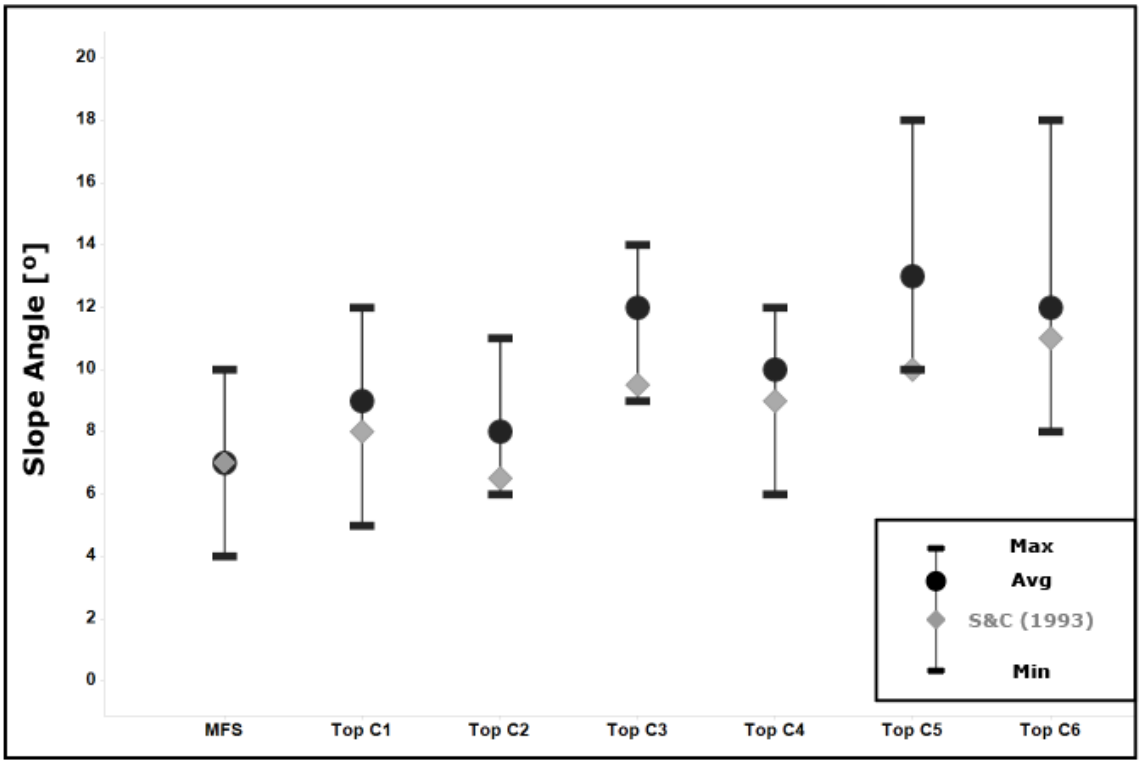

Figure 23: Comparison of clinoform slope angles from this study (black) and Sonnenfeld & Cross (1993; gray). The range of the upper (max) and lower (min) horizontal bars indicates the along-strike variability of slope angles within the individual clinoforms. Note the systematically increasing slope angles from the MFS to Top Clinoform C6.

The flattening tends to decrease resulting clinoform slope angles by ~2˚ compared to field measurements. We interpret the stacked large-scale trough geometries and the distribution of siliciclastic facies as indicators of a locally persistent, large-scale paleo-topographic low in the study area that likely served as chute for basinward siliciclastic sediment bypass during fifth-order relative sea level lowstands.

III.5.2 Progradation and Aggradation

Clinoform progradation and aggradation values were derived from the ten dip profiles DL1 to DL10 after the clinoforms were flattened on the base of the overlying Hayes Sandstone (Fig. 24). Clinoform C1 displays intermediate progradation of ~200 m and strong aggradation of ~ 12 m. Subsequent progradation of Clinoforms C2 and C3 was high (500+ m), whereas the clinoform rollover recorded downstepping of ~3 m. Clinoform C3 has opposing directions of aggradation from 9 m of downstepping to 2 m of aggradation. Clinoforms C4, C5, and C6 prograded ~100 m each and aggraded slightly (~6 m). Overall, our calculated progradation and aggradation ranges match the trend of Sonnenfeld and Cross (1993), although absolute values differ slightly in most cases.

Our results demonstrate up to ~300 m of progradational lateral variability and up to 10 m in aggradational lateral variability of the clinoforms. We attribute the concurrent aggradation and downstepping in the clinoform rollover along strike of Clinoform C3 (Fig. 24b) to the filling of varying accommodation along strike. Clinoform sections that exhibit slope channel incision gain accommodation by losing strata and thus decrease in elevation. Along strike of the same clinoform, areas that are not affected by slope channel incision experience progradation and aggradation as controlled by their antecedent topography, without interruption by channelized erosion.

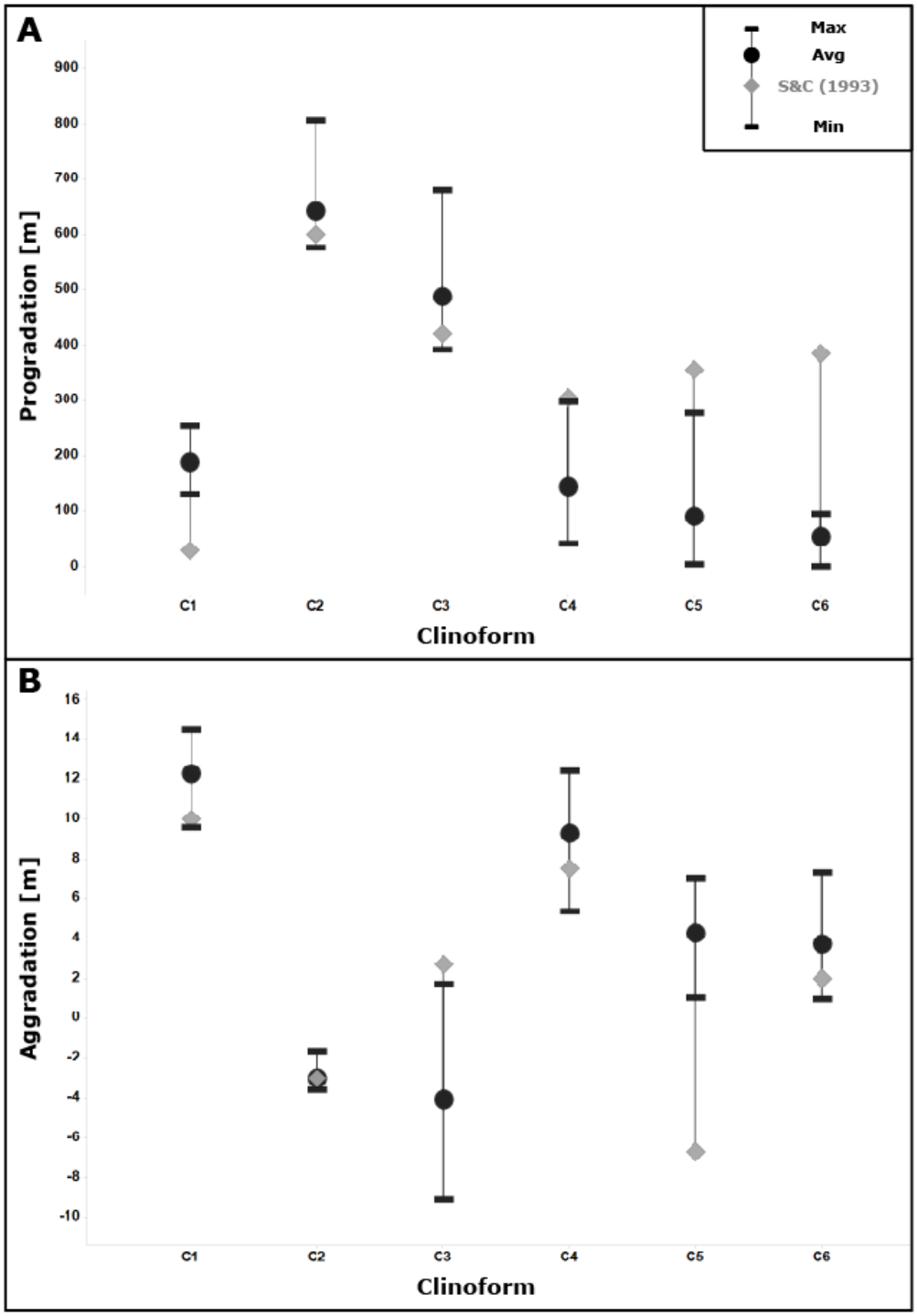

Figure 24: Clinoform progradation and aggradation from this study (in black) calculated along ten dip profiles to visualize the lateral variability. Sonnenfeld & Cross (1993) progradation and aggradation rates (in gray) were derived from their projected 2D dip profile.

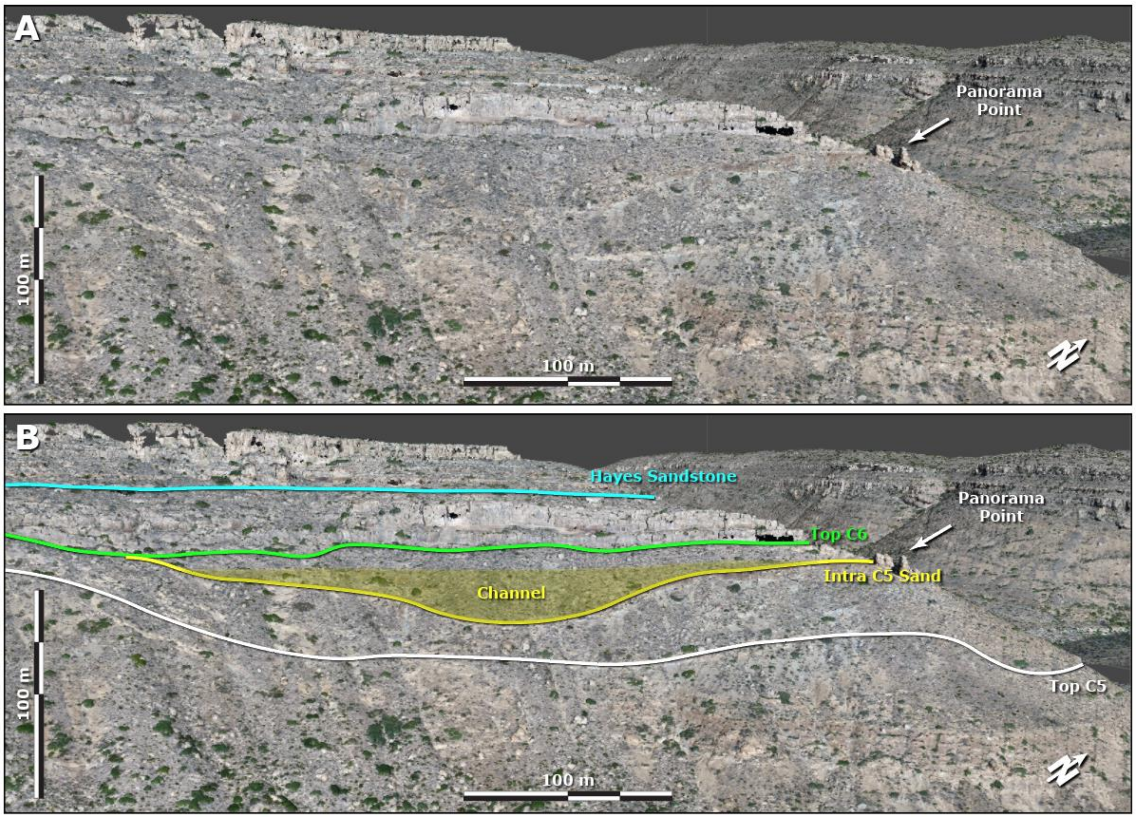

Figure 25: Strike-parallel view of Panorama Point location in the photogrammetry-derived high-resolution digital elevation model. A) Uninterpreted view. B) Interpreted channel geometries and clinoform contacts on the canyon wall. These intermediate-scale channels are located on the upper slope, just below the clinoform rollover. Strike-oriented outcrop cuts of the slope channels have a width of up to 370 m and a depth of up to 25 m.

The derived amplitude of vertical movement of the seven clinoform rollover positions is less than 15 m (Fig. 24b). This amplitude compares favorably to the previously described absence of signs of subaerial exposure of the shallow water carbonate facies (Phelps et al., 2008) and our initial assumption of fifth-order relative sea level variation during the deposition of the HST parasequences to be in the range of ~10

m. In addition, the low absolute aggradational variation and subtle clinoform rollover geometries magnify minor variations in manually picking the rollover position. Considering the subjective nature of clinoform rollover interpretation, this effect can lead to discrepancies in the results of different interpreters. Third-order HSTs generally are characterized by an aggrading-prograding-downstepping stacking pattern (e.g. Neal et al., 2016). The initial high aggradation in Clinoform C1 and subsequent intermediate progradation and low aggradation support the notion that Clinoforms C1 to C6 represent the aggradational to progradational stacking pattern seen in the third-order HST of the Upper San Andres Formation. The intermediate-scale channels within the fifth-order LST and TST siliciclastic deposits represent a second scale of basinward sand transport avenue.

III.5.3 Modification to the Reciprocal Sedimentation Model

The standard model of reciprocal sedimentation in the Permian Basin describes a "carbonate stage" with broad, shelf-rimming carbonate sedimentation and a sediment-starved basin during high relative sea levels (TST and HST), and a "clastic stage" with siliciclastic sediment bypass into the basin during low relative sea levels (LST) (Meissner, 1972; Van Siclen, 1958; Wilson, 1975), without inference on hierarchical order. Kerans and Kempter (2002) adapted the facies partitioning of lowstand siliciclastic and highstand carbonate facies to third-order and fourth-order hierarchy in the large-scale setting of the Permian Basin. In their reciprocal sedimentation model, Meissner (1972), Wilson (1975), and Kerans and Kempter (2002) de facto imply a basin-

wide carbonate factory shut-off during third-order relative sea level lowstands. This discussion focuses on the local fifth-order cyclicity and facies partitioning of strata in Last Chance Canyon, as controlled by relative sea level.

Our modeled clinoform geometries and resulting isopachs indicate a large-scale (~ 2 km wide) paleo-topographic low that dips east-southeast, parallel to clinoform progradation; its axis is in present-day Wilson Canyon (Fig. 22c). The "Lower Gray Sand" below the third-order MFS is an east-southeast trending sand body in the vicinity of the confluence of Wilson Canyon and Sitting Bull Canyon (Fig. 26a), indicating the existence of a paleo-topographic low in LCC prior to the development of the third-order HST clinoforms. The sand thickness map of Clinoform C6 mimics the thickness distribution of the "Lower Gray Sand" with a scoop-shaped geometry and maximum sand thickness of 40 m near Panorama Point (Fig. 26b). In addition, measured sections from previous work indicate that the thick basinal siliciclastic facies of the third-order HST clinoforms in Last Chance Canyon thin southwestward and pinch out into coeval carbonate-dominated clinoforms between Sonnenfeld measured section 25 and 28 (Figs. 18 and 27) (Phelps et al., 2008, Fig. 24; Sarg et al., 1997, Fig. 3-IV-3; Sonnenfeld, 1991b). These carbonate-dominated clinoforms prograde eastward towards the canyon axis and downlap onto older upper-slope siliciclastic foresets, or laterally transition into and downlap onto lower slope and basinal siliciclastic units (Fig. 11).

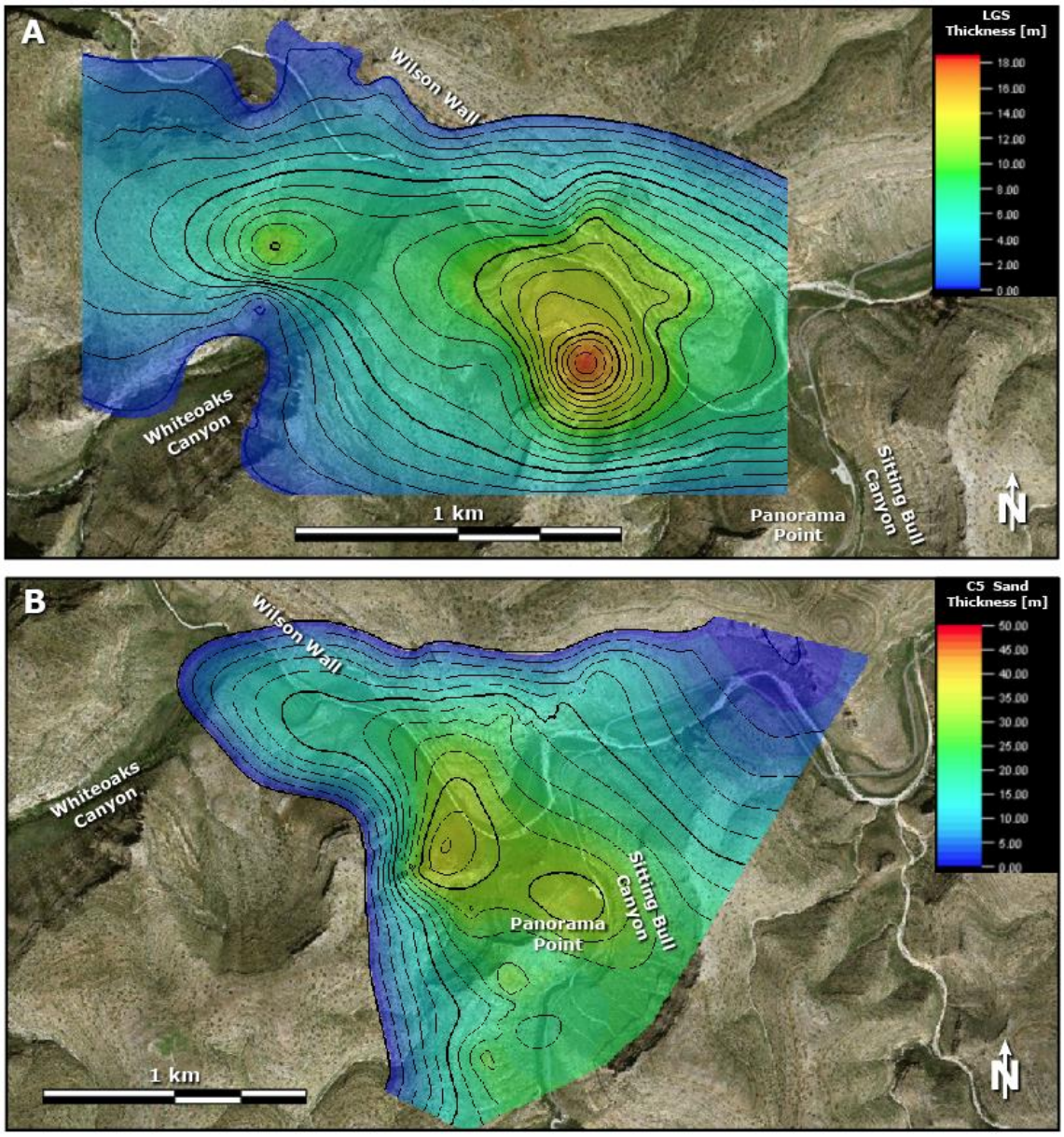

Figure 26: Example of inherited topography and evidence of the large-scale chute in Last Chance Canyon being a paleo-topographic low for preferred siliciclastic bypass. A) Thickness map of the "Lower Gray Sand" below the third-order maximum flooding surface (re-drawn from Sarg et al., 1997). CI = 1 m. B) Clinoform 5 sand thickness. CI = 3 m. The axes of both sand bodies are parallel to depositional dip (WNW-ESE) as indicator for inherited topography.

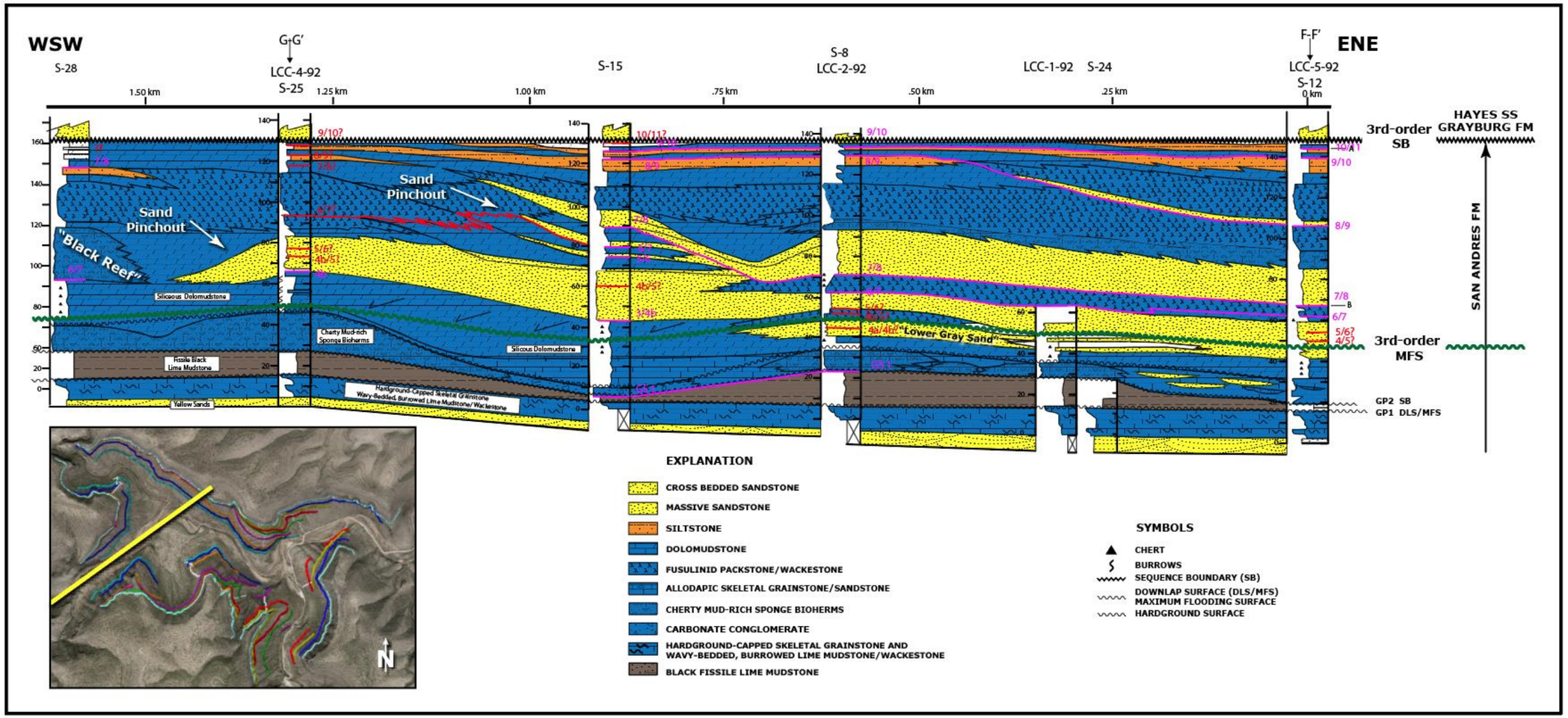

Figure 27: Strike section of LCC indicating thinning and pinch-out of siliciclastic facies towards west-southwest (modified from Sarg et al., 1997, Fig. 3-IV-3).

Based on the above analysis, we argue that internal clinoform facies partitioning between siliciclastic bottomset and carbonate topset facies is dominantly controlled by fifth-order relative sea level variations and antecedent topography. We propose that the Wilson Canyon area of Last Chance Canyon was a large-scale paleo-topographic low or "chute" that served as a preferential pathway for basinward siliciclastic sediment flux during fifth-order relative sea level lowstands. Furthermore, we suggest that the reciprocal sedimentation model for the Upper San Andres clinoforms in LCC, as previously described by Sonnenfeld and Cross (1993), is an artifact of the intermediate-scale 3D sedimentation patterns. Thus, we introduce a modification to the reciprocal sedimentation model that integrates our observations of the fifth-order parasequences and includes uninterrupted sediment production of the carbonate factory in a "refugio" position, away from the avenues of sand input (Fig. 28).

The carbonate factory produced ramp-crest and outer ramp sediment in the form of autochthonous subtidal peloidal grain-dominated packstone, massive peloidal sandstone, fusulinid peloidal dolopackstone, and cherty fusulinid dolowackestone in a paleo-water depth of 0-40 m (Phelps et al., 2008) throughout the LCC area during the fifth-order HST (Fig. 28a). Wilson Canyon region was in a topographically low position and was flanked by promontories towards the southwest and northeast. Shelfal topset carbonate facies prograded and downlapped onto slope and basinal siliciclastic sediments. In the fifth-order LST (Fig. 28b), facies patterns shifted basinward and siliciclastic sediment input from the north was funneled through the large-scale paleo-topographic low in the "Wilson Canyon Chute", disrupting the carbonate factory in the

direct path of sediment flow. Basinal siliciclastic sediments onlapped the clinoform foresets and were themselves channelized by intermediate-scale slope channels. At the same time, the carbonate factory does not shut off laterally, in the paleo-topographically higher promontories southwest of Wilson Canyon. During 5th-order lowstands, we interpret that the carbonate factory retreated laterally out from the Wilson Canyon area and occupied topographically lower positions along strike on older, underlying slope facies, and maintained its normal habitat below sea level. Throughout the fifth-order TST (Fig. 28c), facies patterns shifted landward to a topographically higher position and the carbonate factory moved laterally from the flanks of the promontories back into the Wilson Canyon Chute. Carbonate sediment downlapped the previous LST slope and basinal siliciclastic units toward the chute axis, until a laterally continuous, highstand carbonate factory was re-established.

Previous studies described carbonate factories with significant lateral variability of stratal stacking patterns in carbonate factories of the Maldives and the Australian North West Shelf due to high-amplitude sea level fluctuations (Belopolsky and Droxler, 2004; Betzler et al., 2013; Harper et al., 2015; Tesch et al., 2018). The Great Barrier Reef may serve as a good analogue for the modified reciprocal sedimentation model in Last Chance Canyon.

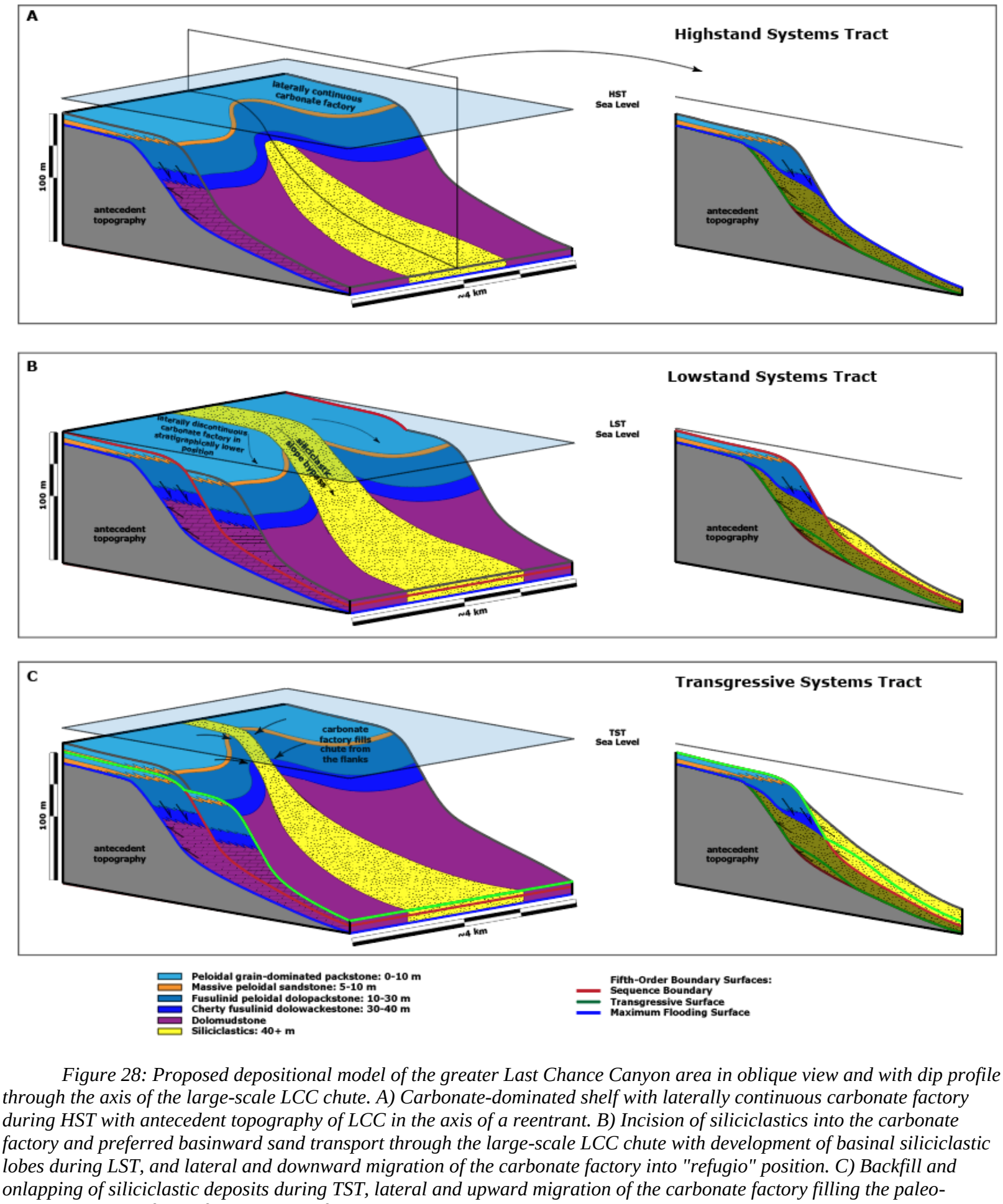

Figure 28: Proposed depositional model of the greater Last Chance Canyon area in oblique view and with dip profile through the axis of the large-scale LCC chute. A) Carbonate-dominated shelf with laterally continuous carbonate factory during HST with antecedent topography of LCC in the axis of a reentrant. B) Incision of siliciclastics into the carbonate factory and preferred basinward sand transport through the large-scale LCC chute with development of basinal siliciclastic lobes during LST, and lateral and downward migration of the carbonate factory into "refugio" position. C) Backfill and onlapping of siliciclastic deposits during TST, lateral and upward migration of the carbonate factory filling the paleo-topographic low of LCC from the chute flanks.

Harper et al. (2015) investigated the response of the mixed carbonate-siliciclastic depositional system in the Great Barrier Reef to high-amplitude, fourth-order relative sea level changes that created lateral variability through channel incision into the reef during the last 150 – 75 kyr. Through the fourth-order relative sea level minimum of MIS-6, the reef was exposed while fringing reefs prevailed in a topographically lower refuge position. During this time, basinward sediment transport consisted of siliciclastic units being funneled through topographic lows between reef mounds (Harper et al., 2015; their Fig. 13a).

III.6 Summary and Conclusion

The objective of this study was to augment previous research in LCC to answer two key questions: 1) How did relative sea level changes and antecedent topography affect the 3D geometrical variability and carbonate vs. siliciclastic facies distribution in LCC? 2) How can we reconcile the presence of mixed siliciclastic-carbonate clinoforms in the eastern part of LCC (Wilson Wall) with the presence of coeval, pure carbonate clinoforms in the western part of LCC (Whiteoaks Canyon)? We integrated traditional geological field work and drone-based photogrammetry in the mixed clastic-carbonate clinoform system of Last Chance Canyon, Guadalupe Mountains, New Mexico, to reconstruct the 3D clinoform geometries and reveal significant lateral variability in progradation, aggradation, and slope angles.

We reconciled our outcrop observations and modeling results with a modification to the traditional reciprocal sedimentation model in the Permian Basin. As opposed to

the traditional lowstand siliciclastic and highstand carbonate dichotomy, our modification proposes uninterrupted sediment production of the carbonate factory in a "refugio" position, away from the avenues of sand input during fifth-order relative sea level drops. Our modeling results reveal a locally persistent, large-scale (~2 km wide) paleo-topographic low, the "Wilson Canyon Chute", in Last Chance Canyon that created mixed siliciclastic-carbonate clinoforms whereas coeval carbonates outside the chute entirely lack siliciclastic facies. The Wilson Canyon Chute most likely served as preferred avenue for basinward siliciclastic sediment bypass and deposition during fifth-order relative sea level lowstands.

Clinoform progradational extent was as great as 800 m, and slope angles were as great as 18˚. Our investigation of slope angles, progradation, and aggradation in 3D reveals, for the first time, the significant along-strike variability in LCC clinoform geometries. Intermediate-scale (~300 m wide, ~25 m deep) slope channels within the lower slope and bottomset portion of the clinoforms served as possible basinward sediment transport pathways for siliciclastic sediment within the fifth-order LST and TST. Clinoform-internal facies partitioning between siliciclastic bottomset and carbonate topset facies was dominantly controlled by low-amplitude (~10 m), fifth-order relative sea level variations, antecedent topography, and slope channel incision.

IV - ADDING THE MISSING THIRD AND FOURTH DIMENSIONS TO TRAJECTORY ANALYSIS IN CARBONATE SYSTEMS

IV.1 Synopsis

We developed a seismic geomorphology-based analysis to enhance traditional trajectory analysis with the ability to visualize and quantify lateral variability along carbonate prograding-margin types (ramps and rimmed shelves) in 3D and 4D. This analysis revealed the effect of far-field tectonic forcing on the large-scale shelf break evolution of the Oligo-Miocene carbonate clinoform system in the Browse Basin and identified the feedback between antecedent topography and carbonate system response as controlling factor on shelf break rugosity.

Our geometrical analysis identified a systematic shift in the large-scale average shelf break strike direction over a transect of 10 km from 62° to 55° in the Oligo-Miocene interval of the Browse Basin, which is likely controlled by far-field allogenic forcing from the Timor Trough collision zone. Plotting of 3D shelf break trajectories represents a convenient way to visualize the lateral variability in shelf break evolution. Shelf break trajectories that indicate contemporaneous progradation and retrogradation correlate with phases of autogenic slope system re-organization and may be a proxy for morphological stability of the shelf break. Ramp margin geometries are neither straight nor uniform through time. Shelf break rugosity and shelf break trajectory rugosity are not inherited, but instead controlled by the intermediate-scale autogenic feedback between antecedent topography and carbonate system response. The autogenic carbonate

system response smooths high-rugosity areas by filling accommodation and maintains a relatively constant rugosity of ~ 150 m. Color-coding of the vertical component in the shelf break trajectory captures the creation and filling of accommodation, and highlights areas of the transect that are likely to yield inconsistent 2D sequence stratigraphic interpretations.

IV.2 Introduction

The use of seismic data in stratigraphic analysis gave rise to seismic stratigraphy, which assigns seismic reflections to timelines and places seismic reflections in a chronostratigraphic framework (Mitchum et al., 1977b). The resulting sequence stratigraphic method uses seismic reflection terminations and seismic reflection geometries to reconstruct depositional systems, predict lithologies (Vail et al., 1977), and make inferences on relative sea level (Mitchum et al., 1977b). Decades of sequence stratigraphic research in a variety of depositional systems led to the development of a nomenclature that mixes observations with interpretations, which Catuneanu et al. (2009) eventually reconciled to standardize the sequence stratigraphic method.

In contrast, the accommodation succession method aims to clearly separate observation from interpretations as an observation-driven approach to sequence stratigraphy, based entirely on geometric relationships of strata to gain insight into sequence boundary formation (Neal et al., 2016). Similar to the accommodation succession method, trajectory analysis is observation driven and traces the 2D vertical and lateral shelf break or clinoform rollover position through time (Helland-Hansen &

Hampson, 2009; Henriksen *et al.*, 2009). Trajectory analysis and the accommodation succession method represent valuable conceptual variants of the sequence stratigraphic method that do not aim to account for the entire 3D volume of the depositional record, or for along-strike variability in stratal architecture of depositional systems (Madof et al., 2016).

Although previous studies recognized along-strike variability in stacking (Wehr, 1994) and character of bounding surfaces (Martinsen and Helland-Hansen, 1995), 2D dip sections remain the leading method of interpretation in trajectory analysis (Henriksen et al., 2009). Sanchez et al. (2012) highlighted an important limitation of shelf edge trajectory analysis in deltaic systems, namely that only sections near the siliciclastic delta receive sufficient sediment input to record changes in relative sea level. However, this is not the case in carbonate systems, as sediment is produced in place by the carbonate factory, although the amount of produced sediment varies by facies (Schlager, 2005). While there is a solid body of research on the topography of the slope profile (e.g. Adams et al., 2013; Adams and Schlager, 2000; Puga-Bernabéu et al., 2013; Schlager and Adams, 2001), few studies quantified the effect of along-strike variability on interpreted systems tracts and rollover trajectories in 3D (e.g. Gill and Cobban, 1973; Helland-Hansen and Hampson, 2009; Madof et al., 2016). Notably, work by Madof et al. (2016) focused on developing the concept of geometrical hinges to describe a mechanism for along-strike variability in the clinoform rollover trajectory. Differential progradation (sensu Madof et al., 2016) is a morphological approach to describing lateral variability in nearshore settings that conceptualizes the simultaneous progradation and

retrogradation of depositional systems rollover position around a geometrical hinge in map view.

In this study, we introduce a descriptive and observationally-driven workflow to quantify along-strike variability in the clinoform rollover trajectory. Traditional trajectory analysis and the sequence stratigraphic method lack the nomenclature and parameters to account for lateral variability. Therefore, such analysis yields simplified sequence stratigraphic and depositional models that show "straight-line" strike geometry, which are exceptionally rare in reality. More common are prograding carbonate ramp and shelf margins with significant along-strike variability. Given this, traditional trajectory analysis can result in conflicting sequence stratigraphic interpretations of a prograding carbonate system when analyzed in three dimensions. We introduce three parameters to address this shortcoming in the hope of raising more attention to the 3D / 4D complexity of depositional systems in sequence stratigraphic analyses, which can alleviate an interpreter's urge to force-fit data to a pre-conceived simplified model.

Abbreviations:

SB – Shelf break

SBT – Shelf break trajectory

R_{SB} – Shelf break rugosity

R_{SBT} – Shelf break trajectory rugosity

IV.3 Data and Methods

IV.3.1 Browse Basin Seismic Data

The study area (Fig. 29) is located in the Browse Basin on the Australian North West Shelf (NWS). Our study focus was the Brecknock South 3D multichannel seismic volume that covers an area of 287.3 km^2 in the central Browse Basin, at the intersection of the Seringapatam, Barcoo, and Caswell Sub-basins. The original seismic data are time-migrated, zero phase, and follow European polarity (Veritas, 2000). Previous work depth-converted the Brecknock South 3D seismic volume and identified twelve depositional sequences (SS1 through S12) with thirteen sequence boundaries (SB1 through SB13) in the Oligo-Miocene section of the Browse Basin (Tesch et al., 2018), using seismic reflection terminations and seismic reflection geometries (Catuneanu et al., 2009; Mitchum et al., 1977a; Mitchum and Van Wagoner, 1991) to study the architectural evolution of the strongly prograding carbonate clinoforms. Resulting limits of vertical and horizontal resolution in the seismic data at the Oligocene-Miocene boundary are ~15 m and ~30 m, respectively (Tesch et al., 2018). During the Oligocene to Lower Miocene, a distally-steepened, strongly channelized heterozoan carbonate ramp developed in the Browse Basin (Reuning et al., 2009; Rosleff-Soerensen et al., 2012; Tesch et al., 2018). Age constraints from previous studies place the time duration for the thirteen depositional sequences at ~1.4 – 1.8 Myr/sequence (Belde et al., 2017; Rosleff-Soerensen et al., 2012; Tesch et al., 2018). Accommodation fill in the study area was dominated by autogenic sediment production of the cool-water carbonate factory with

negligible amounts of siliciclastic sediment during the Oligo-Miocene (Rosleff-Soerensen et al., 2012; Tesch et al., 2018).

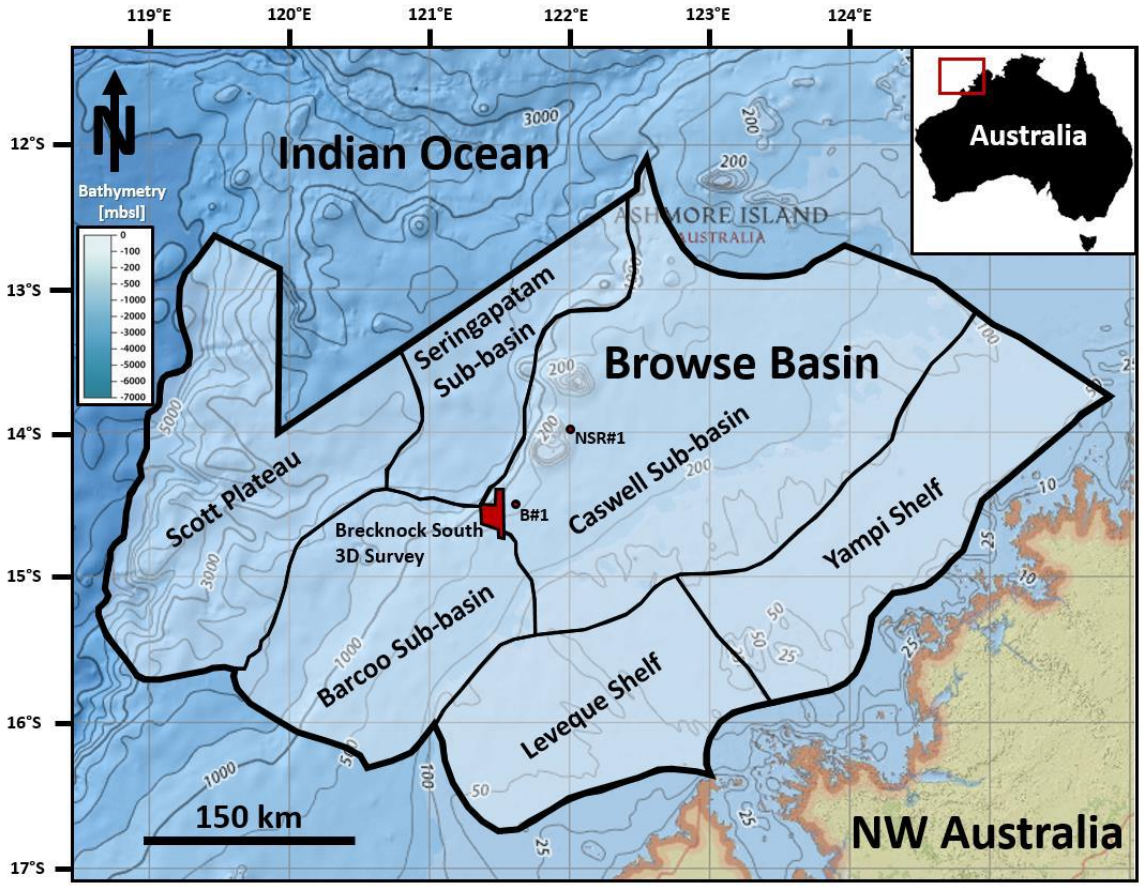

Figure 29: Location of Browse Basin on the North West Shelf of Australia with location of the Brecknock South 3D Seismic Survey in red (from Tesch et al., 2018).

IV.3.2 Shelf Break Parameterization

Shelf breaks and shelf break trajectories are the two key morphological features that form the building blocks of our analysis (Fig. 30). The shelf break or clinoform rollover in the dataset is identified by a marked increase in seismic reflection dip angle (e.g. Wiseman and Ovey, 1953) from gently dipping shelfal reflections of < 2˚ to steeper slope reflections at a dip angle of > 4˚. The shelf break trajectory describes the lateral and vertical movement of the shelf break in a sedimentary system through time (e.g. Helland-Hansen and Hampson, 2009; Henriksen et al., 2009).

This study introduces three parameters and a workflow to quantify shelf break lateral variability through time. In the initial stage of the parameterization workflow, we interpreted the shelf breaks of sequence boundaries SB3 to SB12 manually on 3D clinoform surfaces. To aid the manual interpretation of the shelf breaks in 3D, we color-coded the surfaces with the dip angle attribute, highlighting the transition from gently dipping shelfal reflections to steeper slope reflections at a dip angle of ~4˚. Each 3D shelf break for the ten studied clinoforms consists of approximately 2,000 points along a transect of ~10 km (Fig. 31a).

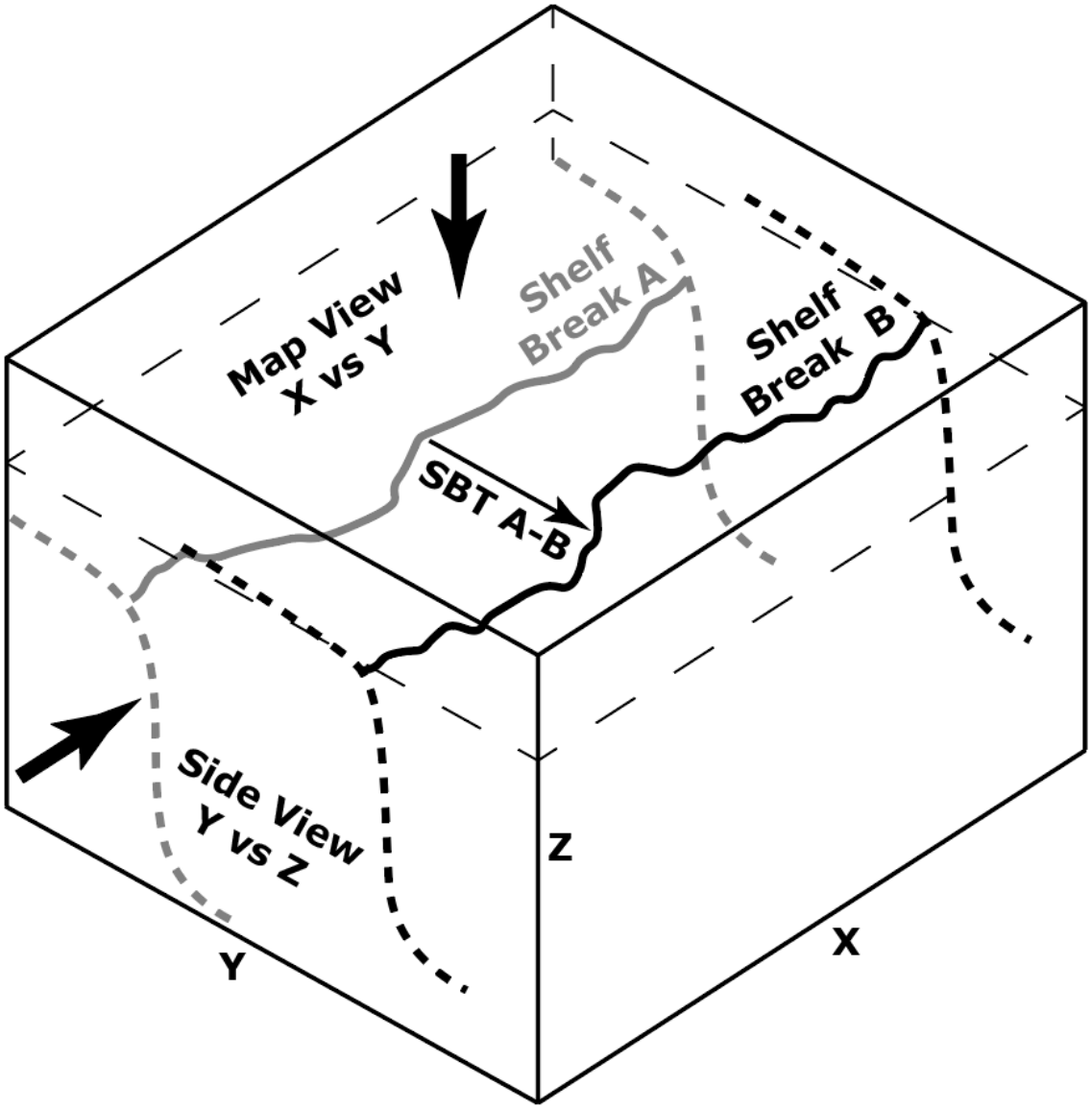

Figure 30: Block diagram illustrating the three-dimensionality of clinoform shelf breaks and shelf break trajectories (SBT). X vs. Y map view visualizes the shelf break evolution through time and along strike. Shelf break trajectories are calculated as the difference in Y values between two successive shelf breaks to quantify the rugosity or along-strike variability in progradation and aggradation of the margin between consecutive time intervals A and B. Y vs. Z side view represents a dip profile and depicts the s- or z-shaped geometry of clinoforms. We collapsed 3D shelf breaks onto the Y vs. Z plane (e.g. Fig. 6) as another way to visualize lateral and vertical variability in the shelf break. This provides a detailed insight into 3D shelf break complexity, unlike traditional 2D profiles.

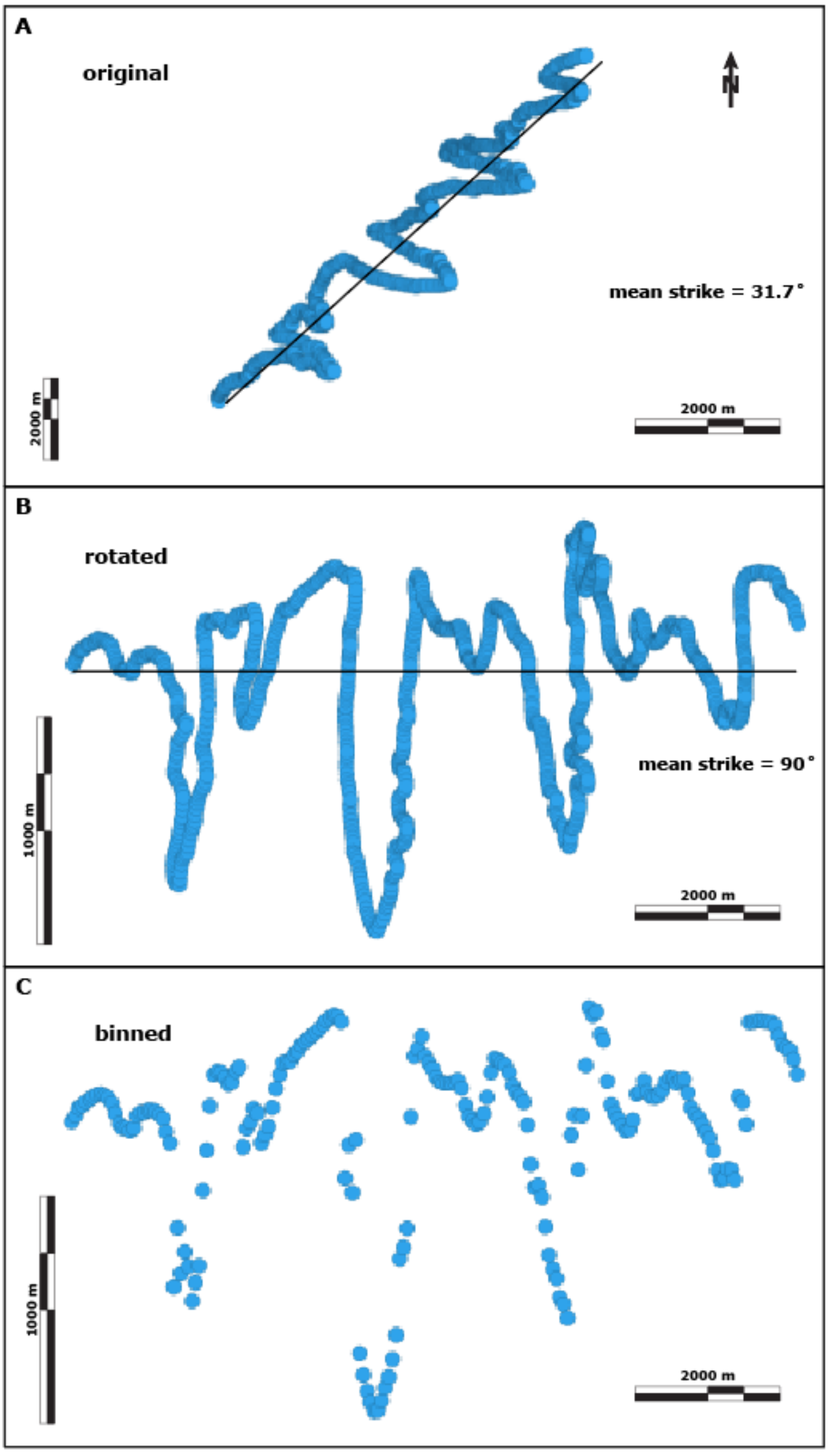

Figure 31: Map view of interpreted shelf break SB3. A – original shelf break orientation with average strike direction of 31.7 degrees. B – shelf break rotated by 58.3 degrees to align mean strike line in a horizontal direction. This rotation simplifies the calculation of progradation relative to a previous position in x/y space. C – shelf break binned laterally into 200 bins of 50 m size covering the full 10 km transect to ensure a normalized sampling rate along the profile.

The first parameter is the slope of the shelf break mean-line (M_{SB}), denoting the average strike direction of the shelf break.

Equation 4:

$$M_{SB} = arctan\ \frac{\sum(x-\bar{x})(y-\bar{y})}{\sum(x-\bar{x})^2}$$

Where x and y are the x, y values of each map view data point for the shelf break. Fluctuations in M_{SB} through time highlight changes in the large-scale progradation direction of the depositional system as controlled by allogenic and/or autogenic parameters.

To simplify the calculation of shelf break progradation perpendicular to strike, we rotated all shelf break points in Petrel to a 90° strike direction of the oldest shelf break (Fig. 31b) and clipped the data laterally to ensure all shelf breaks have the same lateral extent. A subsequent stage of the workflow compensates for varying point density from manual shelf break interpretation and ensures an equal lateral sampling rate by averaging the shelf break measurements laterally into 50 m bins (Fig. 31c). This methodology allows for an efficient analysis of the shelf edge trajectory along 200 dip directional profiles. Ultimately, the bin size determines the lateral resolution of the analysis and needs to be sized appropriately to capture the geomorphological features of interest. This study employed a lateral bin size of 50 m to capture the prominent slope channels that created lateral shelf edge variability by incising into the shelf edge with a width of ~300 – 1,100 m (Tesch et al., 2018).

We adapted a parameter that is used in materials science for measuring surface roughness (e.g. Black and Kohser, 2017) to design the shelf break rugosity parameter

(R_{SB}). R_{SB} quantifies the along-strike variability of a given shelf break as the deviation of shelf break geometry from an idealized line source in all three spatial dimensions (Fig. 32a).

Equation 5:

$$R_{SB} = \frac{1}{n} * \sum_{i=1}^{n} |\bar{Y} - Y_i|$$

Where n = number of lateral bins = 200; $\bar{Y}$ = average y value of the shelf break; Yi = distance between i^{th} data point perpendicular to the average line. R_{SB} yields the average distance (in meters) of the interpreted shelf break points away from the shelf break mean line. In effect, R_{SB} quantifies the average amplitude of shelf break rugosity, or the dissimilarity of the shelf break from a line source. A perfectly straight line has an R_{SB} = 0.

The third parameter is shelf break trajectory rugosity (R_{SBT}). We calculate the shelf break trajectory as the difference between the y values of a given shelf break and the y values of the subsequent shelf break perpendicular to strike. R_{SBT} quantifies the rugosity or along-strike variability in progradation and aggradation of the margin between consecutive time intervals A and B, or between successive stratigraphic sequences (3D evolution through time = 4D). The rugosity of the resulting trajectory is compared to uniform progradation along a dip profile.

Equation 6:

$$R_{SBT} = \frac{1}{n} * \sum_{i=1}^{n} |\bar{Y}_{A-B} - (Y_{i_B} - Y_{i_A})|$$

Where n = number of lateral bins = 200; $\bar{Y}_{A-B}$ = average y value of shelf break trajectory A-B; Y_{iA} = y value of i^{th} data point on shelf break A; Y_{iB} = y value of i^{th} data point on shelf break B; (Fig. 32b)

All three parameters and our workflow were applied to a passive-margin carbonate clinoform system to capture and quantify along-strike changes in progradation and aggradation of the stratigraphic sequences, allowing for more realistic, accurate spatio-temporal characterization of the clinoform margin evolution, geometries, and sequence stratigraphic models. We recognize the potential scale-dependence of the average strike direction, shelf break rugosity, and shelf break trajectory rugosity parameters. Future research needs to investigate the effect of increasing or decreasing the bin size on the resulting values in the calculation of our parameters. Depending on the self-similarity of the shelf breaks, the resulting values may change in a predictable way, similar to fractal patterns described in the coastline paradox (Mandelbrot, 1983; Plotnick et al., 1996).

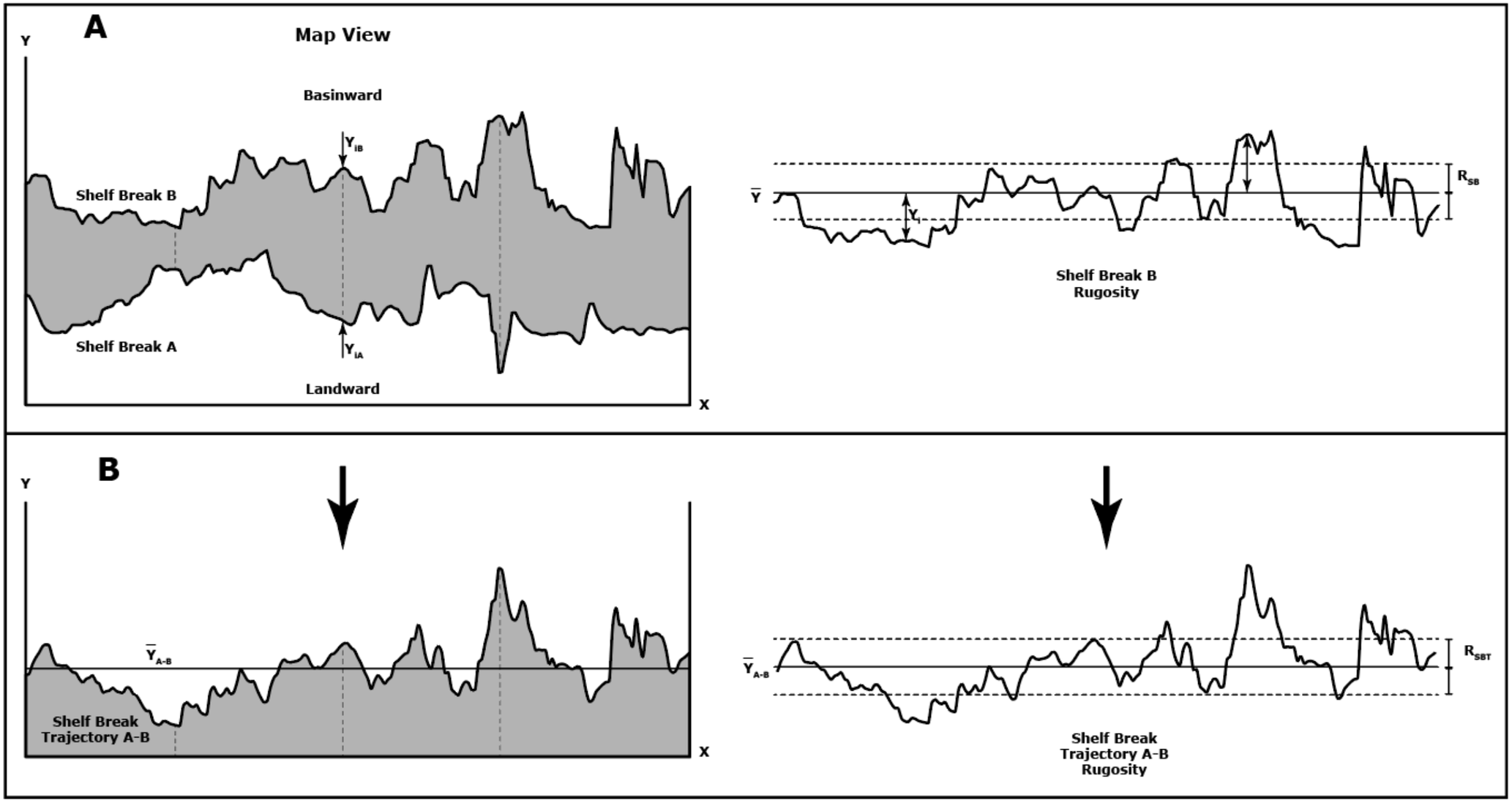

Figure 32: A) Map view of two successive shelf breaks (shelf break A and Shelf break B). B) Shelf break B with visualized mean Y value ($\bar{Y}$) and shelf break rugosity (RSB) as average deviation from the mean line. C) Map view of shelf break trajectory between shelf break A and shelf break B. D) Shelf break trajectory A-B with visualized mean Y value and shelf break trajectory rugosity (RSBT).

IV.4 Results

The average strike direction of shelf breaks SB3 to SB12 ranges from 55° to 62° with a trend of decreasing strike angle through time from 62° in SB4 to 55° in SB12 (Fig. 33). We collapsed the 3D shelf breaks and shelf break trajectories onto the Y vs. Z axis to visualize both lateral and vertical variability (Fig. 34). Average y and z values for shelf breaks and shelf break trajectories in this display are shown as circle, vertical and lateral minimum and maximum values are indicated by error bars. Longer error bars correspond to higher variability in shelf break and shelf break trajectory rugosity. In side view, the average shelf break position for SB3 to SB12 has a step-wise evolution (Fig. 34a). In the first step, SB3 to SB5 are strongly progradational (1,400 m – 1,700 m) at a relatively constant depth of ~2,450 m. During the second step, SB6 to SB9 prograde slightly less (800 m – 1,300 m) at a lower depth of ~2,350 m. In the last step, SB10 and SB12 aggrade (100 m and 54 m) and prograde (~750 m and ~1,500 m), whereas SB11 aggrades ~90 m and retrogrades ~70 m. We plotted shelf break trajectories in four quadrants (I-IV) around the coordinate origin (= zero progradation, zero aggradation relative to the previous shelf break position) in order to better visualize the variability in progradation and aggradation of the SBTs: I – progradation and aggradation; II – retrogradation and aggradation; III – retrogradation and downstepping; IV – progradation and downstepping (Fig. 34b). Generally, SBTs that experience high progradation exhibit low aggradation or downstepping, whereas sections of the profile that experience the least progradation (or retrogradation) exhibit the strongest aggradation. Shelf break trajectories are mostly progradational with a minor

aggradational or downstepping component and plot in quadrants I and IV. SBT 5-6, SBT 8-9, and SBT 10-11 have stronger aggradation and less progradation than the other SBTs. Only SBT 10-11 and part of SBT 5-6 plot in quadrant II, showing a major aggradational and minor retrogradational component. SBT 3-4, SBT 6-7, SBT 7-8, and SBT 8-9 cross over between quadrants I and IV, designating contemporaneous aggradation and downstepping along strike.

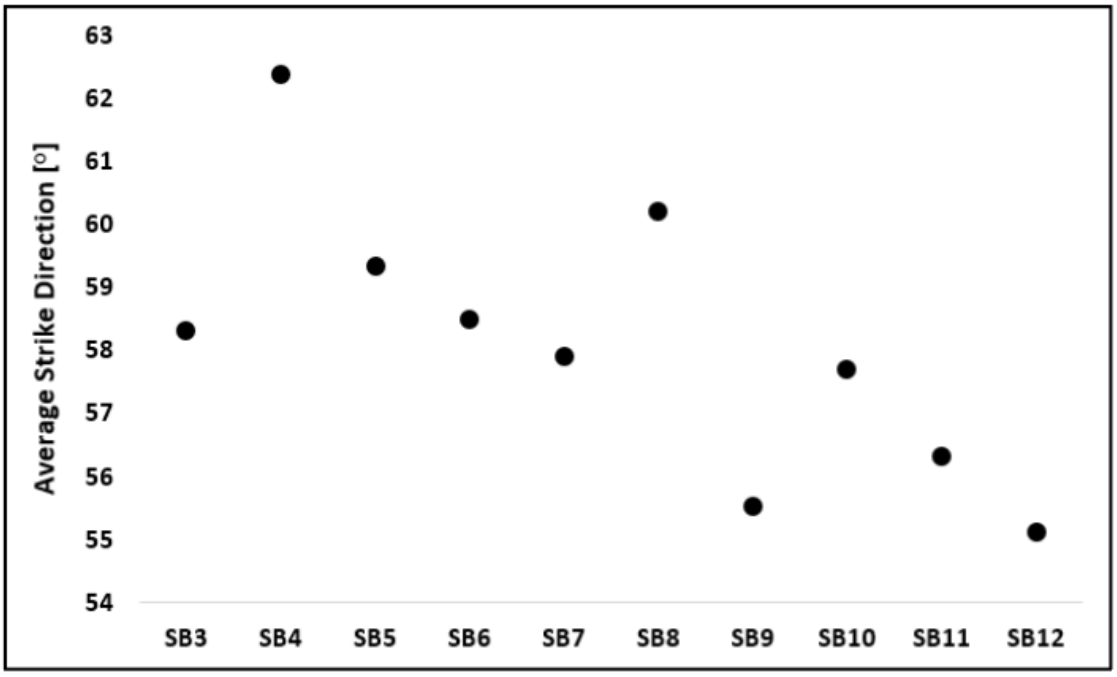

Figure 33: Average strike direction of shelf breaks SB3 to SB12 progressively decreased from ~60° to ~55°. We attribute the progressive shift in average strike direction to allogenic tectonic forcing from the collision of Australia with the Timor Plate and resulting differential subsidence in the Browse Basin during the Oligo-Miocene.

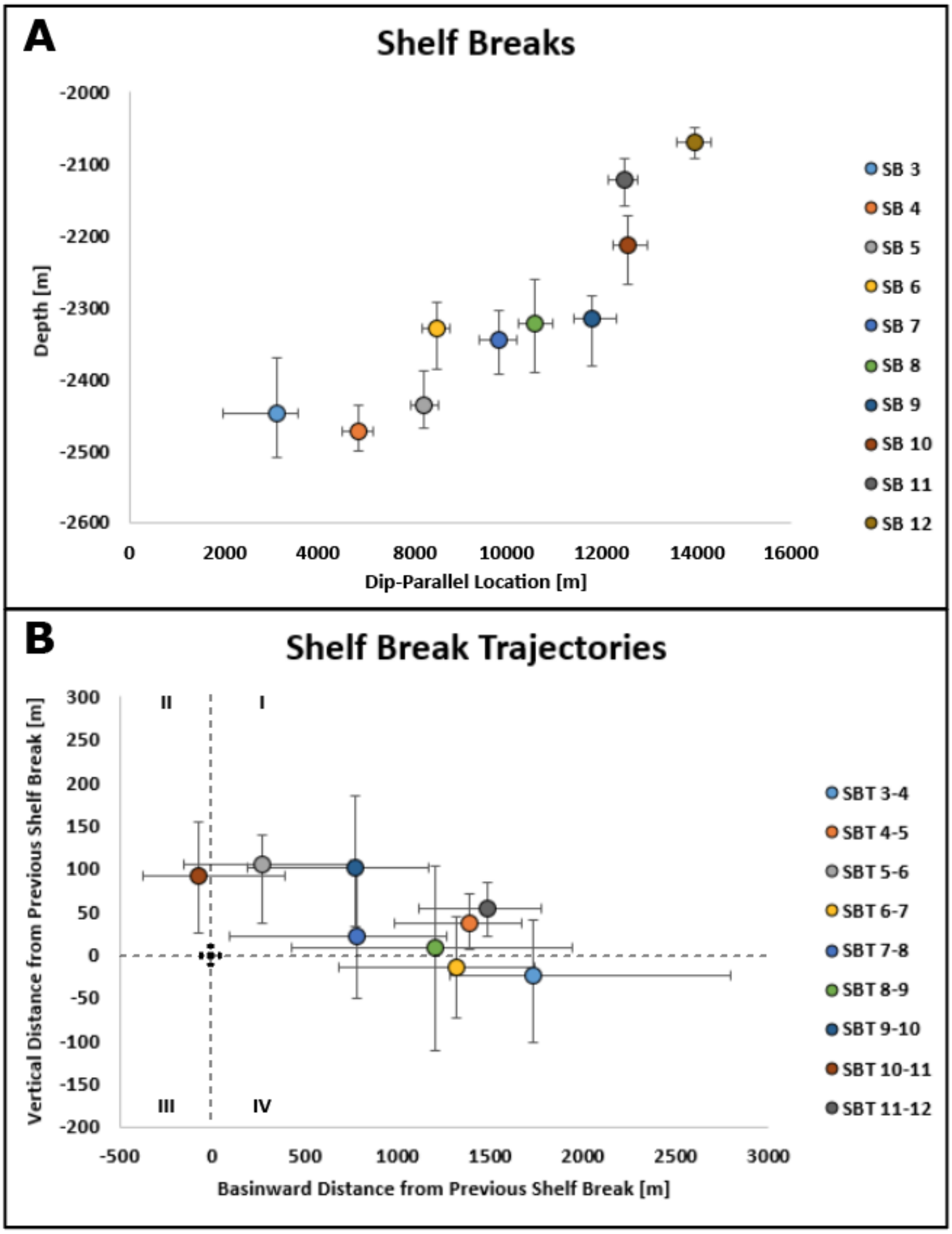

Figure 34: SB and SBT diagrams with error bars indicate basinward and vertical minimum and maximum values. Shorter error bars indicate lower rugosity. A) Side-view (Y vs Z) of the ten shelf break positions SB3 to SB 12 through time. B) Side-view (Y vs Z) of the nine shelf break trajectories SBT 3-4 to SBT 11-12. The 0, 0 coordinate origin designates the position of the previous shelf break for each of the shelf break trajectories. Quadrant designate: I – progradation and aggradation; II – retrogradation and aggradation; III – retrogradation and downstepping; IV – progradation and downstepping. If the error bars are crossing sector boundaries, contradictory along-strike stratal stacking patterns can be expected.

We color-coded vertical movement of the SBTs (red = downstepping, blue = aggradation) to highlight the vertical component of differential progradation in the data set (Fig. 35). Parts of the shelf break trajectories undergo a reversal in progradation amplitude through time: sections of the profile that are characterized by strong progradation record low progradation in the subsequent SBT. For example, Bin 135 exhibits the highest progradation of SBT 4-5 (~1,660 m), but the lowest progradation (~-135 m) in the subsequent SBT 5-6. In addition, parts of the SBT indicate a reversal in aggradation amplitude through time. For example, bins 40-70 of SBT 6-7 have strong progradation (~1,600 m) and mild downstepping (~-30 m). In the subsequent SBT 7-8, bins 40-70 have low progradation (~120 m) and high aggradation (~90 m). These progradation and aggradation reversals are common but not a strict rule. Moreover, a general divide between aggradational (blue) and downstepping (red) data points in the SBTs occurs at progradation values of ~900 - 1,500 m. SBTs with a progradation of less than ~1,200 m tend to exhibit no downstepping component, with the exception of SBT 4-5 and SBT 11-12. Shelf break rugosity (R_{SB}) values range from 113 m in SB8 to 256 m in SB3 and average 146 m. Shelf break trajectory rugosity (R_{SBT}) values are slightly higher than shelf break rugosity values, ranging from 115 m in SBT4-5 to 260 m in SBT3-4 with an average of 198 m (Fig. 36a). In order to test the effect of a given shelf break rugosity on the subsequent shelf break rugosity and shelf break trajectory rugosity, we plotted R_{SB} n vs. R_{SB} n+1 (Fig. 36b) and R_{SB} n vs. R_{SBT} n+1 (Fig. 36c). There is a poor correlation between R_{SB} n vs. R_{SB} n+1 ($R^2 = 0.11$) and between R_{SB} n vs. R_{SBT} n+1 ($R^2 = 0.24$).

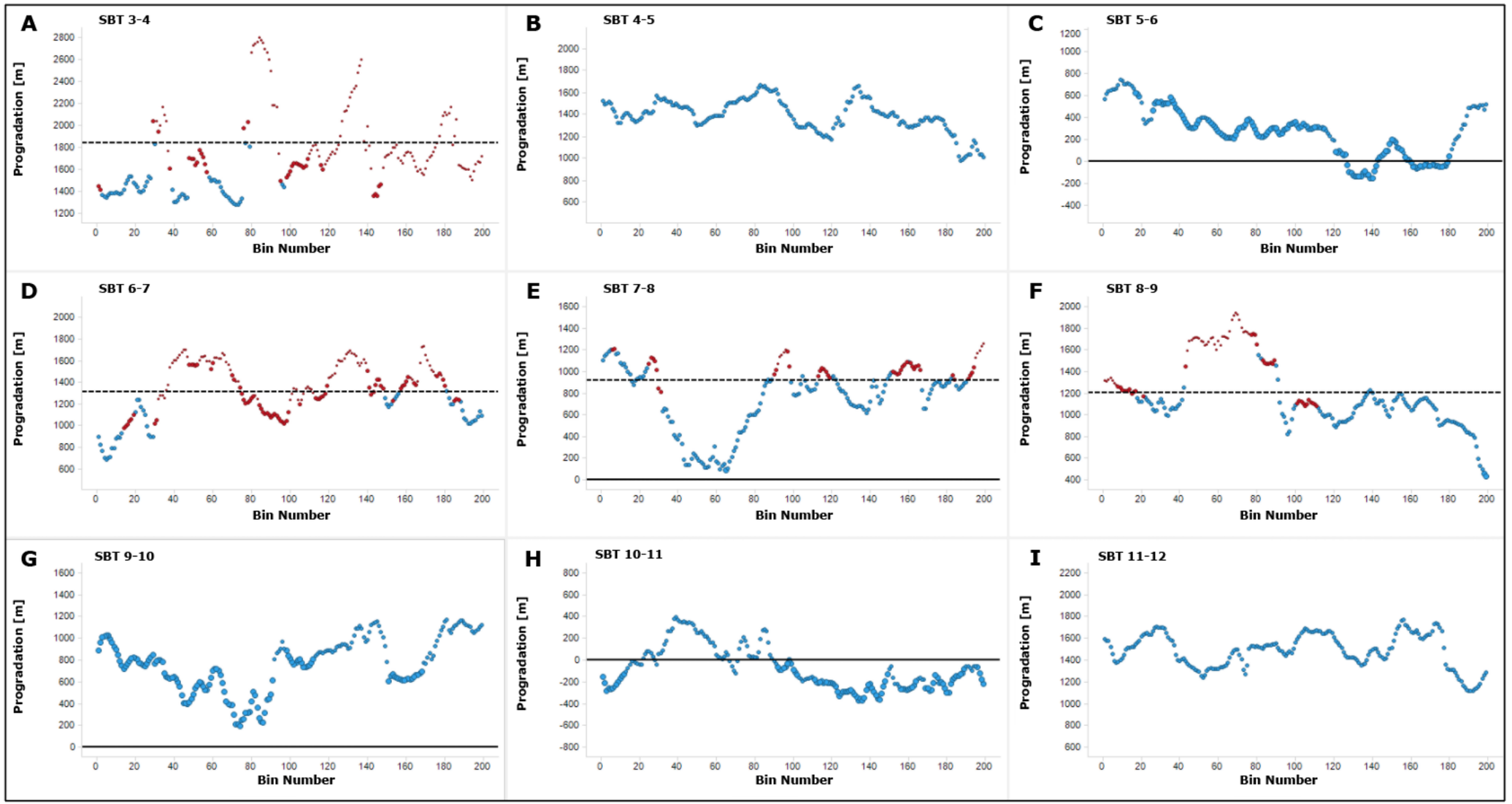

Figure 35: Map view of shelf break trajectories color coded by aggradation (blue) and downstepping (red). Dashed horizontal lines mark the approximate progradation distance at which the shelf break trajectory transitions from aggrading to downstepping. Solid horizontal line marks the zero progradation line. Shelf break trajectories with relatively low progradation tend to be almost entirely aggradational (e.g. B, G, I); some shelf break trajectories display concurrent progradation and retrogradation (e.g. C and G); in general, a divide between aggradational (blue) and downstepping (red) data points in the shelf break trajectories occurs at progradation values of ~900 - 1,500 (e.g. A, D, E, F).

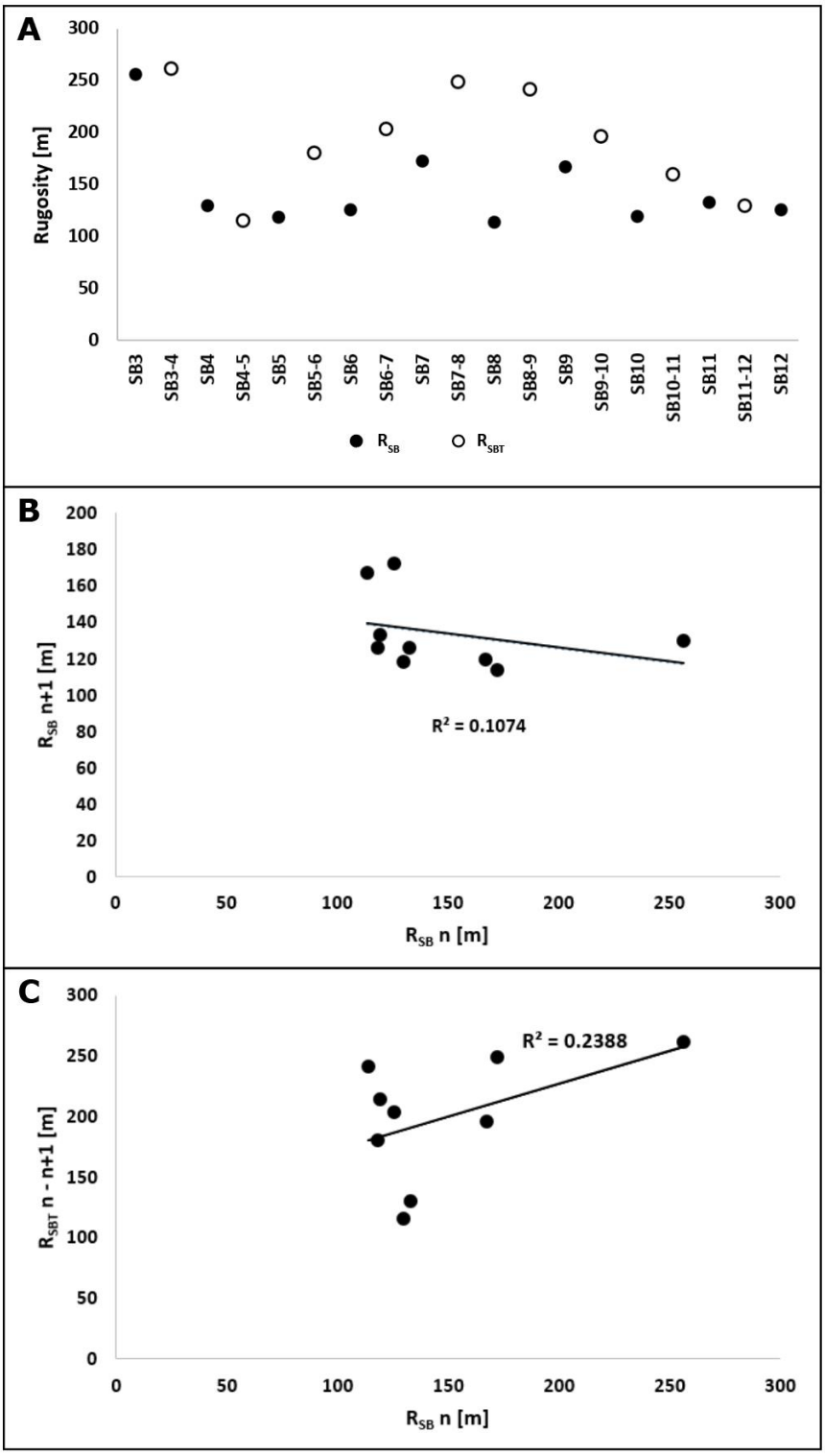

Figure 36: The rugosity value of all shelf breaks and shelf break trajectories ranges between 250 – 100m.

IV.5 Discussion

Our observed shift in average shelf break strike direction along a 10 km wide transect captures large-scale changes in the geometric evolution of the Browse Basin depositional system and could be indicative of a geometrical hinge *sensu* Madof et al. (2016). A significant far-field tectonic forcing factor in the vicinity of the study area was inversion tectonics related to the Miocene-Pliocene Timor Trough collision zone (Hall, 2011; Kennard et al., 2003), ~500 km north of the Browse Basin. This far-field tectonic activity could have triggered northward-increasing differential subsidence in the Browse Basin (Rosleff-Soerensen et al., 2016), causing decreased progradation in the NW of our profile and a resulting shift in average shelf break strike direction from 62° in SB4 to 55° in SB12. Similarly, Rosleff-Soerensen et al. (2016) analyzed the variability of progradation and retrogradation of the Miocene reef complexes in the Browse Basin along a 180 km transect and attributed differential progradation to antecedent topography and local inversion tectonics related to the collision of Australia with the Timor plate. Another example of large-scale tectonic forcing as cause for a geometrical hinge comes from the Santos Basin; Madof et al. (2016) identified a geometrical hinge that caused a shift in the average shelf break strike direction of the Marambaia Formation (from 32° to 28°, and then back to 35° within ~6 Myr during the Ypresian) and attributed the shift to differential tectonic deformation related to hinterland uplift.

SBT 5-6 and SBT 10-11 aggrade strongly along the entire profile and their error bars cross the boundaries between sectors I/II, which records contemporaneous progradation and retrogradation (Fig. 35). SBT 5-6 and SBT 10-11 occur during

autogenic slope system re-organization phases and support the interpretation of Tesch et al. (2018) that the re-organization phases occurred during high relative sea level, since a rise in sea level would increase accommodation and provide space for the carbonate factory to aggrade. During constant relative sea level or a drop in relative sea level, topographic lows may still be filled and aggrade. However, the surrounding topographically higher areas would fill to the bottom of the wave base and then prograde into the basin. The correlation between the SBT 5-6 and SBT 10-11 crossing of the sector I/II boundaries with slope channel re-organization phases might indicate that the sector I/II crossing could be another proxy for morphological stability of the shelf break, as controlled by allogenic and autogenic controls. Further research will need to test this hypothesis in other depositional settings. Overall, the magnitude of the error bars provides a quantification and visualization of along-strike variability and can help interpreters better understand uncertainty in their sequence stratigraphic interpretations. Shorter error bars that do not cross sector boundaries indicate low lateral variability and a more robust the sequence stratigraphic interpretations along strike. Whenever the SBT error bars are crossing sector boundaries, contradictory along-strike stratal stacking patterns can be expected.

Ramp margin geometries are neither straight nor uniform through time. The poor correlation between R_{SB} n vs. R_{SB} n+1 ($R^2 = 0.11$) and between R_{SB} n vs. R_{SBT} n+1 ($R^2 = 0.24$) indicates that the effect of a given shelf break rugosity on the subsequent shelf break rugosity and shelf break trajectory rugosity is negligible. This shows that R_{SB} and R_{SBT} are not inherited parameters in the Browse Basin clinoforms, and that antecedent

topography does not dictate long-term differential movement of the shelf margin through successive depositional sequences. The geometrical reversals in progradation and aggradation capture the creation and filling of accommodation and visualize the autogenic negative feedback between antecedent topography and the carbonate factory (sediment production, delivery and accumulation): areas of high rugosity and/or high accommodation (reentrants) due to slope channelization or minor faulting near the ramp margin are preferentially filled, whereas areas of low rugosity and/or low accommodation (promontories) experience less sedimentation. This interplay acts as high-pass filter to smooth out areas of very high rugosity to maintain the relatively constant shelf break rugosity around 150 m. R_{SBT} can therefore be considered a measure of the smoothing amplitude that is required to maintain the R_{SB}.

When the shelf break trajectory is used as a proxy for changes in relative sea level, along-strike differences in shelf break trajectories can lead to contradictory 2D interpretations (Fig. 37). Red-blue (downstepping-aggrading) color-coding of the vertical component in the SBT captures the creation and filling of accommodation, and highlights areas of the transect that are likely to yield inconsistent along-strike results in the derived sea level curve.

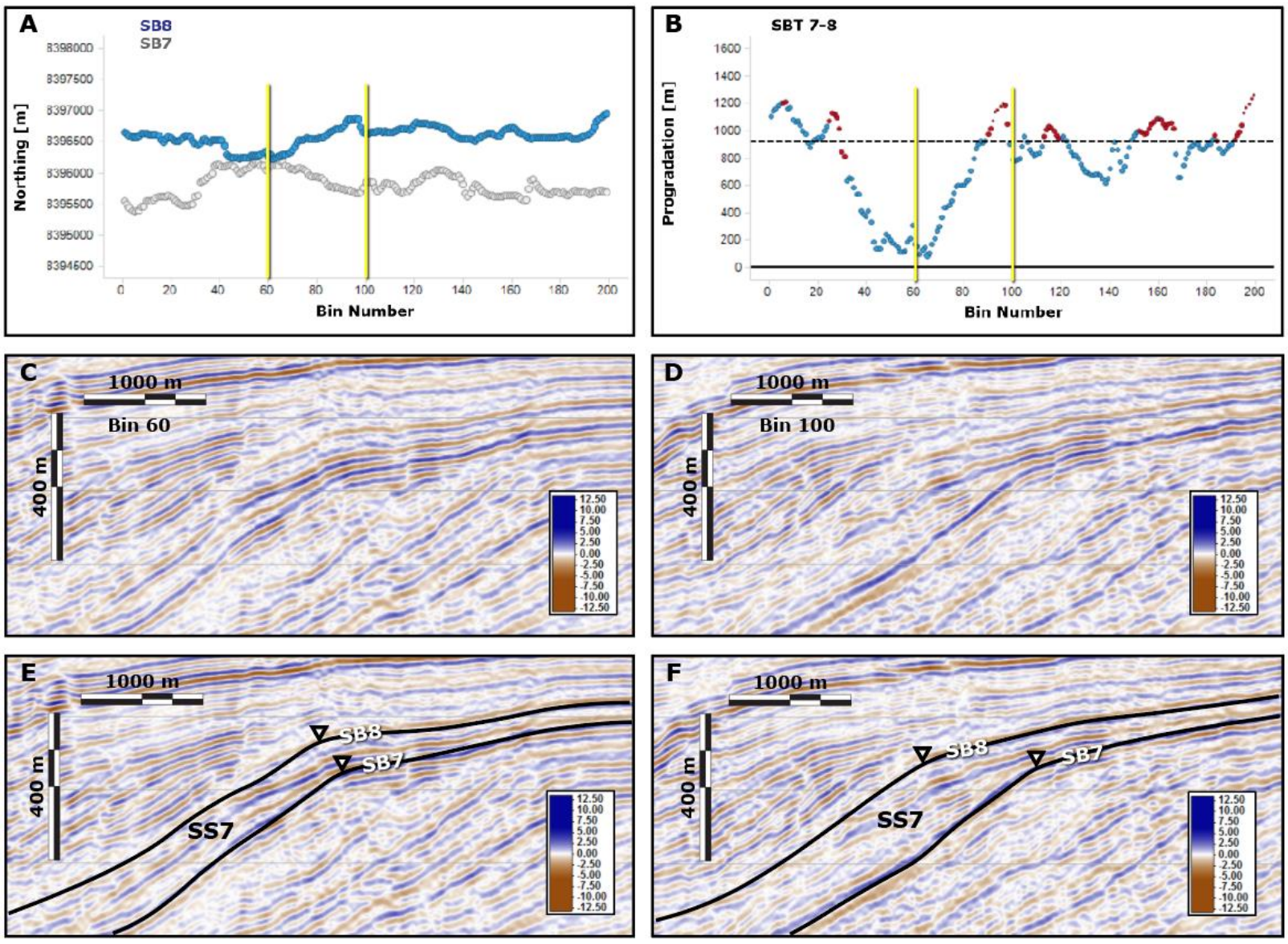

Figure 37: Map view and seismic dip lines visualizing differential progradation of SBT7-8 along bin 60 and bin 100 (= 2 km lateral separation). A) Map view of SB7 and SB8. B) Map view of SBT 7-8 color-coded for aggradation (blue) and downstepping (red). C) Uninterpreted depth-converted seismic dip line along bin 60. Vertical exaggeration = 3x. D) Uninterpreted depth-converted seismic dip line along bin 100. E) Interpreted depth-converted seismic dip line along bin 60 with shelf breaks SB7 and SB8, indicating an aggrading shelf break trajectory with minor progradation. F) Interpreted depth-converted seismic dip line along bin 100 with shelf breaks SB7 and SB8, indicating a prograding shelf break trajectory with minor aggradation.

For example, y values in bin 60 aggraded more than 50 m and prograded less than 200 m between SB7 and SB8. In the same time interval, and only 2 km laterally separated, y values in bin 100 aggraded ~10 m and prograded more than 800 m. The resulting 2D shelf break trajectory of bin 60 would indicate a rise in relative sea level, whereas the 2D shelf break trajectory of bin 100 would indicate a relative sea level still stand. This example illustrates a shortcoming of relying on 2D dip sections in trajectory analysis and, in extension, of using 2D profiles for sequence stratigraphic interpretations. Since lateral variability in sequence stratigraphic interpretations has an impact on the resulting reservoir model, an important industry application of our method could be in the reconstruction of reservoir architecture, with potential applications in risk analysis of reservoir presence and well placement in the field development stage. Moreover, our workflow could provide valuable guidance for subsurface well-to-well correlations when reconstructing subsurface reservoir architecture. By not accounting for lateral variability, resulting sequence stratigraphic and reservoir models may suffer significant inaccuracies in reservoir presence and reservoir continuity.

IV.6 Summary and Conclusion

Our new workflow introduces a descriptive and observationally-driven approach to quantify and visualize along-strike variability in clinoform rollover trajectory analysis by providing the nomenclature and parameters that traditional trajectory analysis and the sequence stratigraphic method lack. This methodology adds the missing third spatial and fourth temporal dimension to trajectory analysis and should be applicable to carbonate

systems with an identifiable shelf or ramp margin, across multiple scales of stratigraphy to analyze strike variability within systems tracts, sequences, and supersequences.

Key findings of this study are:

1) Our geometrical analysis identified a systematic shift in the large-scale average shelf break strike direction in the Oligo-Miocene interval of the Browse Basin over a transect of 10 km. This shift resembles a geometrical hinge, which records large-scale differential progradation of the ramp margin and is likely controlled by far-field allogenic forcing from the Timor Trough collision zone.

2) The plotting of 3D shelf break trajectories represents a convenient way to visualize the lateral variability in shelf break evolution. Shelf break trajectories that plot in both sectors I (progradation and aggradation) and II (retrogradation and aggradation) correlate with phases of autogenic slope system re-organization and may be a proxy for morphological stability of the shelf break. The amplitude of error bars in this display indicates lateral and vertical shelf break variability and the potential robustness of resulting sequence stratigraphic interpretations. Whenever the SBT error bars are crossing sector boundaries, contradictory along-strike stratal stacking patterns can be expected.

3) Ramp margin geometries are neither straight nor uniform through time. Shelf break rugosity and shelf break trajectory rugosity are not inherited, but instead controlled by the intermediate-scale autogenic feedback between antecedent topography and carbonate system response. The autogenic carbonate system response in the Browse

Basin smooths high-rugosity areas by filling accommodation and maintains a relatively constant rugosity of ~ 150 m.

4) Color-coding of the vertical component in the shelf break trajectory captures the creation and filling of accommodation, and highlights areas of the transect that are likely to yield inconsistent along-strike sea level reconstructions derived from the shelf break trajectory. By not accounting for lateral variability, resulting sequence stratigraphic and reservoir models may be oversimplified.

V – DISSERTATION SUMMARY

The objective of this dissertation was to employ seismic geomorphology in the subsurface of the Browse Basin (Australia) and digital outcrop modeling in the Last Chance Canyon (New Mexico) outcrops to develop new analytical quantification and visualization techniques in the investigation of carbonate clinoform systems in 3D and 4D to extract information on the interplay of allogenic and autogenic controls that shape carbonate system architecture and evolution.

In Section II, we introduced cumulative channel cross sectional area (CCCSA) as the product of number of slope channels, slope channel depth, and slope channel width. CCCSA is a seismically-derived parameter that can highlight phases of autogenic slope system re-organization in response to changes in relative sea level. We interpret CCCSA to be a proxy for the equilibrium between basinward sediment flux and available flux capacity of the channel system. CCCSA analysis offers a novel way of parameterizing carbonate slope channel systems and their morphologic stability. Our analysis of 3D clinoform geometries and lateral variability yields new insight into sediment transport that is not apparent from 2D analyses: An increase in relative sea level created accommodation, resulting in increased aggradation of the carbonate system. The aggradation increase steepened slope angles beyond 10º, which, in turn, increased basinward sediment flux beyond the flux capacity of the slope system. This disequilibrium was mitigated by the incision of new slope channels, that increased the slope system flux capacity and created lateral variability in the ramp margin trajectory.

The northwest progradation of the Browse Basin ramp was determined by large-scale antecedent topography, whereas the effect of intermediate-scale and small-scale antecedent topography is overprinted by relative sea level changes.

In Section III, we successfully integrated field observations, drone-based photogrammetry, and digital outcrop analysis to gain new insight into the significant lateral variability of 3D geometries in the Upper San Andres mixed clastic-carbonate clinoforms of Last Chance Canyon, NM. We reconciled our outcrop observations and modeling results in a modification to the traditional reciprocal sedimentation model in the Permian Basin to explain the presence of mixed siliciclastic-carbonate clinoforms in the eastern part of LCC and coeval pure carbonate clinoforms in the western part of LCC. Unlike the lowstand siliciclastic and highstand carbonate dichotomy of the traditional reciprocal sedimentation model, our modification proposes uninterrupted sediment production of the carbonate factory in a "refugio" position, away from the avenues of sand input during fifth-order relative sea level lowstands. Our modeling results indicate a locally and temporally persistent, large-scale (~2 km wide) paleo-topographic low, the "Wilson Canyon Chute", in Last Chance Canyon that created mixed siliciclastic-carbonate clinoforms whereas coeval carbonates outside the chute entirely lack siliciclastic facies. During fifth-order relative sea level lowstands, the Wilson Canyon Chute most likely served as preferred avenue for basinward siliciclastic sediment bypass and deposition. Our 3D geometrical analysis, for the first time, revealed the significant along-strike variability in LCC clinoform geometries. Clinoform progradational extent was as great as 800 m, with up to ~300 m of progradational lateral

variability and up to 10 m in aggradational lateral variability. Slope angles were as great as 18˚ and varied up to 10˚ along strike within the individual clinoforms.

In Section IV, we introduced our new descriptive and observationally-driven shelf break rugosity analysis methodology that adds the missing third spatial and fourth temporal dimension to trajectory analysis. Our methodology presents an approach to quantify and visualize 4D along-strike variability in clinoform rollover trajectory analysis by providing the nomenclature and parameters that traditional trajectory analysis and the sequence stratigraphic method lack. We believe that the application of our methodology has the capability to improve the accuracy of sequence stratigraphic interpretations and reduce operator error from force-fitting data to pre-conceived / oversimplified depositional models. This study identified allogenic forcing from regional tectonics as main control on large-scale shelf geometries, and autogenic forcing from the carbonate factory growth as main control on intermediate-scale shelf break rugosity. Our analysis revealed a systematic shift in the large-scale average shelf break strike direction in the Oligo-Miocene interval of the Browse Basin over a transect of 10 km, which we attribute to far-field allogenic forcing from the Timor Trough collision zone. Furthermore, the ramp margin geometries in the Browse Basin are neither straight nor uniform through time. Shelf break rugosity and shelf break trajectory rugosity are not inherited parameters but are instead controlled by the intermediate-scale feedback between antecedent topography and carbonate system response. High-rugosity sections of the shelf break are smoothed by the autogenic carbonate system response in the Browse Basin by filling accommodation, resulting in a relatively constant rugosity of

~150 m. Visualizing 3D shelf breaks and shelf break trajectories in side view revealed that shelf break trajectories that plot in both sectors I (progradation and aggradation) and II (retrogradation and aggradation) correlate with phases of autogenic slope system re-organization and may be a proxy for morphological stability of the shelf break. Furthermore, map view and side view visualization of the shelf break trajectories highlighted intervals along the Browse Basin transect that are likely to yield inconsistent along-strike sea level reconstructions and sequence stratigraphic interpretations due to significant variability in stratal stacking patterns along strike.

REFERENCES

Adams, E. W., J. A. Kenter, K. Verwer, T. Playton, and P. Harris, 2013, So different, yet so similar: comparing and contrasting siliciclastic and carbonate slopes: Deposits, Architecture, and Controls of Carbonate Margin, Slope, and Basinal Settings: SEPM, Special Publication, v. 105, p. 14-25.

Adams, E. W., and W. Schlager, 2000, Basic types of submarine slope curvature: Journal of Sedimentary Research, v. 70, p. 814-828.

Ahr, W. M., 2011, Geology of carbonate reservoirs: the identification, description and characterization of hydrocarbon reservoirs in carbonate rocks, John Wiley & Sons.

Amour, F., M. Mutti, N. Christ, A. Immenhauser, G. S. Benson, S. M. Agar, S. Tomás, and L. Kabiri, 2013, Outcrop analog for an oolitic carbonate ramp reservoir: A scale-dependent geologic modeling approach based on stratigraphic hierarchy: AAPG bulletin, v. 97, p. 845-871.

Apthorpe, M., 1988, Cainozoic depositional history of the North West Shelf, *in* P. G. Purcell, and R. R. Purcell, eds., The Sedimentary Basins of Western Australia 2. Proceedings of the Petroleum Exploration Society of Australia Symposium: Perth, p. 55-84.

Baillie, P., C. M. Powell, Z. Li, and A. Ryall, 1994, The tectonic framework of Western Australia's Neoproterozoic to recent sedimentary basins, *in* P. G. Purcell, and R. R. Purcell, eds., The Sedimentary Basins of Western Australia, Proceedings of the Petroleum Exploration Society of Australia Symposium: Perth, p. 45-62.

Belde, J., S. Back, J. Bourget, and L. Reuning, 2017, Oligocene and Miocene carbonate platform development in the Browse Basin, Australian Northwest Shelf: Journal of Sedimentary Research, v. 87, p. 795-816.

Belopolsky, A. V., and A. W. Droxler, 2004, Seismic expressions of prograding carbonate bank margins: Middle Miocene, Maldives, Indian Ocean.

Bergman, K. L., H. Westphal, X. Janson, A. Poiriez, and G. P. Eberli, 2010, Controlling parameters on facies geometries of the Bahamas, an isolated carbonate platform environment, *in* W. H., R. B., and E. G.P., eds., Carbonate Depositional Systems: Assessing Dimensions and Controlling Parameters: Berlin, Springer, p. 5-80.

Bertram, G. T., and N. J. Milton, 1996, Seismic stratigraphy, *in* D. Emery, and K. Myers, eds., Sequence Stratigraphy: Oxford, UK, Blackwell Publishing Ltd., p. 43-60.

Betzler, C., J. Fürstenau, T. Lüdmann, C. Hübscher, S. Lindhorst, A. Paul, J. J. Reijmer, and A. W. Droxler, 2013, Sea-level and ocean-current control on carbonate-platform growth, Maldives, Indian Ocean: Basin Research, v. 25, p. 172-196.

Betzler, C., S. Lindhorst, G. P. Eberli, T. Lüdmann, J. Möbius, J. Ludwig, I. Schutter, M. Wunsch, J. J. Reijmer, and C. Hübscher, 2014, Periplatform drift: The combined result of contour current and off-bank transport along carbonate platforms: Geology, v. 42, p. 871-874.

Black, J. T., and R. A. Kohser, 2017, DeGarmo's materials and processes in manufacturing, John Wiley & Sons.

Blevin, J. E., Struckmeyer, H.I.M., Boreham, C.J., Cathro, D.L., Sayers, J., Totterdell, J.M., 1997, Browse Basin High Resolution Seismic Study - North West Shelf, Australia - Interpretation Report, Canberra, Australian Geological Survey Organisation, p. 282.

Bosence, D., 2005, A genetic classification of carbonate platforms based on their basinal and tectonic settings in the Cenozoic: Sedimentary Geology, v. 175, p. 49-72.

Boyd, D. W., 1958, Permian sedimentary facies, central Guadalupe Mountains, New Mexico, State Bureau of Mines and Mineral Resources, New Mexico Institute of Mining & Technology.

Burchette, T. P., 2012, Carbonate rocks and petroleum reservoirs: a geological perspective from the industry: Geological Society, London, Special Publications, v. 370, p. 17-37.

Cathro, D. L., and J. A. Austin, 2001, An early mid-Miocene, strike-parallel shelfal trough and possible karstification in the Northern Carnarvon Basin, northwest Australia: Marine Geology, v. 178, p. 157-169.

Cathro, D. L., J. A. Austin Jr, and G. D. Moss, 2003, Progradation along a deeply submerged OligoceneMiocene heterozoan carbonate shelf: How sensitive are clinoforms to sea level variations?: AAPG Bulletin, v. 87, p. 1547-1574.

Catuneanu, O., V. Abreu, J. P. Bhattacharya, M. D. Blum, R. W. Dalrymple, P. G. Eriksson, C. R. Fielding, W. L. Fisher, W. E. Galloway, M. R. Gibling, K. A. Giles, J. M. Holbrook, R. Jordan, C. G. S. C. Kendall, B. Macurda, O. J. Martinsen, A. D. Miall, J. E. Neal, D. Nummedal, L. Pomar, H. W. Posamentier,

B. R. Pratt, J. F. Sarg, K. W. Shanley, R. J. Steel, A. Strasser, M. E. Tucker, and C. Winker, 2009, Towards the standardization of sequence stratigraphy: Earth-Science Reviews, v. 92, p. 1-33.

Choquette, P. W., and P. O. Roehl, 1985, Carbonate petroleum reservoirs, Springer-Verlag.

Cresswell, G. R., 1991, The Leeuwin Current — observations and recent models: Journal of the Royal Society of Western Australia, v. 74, p. 1-14.

Dalrymple, R., 2010, Interpreting sedimentary successions: facies, facies analysis and facies models, *in* R. W. Dalrymple, and N. P. James, eds., Facies Models 4: St, John's, New Foundland, Geological Association of Canada, p. 3-18.

Darton, N., and J. Reeside Jr, 1926, Guadalupe group: Bulletin of the Geological Society of America, v. 37, p. 413-428.

Dutton, S. P., E. M. Kim, R. F. Broadhead, W. D. Raatz, C. L. Breton, S. C. Ruppel, and C. Kerans, 2005, Play analysis and leading-edge oil-reservoir development methods in the Permian basin: Increased recovery through advanced technologies: AAPG bulletin, v. 89, p. 553-576.

Feary, D. A., and N. P. James, 1995, Cenozoic biogenic mounds and buried Miocene (?) barrier-reef on a predominantly cool-water carbonate continental-margin Eucla Basin, Western Great-Australian-Bight: Geology, v. 23, p. 427-430.

Fischer, A. G., and M. Sarnthein, 1988, Airborne silts and dune-derived sands in the Permian of the Delaware Basin: Journal of Sedimentary Petrology, v. 58.

Galloway, W., T. Ewing, C. Garrett, N. Tyler, and D. Bebout, 1983, Atlas of major Texas oil reservoirs.

Gardner, M. H., 1992, Sequence stratigraphy of eolian-derived turbidites: deep water sedimentation patterns along an arid carbonate platform and their impact on hydrocarbon recovery in Delaware Mountain Group reservoirs, West Texas, *in* D. H. Mruk, Curran, B. C. , ed., Permian Basin Exploration and Production Strategies: Applications of Sequence Stratigraphic and Reservoir Characterization Concepts: West Texas Geological Society, Publication, v. 92-91, p. 7-11.

Gill, J. R., and W. A. Cobban, 1973, Stratigraphy and geologic history of the Montana Group and equivalent rocks, Montana, Wyoming, and North and South Dakota.

Gischler, E., and A. J. Lomando, 2000, Isolated carbonate platforms of Belize, Central America: sedimentary facies, late Quaternary history and controlling factors: Geological Society, London, Special Publications, v. 178, p. 135-146.

Golonka, J., M. Ross, and C. Scotese, 1994, Phanerozoic paleogeographic and paleoclimatic modeling maps.

Gómez-Pérez, I., P. A. Fernández-Mendiola, and J. García-Mondéjar, 1998, Constructional dynamics for a Lower Cretaceous carbonate ramp (Gorbea Massif, north Iberia), *in* V. P. Wright, and T. P. Burchette, eds., Carbonate Ramps, v. 149: London, Geological Society, London, Special Publications, p. 229-252.

Gradstein, F. M., J. G. Ogg, M. Schmitz, and G. Ogg, 2012, The geologic time scale 2012, Elsevier, 1176 p.

Hall, R., 2011, Australia–SE Asia collision: plate tectonics and crustal flow: Geological Society, London, Special Publications, v. 355, p. 75-109.

Haq, B. U., J. Hardenbol, and P. R. Vail, 1987, Chronology of fluctuating sea levels since the Triassic: Science, v. 235, p. 1156-1167.

Harms, J. C., and C. R. Williamson, 1988, Deep-water density current deposits of Delaware Mountain Group (Permian), Delaware Basin, Texas and New Mexico: AAPG Bulletin, v. 72, p. 299-317.

Harper, B. B., Á. Puga-Bernabéu, A. W. Droxler, J. M. Webster, E. Gischler, M. Tiwari, T. Lado-Insua, A. L. Thomas, S. Morgan, and L. Jovane, 2015, Mixed carbonate–siliciclastic sedimentation along the great barrier reef upper slope: A challenge to the reciprocal sedimentation model: Journal of Sedimentary Research, v. 85, p. 1019-1036.

Harrison, S. C., 1966, Depositional mechanics of the Permian Cherry Canyon Sandstone Tongue, Last Chance Canyon, New Mexico, Texas Tech University.

Hart, B. S., 2013, Whither seismic stratigraphy?: Interpretation, v. 1, p. SA3-SA20.

Hayes, P. T., 1959, San Andres limestone and related Permian rocks in Last Chance Canyon and vicinity, southeastern New Mexico: AAPG Bulletin, v. 43, p. 2197-2213.

He, Y., C. Kerans, H. Zeng, X. Janson, and S. Z. Scott, 2016, Reservoir-scale chronostratigraphic significance of seismic reflections of a strongly prograding

shelf margin: 3D outcrop-constrained seismic models, SEG Technical Program Expanded Abstracts 2016, Society of Exploration Geophysicists, p. 1818-1823.

Helland-Hansen, W., and G. J. Hampson, 2009, Trajectory analysis: concepts and applications: Basin Research, v. 21, p. 454-483.

Henriksen, S., G. J. Hampson, W. Helland-Hansen, E. P. Johannessen, and R. J. Steel, 2009, Shelf edge and shoreline trajectories, a dynamic approach to stratigraphic analysis: Basin Research, v. 21, p. 445-453.

Henriksen, S., W. Helland-Hansen, and S. Bullimore, 2011, Relationships between shelf-edge trajectories and sediment dispersal along depositional dip and strike: a different approach to sequence stratigraphy: Basin Research, v. 23, p. 3-21.

Hine, A. C., and H. T. Mullins, 1983, Modern carbonate shelf-slope breaks: SEPM Special Publications, v. 33, p. 169-183.

Hodgetts, D., 2013, Laser scanning and digital outcrop geology in the petroleum industry: a review: Marine and Petroleum Geology, v. 46, p. 335-354.

Jacka, A., R. Beck, L. St Germain, and S. Harrison, 1968, Permian deep-sea fans of the Delaware Mountain Group (Guadalupian), Delaware basin: Guadalupian Facies, Apache Mountain Area, West Exas: Permian Basin Sec., Soc. Econ. Paleontologists and Mineralogists, p. 49-90.

James, N. P., and Y. Bone, 2010, Neritic Carbonate Sediments in a Temperate Realm: Southern Australia, Springer Science & Business Media, 254 p.

Jervey, M. T., 1988, Quantitative geological modeling of siliciclastic rock sequences and their seismic expression, *in* C. K. Wilgus, B. S. Hasting, C. G. S. C. Kendall, H.

W. Posamentier, C. A. Ross, and J. Van Wagoner, eds., Sea-Level Changes—An Integrated Approach: SEPM Special Publication 42, p. 47-69.

Johannessen, E. P., and R. J. Steel, 2005, Shelf-margin clinoforms and prediction of deepwater sands: Basin Research, v. 17, p. 521-534.

Kendall, C.G.St.C., and W. Schlager, 1981, Carbonates and relative changes in sea level: Marine Geology, v. 44, p. 181-212.

Kennard, J., I. Deighton, D. Ryan, D. Edwards, and C. Boreham, 2003, Subsidence and thermal history modelling: new insights into hydrocarbon expulsion from multiple petroleum systems in the Browse Basin: Timor Sea Petroleum Geoscience. Proceedings of the Timor Sea Symposium, Darwin, p. 19-20.

Kenter, J., G. Bracco Gartner, and W. Schlager, 2001, Seismic models of a mixed carbonate-siliciclastic shelf margin: Permian upper San Andres Formation, Last Chance Canyon, New Mexico: Geophysics, v. 66, p. 1744-1748.

Kenter, J. A., 1990, Carbonate platform flanks: slope angle and sediment fabric: Sedimentology, v. 37, p. 777-794.

Kenter, J. A., F. Podladchikov, M. Reinders, S. J. Van der Gaast, B. W. Fouke, and M. D. Sonnenfeld, 1997, Parameters controlling sonic velocities in a mixed carbonate-siliciclastics Permian shelf-margin (upper San Andres formation, Last Chance Canyon, New Mexico): Geophysics, v. 62, p. 505-520.

Kerans, C., and W. M. Fitchen, 1995, Sequence hierarchy and facies architecture of a carbonate-ramp system: San Andres Formation of Algerita Escarpment and western Guadalupe Mountains, west Texas and New Mexico: University of

Texas, Bureau of Economic Geology, Report of Investigations, v. 235: Austin, Bureau of Economic Geology, University of Texas at Austin, 86 p.

Kerans, C., and K. Kempter, 2002, Hierarchical stratigraphic analysis of a carbonate platform, Permian of the Guadalupe Mountains, Tulsa, OK, AAPG Datapages. Discovery Series 5, CD-ROM and color plate.

Kerans, C., F. J. Lucia, and R. Senger, 1994, Integrated characterization of carbonate ramp reservoirs using Permian San Andres Formation outcrop analogs: AAPG bulletin, v. 78, p. 181-216.

Kerans, C., and S. W. Tinker, 1997, Sequence stratigraphy and characterization of carbonate reservoirs, v. 40, SEPM.

King, P. B., 1942, Permian of West Texas and Southeastern New Mexico: PART 1: AAPG Bulletin, v. 26, p. 535-763b.

Kocurek, G., and B. L. Kirkland, 1998, Getting to the source: aeolian influx to the Permian Delaware basin region: Sedimentary Geology, v. 117, p. 143-149.

Lee, H. J., J. Locat, P. Desgagnés, J. D. Parsons, B. G. McAdoo, D. L. Orange, P. Puig, F. L. Wong, P. Dartnell, and E. Boulanger, 2007, Submarine mass movements on continental margins, *in* C. A. Nittrouer, J. A. Austin, M. E. Field, J. H. Kravitz, J. P. M. Syvitski, and P. L. Wiberg, eds., Continental Margin Sedimentation: From Sediment Transport to Sequence Stratigraphy: Oxford, UK, Blackwell Publishing Ltd., p. 213-273.

Madof, A. S., A. D. Harris, and S. D. Connell, 2016, Nearshore along-strike variability: Is the concept of the systems tract unhinged?: Geology, v. 44, p. 315-318.

Mandelbrot, B. B., 1983, The fractal geometry of nature, v. 173, WH freeman New York.

Martinsen, O. J., and W. Helland-Hansen, 1995, Strike variability of clastic depositional systems: Does it matter for sequence-stratigraphic analysis?: Geology, v. 23, p. 439-442.

McCormick, D. S., J. B. Thurmond, J. P. Grotzinger, and R. J. Fleming, 2000, Creating a Three-Dimensional Model of Clinoforms in the Upper San Andreas Formation, Last Chance Canyon, New Mexico: American Association of Petroleum Geologists, Bulletin, v. 84.

McDermott, R. W., 1983, Depositional processes and environments of the Permian sandstone tongue of the Cherry Canyon Formation and the Upper San Andres Formation, Last Chance Canyon, Southeastern New Mexico, University of Texas at Austin.

McGowran, B., G. R. Holdgate, Q. Li, and S. J. Gallagher, 2004, Cenozoic stratigraphic succession in southeastern Australia: Australian Journal of Earth Sciences, v. 51, p. 459-496.

McKnight, C. L., 1983, Structural Evolution of the Guadalupe Mountains, South-Central New-Mexico and West Texas: AAPG Bulletin, v. 67, p. 511-511.

McKnight, C. L., 1986, Descriptive geomorphology of the Guadalupe Mountains, south-central New Mexico and west Texas, Department of Geology, Baylor University.

Meissner, F. F., 1972, Cyclic sedimentation in Middle Permian strata of the Permian basin, west Texas and New Mexico: Cyclic sedimentation in the Permian Basin, p. 203-232.

Mellere, D., P. Plink-Björklund, and R. Steel, 2002, Anatomy of shelf deltas at the edge of a prograding Eocene shelf margin, Spitsbergen: Sedimentology, v. 49, p. 1181-1206.

Miller, K. G., M. A. Kominz, J. V. Browning, J. D. Wright, G. S. Mountain, M. E. Katz, P. J. Sugarman, B. S. Cramer, N. Christie-Blick, and S. F. Pekar, 2005, The phanerozoic record of global sea-level change: Science, v. 310, p. 1293-1298.

Mitchum, R., P. Vail, and J. Sangree, 1977a, Seismic stratigraphy and global changes of sea level: Part 6. Stratigraphic interpretation of seismic reflection patterns in depositional sequences: Section 2. Application of seismic reflection configuration to stratigraphic interpretation, *in* C. E. Payton, ed., AAPG Memoir 26: Seismic Stratigraphy--Applications to Hydrocarbon Exploration, p. 117-133.

Mitchum, R., P. Vail, and S. Thompson III, 1977b, Seismic stratigraphy and global changes of sea level: Part 2. The depositional sequence as a basic unit for stratigraphic analysis: Section 2. Application of seismic reflection configuration to stratigraphic interpretation.

Mitchum, R. M., and J. C. Van Wagoner, 1991, High-frequency sequences and their stacking patterns: sequence-stratigraphic evidence of high-frequency eustatic cycles: Sedimentary Geology, v. 70, p. 131-160.

Naiman, E. R., 1982, Sedimentation and diagenesis of a shallow marine carbonate and siliciclastic shelf sequence: the Permian (Guadalupian) Grayburg Formation, southeastern New Mexico, University of Texas at Austin.

Neal, J. E., V. Abreu, K. M. Bohacs, H. R. Feldman, and K. H. Pederson, 2016, Accommodation succession (δA/δS) sequence stratigraphy: observational method, utility and insights into sequence boundary formation: Journal of the Geological Society, v. 173, p. 803-816.

Phelps, R. M., and C. Kerans, 2007, Architectural characterization and three-dimensional modeling of a carbonate channel–levee complex: Permian San Andres Formation, Last Chance Canyon, New Mexico, USA: Journal of Sedimentary Research, v. 77, p. 939-964.

Phelps, R. M., C. Kerans, S. Z. Scott, X. Janson, and J. A. Bellian, 2008, Three-dimensional modelling and sequence stratigraphy of a carbonate ramp-to-shelf transition, Permian Upper San Andres Formation: Sedimentology, v. 55, p. 1777-1813.

Pike, R., I. Evans, and T. Hengl, 2009, Geomorphometry: a brief guide: Developments in Soil Science, v. 33, p. 3-30.

Pike, R. J., 2000, Geomorphometry-diversity in quantitative surface analysis: Progress in Physical Geography, v. 24, p. 1-20.

Plotnick, R. E., R. H. Gardner, W. W. Hargrove, K. Prestegaard, and M. Perlmutter, 1996, Lacunarity analysis: a general technique for the analysis of spatial patterns: Physical review E, v. 53, p. 5461.

Pomar, L., 2001, Types of carbonate platforms: a genetic approach: Basin Research, v. 13, p. 313-334.

Pomar, L., A. Obrador, and H. Westphal, 2002, Sub-wavebase cross-bedded grainstones on a distally steepened carbonate ramp, Upper Miocene, Menorca, Spain: Sedimentology, v. 49, p. 139-169.

Posamentier, H., R. Davies, J. Cartwright, and L. Wood, 2007, Seismic geomorphology-an overview: Geological Society, London, Special Publications, v. 277, p. 1-14.

Puga-Bernabéu, Á., J. M. Webster, R. J. Beaman, and V. Guilbaud, 2013, Variation in canyon morphology on the Great Barrier Reef margin, north-eastern Australia: the influence of slope and barrier reefs: Geomorphology, v. 191, p. 35-50.

Rankey, E. C., 2003, Carbonate-filled channel complexes on carbonate ramps: an example from the Peerless Park Member [Keokuk Limestone, Visean, Lower Carboniferous (Mississippian)], St. Louis, MO, USA: Sedimentary Geology, v. 155, p. 45-61.

Rarity, F., X. Van Lanen, D. Hodgetts, R. Gawthorpe, P. Wilson, I. Fabuel-Perez, and J. Redfern, 2014, LiDAR-based digital outcrops for sedimentological analysis: workflows and techniques: Geological Society, London, Special Publications, v. 387, p. 153-183.

Read, J. F., 1985, Carbonate platform facies models: AAPG Bulletin, v. 69, p. 1-21.

Reuning, L., S. Back, H. Schulz, M. Hirsch, P. Kukla, and J. Grötsch, 2009, Seismic expression of sedimentary processes on a carbonate shelf and slope system,

Browse Basin, Australia – part I – non-tropical carbonates, Eocene to Lower Miocene. Extended Abstract, 71st EAGE Conference & Exhibition.

Rosleff-Soerensen, B., L. Reuning, S. Back, and P. Kukla, 2012, Seismic geomorphology and growth architecture of a Miocene barrier reef, Browse Basin, NW-Australia: Marine and Petroleum Geology, v. 29, p. 233-254.

Rosleff-Soerensen, B., L. Reuning, S. Back, and P. A. Kukla, 2016, The response of a basin-scale Miocene barrier reef system to long-term, strong subsidence on a passive continental margin, Barcoo Sub-basin, Australian North West Shelf: Basin Research, v. 28, p. 103-123.

Ross, C. A., 1983, Late Paleozoic foraminifera as depth indicators: AAPG Bulletin, v. 67, p. 542-543.

Sanchez, C. M., C. S. Fulthorpe, and R. J. Steel, 2012, Miocene shelf-edge deltas and their impact on deepwater slope progradation and morphology, Northwest Shelf of Australia: Basin Research, v. 24, p. 683-698.

Sarg, J., 1988, Carbonate sequence stratigraphy, *in* C. K. Wilgus, B. S. Hastings, H. M. Posamentier, J. Van Wagoner, C. A. Ross, and G. C. S. C. Kendall, eds., Sea-Level Changes—An Integrated Approach: SEPM Special Publication 42, p. 155-181.

Sarg, J., and P. Lehmann, 1986a, Facies and stratigraphy of lower-upper San Andres shelf-crest and outer shelf and lower Grayburg inner shelf: Lower and Middle Guadalupian Facies, stratigraphy, and reservoir geometries, San

Andres/Grayburg Formations, Guadalupian Mountains, New Mexico and Texas: SEPM Permian Basin Section Publ, v. 86, p. 9-35.

Sarg, J., and P. Lehmann, 1986b, Lower-Middle Guadalupian facies and stratigraphy, San Andres/Grayburg Formations, Permian Basin, Guadalupe Mountains, New Mexico, *in* G. E. Moore, Wilde, G. L. , ed., Lower and Middle Guadalupian Facies, Stratigraphy, and Reservoir Geometries, San Andres/Grayburg Formations, Guadalupe Mountains, New Mexico and Texas: Permian Basin Section/Society of Economic Paleontologists and Mineralogists Publication 86-25: Tulsa, OK, p. 1-8.

Sarg, J., J. Markello, and L. Weber, 1999, The second-order cycle, carbonate-platform growth, and reservoir, source, and trap prediction, *in* P. M. Harris, J. A. Simo, and A. H. Saller, eds., Advances in Carbonate Sequence Stratigraphy: Application to

Reservoirs, Outcrops, and Models. SEPM Special Publication 62, p. 1-24.

Sarg, R., J. Markello, R. Bloch, and B. Clarke, 1997, Stratigraphic architecture of the transgressive and turnaround phases, Guadalupian Supersequence: Cherry Canyon and San Andres Formations, Brokeoff and Guadalupe Mountains, New Mexico, American Association of Petroleum Geologists, Annual Meeting: Future Legends, Field Trip Guidebook #16, p. 213.

Savin, S. M., L. Abel, E. Barrera, D. Hodell, J. P. Kennett, M. Murphy, G. Keller, J. Killingley, and E. Vincent, 1985, The evolution of Miocene surface and near-

surface marine temperatures: oxygen isotopic evidence, *in* J. P. Kennet, ed., The Miocene Ocean: Paleoceanography and Biogeography, v. 163, p. 49-82.

Schlager, W., 2000, Sedimentation rates and growth potential of tropical, cool-water and mud-mound carbonate systems, *in* E. Insalaco, W. P. Skelton, and P. T.J., eds., Carbonate Platform Systems: Components and Interactions, v. 178: London, UK, Geological Society Special Publications, p. 217-227.

Schlager, W., 2005, Carbonate sedimentology and sequence stratigraphy: SEPM concepts in sedimentology and paleontology: Tulsa, Okla., SEPM, vii, 200 p. p.

Schlager, W., and E. W. Adams, 2001, Model for the sigmoidal curvature of submarine slopes: Geology, v. 29, p. 883-886.

Scott, S. Z., 2007, Sequence stratigraphic and architectural characterization of a Permian carbonate ramp, upper San Andres Formation, Last Chance Canyon, New Mexico. Unpublished M.S. Thesis, The University of Texas at Austin, 125 p.

Skinner, J. W., 1946, Correlation of Permian of west Texas and southeast New Mexico: AAPG Bulletin, v. 30, p. 1857-1874.

Slingerland, R., and N. D. Smith, 2004, River avulsions and their deposits: Annu. Rev. Earth Planet. Sci., v. 32, p. 257-285.

Sonnenfeld, M., 1991a, High-frequency cyclicity within shelf-margin and slope strata of the upper San Andres sequence, Last Chance Canyon, *in* S. Meader-Roberts, Candelaria, M. P., Moore G. E., ed., Sequence Stratigraphy, Facies and Reservoir Geometries of the San Andres, Grayburg, and Queen Formations, Guadalupe Mountains, New Mexico and Texas: SEPM, Permian Basin Section, Society of

Economic Paleontologists and Mineralogists Publication Special Publication, v. 91-32, p. 11-51.

Sonnenfeld, M., 1993, Anatomy of offlap: Upper San Andres Formation (Permian, Guadalupian), Last Chance Canyon, Guadalupe Mountains, New Mexico: New Mexico Geology Society Guidebook, 44th Field Conference, Carlsbad Region, New Mexico and West Texas, p. 195-203.

Sonnenfeld, M. D., 1991b, Anatomy of Offlap in a Shel-margin Depositional Sequence: Upper San Andres Formation (Permian, Guadalupian), Last Chance Canyon, Guadalupe Mountains, New Mexico, Colorado School of Mines, Golden, CO, 297 p.

Sonnenfeld, M. D., and T. A. Cross, 1993, Volumetric partitioning and facies differentiation within the Permian Upper San Andres formation of Last Chance Canyon, Guadalupe Mountains, New Mexico: Chapter 17, Carbonate Sequence Stratigraphy, v. 57, AAPG Memoir, p. 435-474.

Stafleu, J., and M. D. Sonnenfeld, 1994, Seismic models of a shelf-margin depositional sequence: upper San Andres formation, Last Chance Canyon, New Mexico: Journal of Sedimentary Research, v. 64, p. 481-499.

Steckler, M., D. Reynolds, B. Coakley, B. Swift, and R. Jarrard, 1993, Modelling passive margin sequence stratigraphy, *in* H. Posamentier, C. Summerhayes, and B. A. Haq, G., eds., Sequence stratigraphy and Facies Associations, v. 18, Special Publication of the International Association of Sedimentologists, p. 19-41.

Steel, R., and T. Olsen, 2002, Clinoforms, clinoform trajectories and deepwater sands: Sequence-stratigraphic models for exploration and production: Evolving methodology, emerging models and application histories: Gulf Coast Section SEPM 22nd Research Conference, Houston, Texas, p. 367-381.

Stephenson, A. E., and S. J. Cadman, 1994, Browse Basin, Northwest Australia - the evolution, paleogeography and petroleum potential of a passive continental-margin: Palaeogeography Palaeoclimatology Palaeoecology, v. 111, p. 337-366.

Struckmeyer, H. I., J. E. Blevin, J. Sayers, J. M. Totterdell, K. Baxter, and D. L. Cathro, 1998, Structural evolution of the Browse Basin, North West Shelf: new concepts from deep-seismic data: The Sedimentary Basins of Western Australia 2: Proceedings of the Petroleum Exploration Society of Australia Symposium, Perth, p. 345-367.

Tesch, P., R. Reece, M. Pope, and J. Markello, 2018, Quantification of architectural variability and controls in an Upper Oligocene to Lower Miocene carbonate ramp, Browse Basin, Australia: Marine and Petroleum Geology, v. 91, p. 432-454.

Tripati, A. K., C. D. Roberts, and R. A. Eagle, 2009, Coupling of CO2 and ice sheet stability over major climate transitions of the last 20 million years: Science, v. 326, p. 1394-1397.

Vail, P., R. Mitchum Jr, and S. Thompson III, 1977, Seismic stratigraphy and global changes of sea level; Part 4, Global cycles of relative changes of sea level, *in* C.

E. Payton, ed., Seismic Stratigraphy; applications to hydrocarbon exploration: American Association of Petroleum Geologists Memoir 26, p. 83-97.

Van Siclen, D., and D. Merriam, 1964, Depositional topography in relation to cyclic sedimentation: Symposium on Cyclic Sedimentation: Kansas Geological Survey, Bulletin, p. 533-539.

Van Siclen, D. C., 1958, Depositional topography--examples and theory: AAPG Bulletin, v. 42, p. 1897-1913.

Van Wagoner, J., 1988, An overview of the fundamentals of sequence stratigraphy and key definitions, *in* C. K. Wilgus, B. S. Hastings, C. G. S. C. Kendall, H. W. Posamentier, C. A. Ross, and J. C. Van Wagoner, eds., Sea Level Changes—An Integrated Approach, SEPM Special Publication, v. 42, p. 39-45.

Veritas, 2000, 1999 Brecknock South 3D Marine Seismic Survey, Seismic data processing report, Veritas DCG Asia Pacific Ltd., p. 198.

Wehr, F., 1994, Effects of variations in subsidence and sediment supply on parasequence stacking patterns: Siliciclastic sequence stratigraphy, v. 58, p. 369-379.

Western Geophysical, 1999, Final operations report, Brecknock South 3D survey, North West Shelf, Western Australia, p. 129.

Williams, K., 1969, Principles of cementation, environmental framework and diagenesis of the Grayburg and Queen formations, New Mexico and Texas: unpublished Ph. D. Dissertation, Texas Tech University.

Willis, I., 1988, Results of exploration, Browse Basin, North West Shelf, Western Australia: North West Shelf Symposium, Perth, W.A., p. 253-257.

Wilson, J. L., 1975, Carbonate Facies in Geologic History: New York, Springer Verlag, 471 p.

Wiseman, J. D., and C. D. Ovey, 1953, Definitions of features on the deep-sea floor: Deep Sea Research (1953), v. 1, p. 11-16.

Woodside, 1980, Brecknock No. 1 well completion report (WA-33-P), Woodside Petroleum Develpment Pty. Ltd., p. 302.

Woodside Energy, 2007, Calliance-1 well completion report, interpretive data (WA-28-R, Browse Basin), Woodisde Energy Ltd., p. 822.

Woodside Energy, 2008, Calliance-2 well completion report, interpretive data (WA-28-R, Browse Basin), Woodside Energy Ltd., p. 667.

Woodside Energy, 2009, Calliance-3 well completion report, basic data (WA-28-R, Browse Basin), Woodside Energy Ltd., p. 1249.

Wyrwoll, K., B. Greenstein, G. Kendrick, and G. Chen, 2009, The paleoceanography of the Leeuwin Current: implications for a future world: Journal of the Royal Society of Western Australia, v. 92, p. 37-51.

Yeates, A., M. Bradshaw, J. Dickins, A. Brakel, N. Exon, R. Langford, S. Mulholland, J. Totterdell, and M. Yeung, 1987, The Westralian Superbasin: an Australian link with Tethys: Shallow Tethys 2: 2nd International Symposium on Shallow Tethys, p. 199-213.

Zachos, J. C., G. R. Dickens, and R. E. Zeebe, 2008, An early Cenozoic perspective on greenhouse warming and carbon-cycle dynamics: Nature, v. 451, p. 279-283.

APPENDIX A

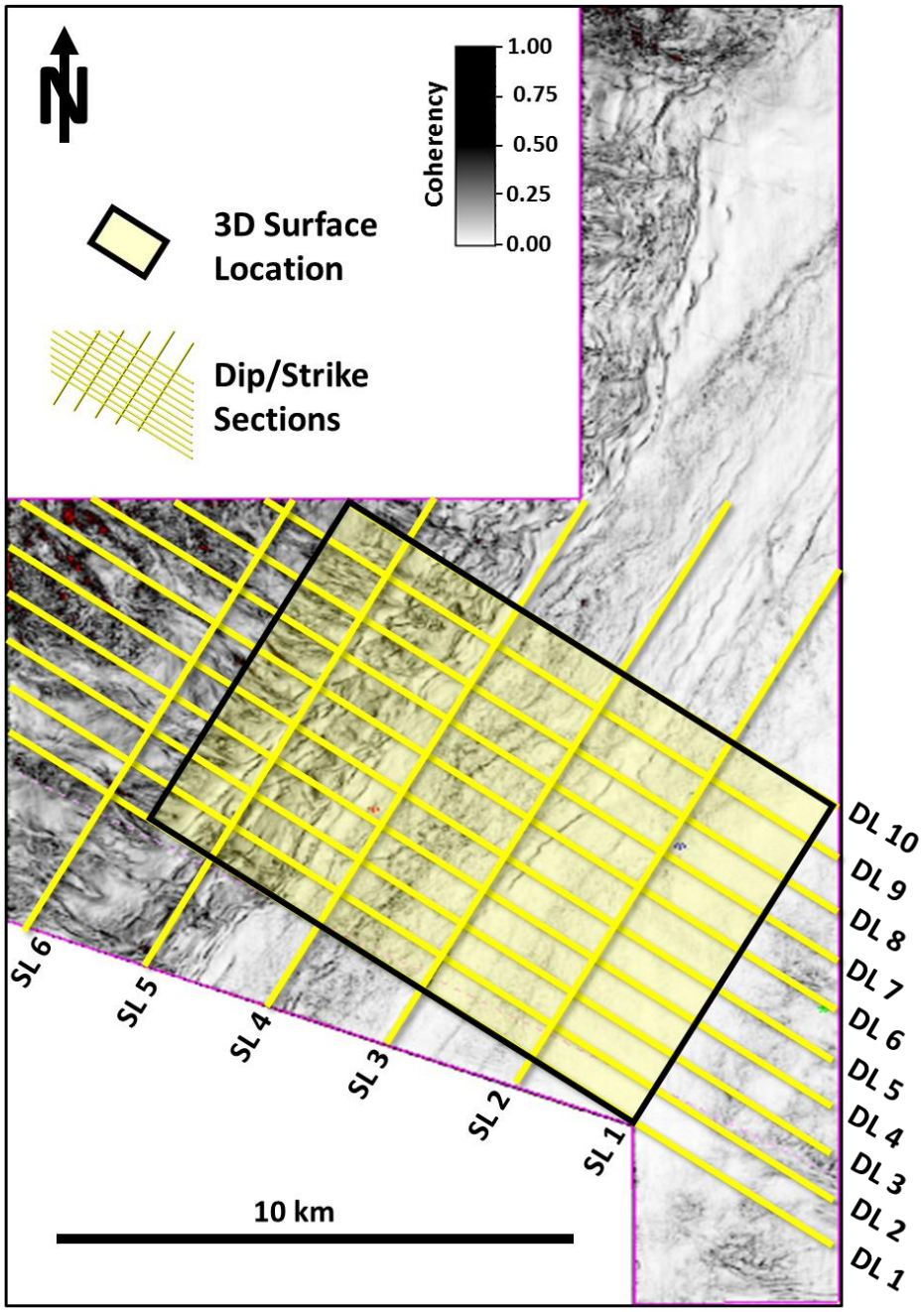

Figure AII.1: Location of the ten dip directional cross sections DL1-10 and the six strike directional cross sections SL1-6 as yellow lines and the map view area of seismic surfaces (black rectangle) on a coherency slice through the depth-converted seismic data at 2200 m.

Table AII.1: Slope angle table.

					Slope Angle [°]						
Seq #	**DL1**	**DL2**	**DL3**	**DL4**	**DL5**	**DL6**	**DL7**	**DL8**	**DL9**	**DL10**	**AVG**
3	6	6	6	6	5	7	6	7	8	7	**6**
4	6	7	8	7	6	7	8	8	8	8	**7**
5	9	9	9	9	10	9	10	10	9	10	**9**
6	12	11	11	10	10	9	10	10	9	10	**10**
7	8	9	9	9	8	8	9	9	8	9	**9**
8	11	9	8	8	8	8	8	8	7	8	**8**
9	8	8	8	7	8	8	8	8	8	8	**8**
10	11	12	11	10	10	10	9	10	9	9	**10**
11	9	10	10	10	9	10	9	10	9	9	**9**
12	7	8	7	8	8	6	8	8	7	8	**7**

Table AII.2: Progradation table.

					Progradation [m]						
Seq #	**DL1**	**DL2**	**DL3**	**DL4**	**DL5**	**DL6**	**DL7**	**DL8**	**DL9**	**DL10**	**AVG**
3	0	0	0	0	0	0	0	0	0	0	0
4	410	1590	1375	1275	2380	1030	1220	740	910	870	**1180**
5	2400	1360	1900	1760	1590	1970	2015	1800	1825	1470	**1809**
6	730	560	730	1110	1040	520	190	560	475	300	**622**
7	190	410	1300	1020	530	840	1230	510	630	1490	**815**
8	1600	1425	120	520	610	1235	610	580	730	410	**784**
9	275	650	100	930	830	125	860	950	1050	500	**627**
10	1750	1080	2100	1330	1690	1170	1490	1010	870	1220	**1371**
11	-190	100	75	150	330	630	80	460	70	280	**199**
12	1650	1600	1000	1090	1470	1660	1615	1850	2100	1525	**1556**

Table AII.3: Aggradation table

					Aggradation [m]						
Seq #	**DL1**	**DL2**	**DL3**	**DL4**	**DL5**	**DL6**	**DL7**	**DL8**	**DL9**	**DL10**	**AVG**
4	75	15	14	25	-25	50	25	50	25	35	**29**
5	-40	40	-10	-5	20	-30	-35	-35	-30	10	**-12**
6	85	90	75	45	50	70	100	75	75	70	**74**
7	70	50	5	0	30	10	-15	40	50	-15	**23**
8	-50	-30	80	70	30	-20	45	35	15	45	**22**
9	80	55	80	35	45	90	20	25	25	75	**53**
10	20	80	5	35	15	35	30	70	75	30	**40**
11	100	55	75	65	50	25	70	50	70	45	**61**
12	35	30	45	55	50	20	30	10	-15	35	**30**

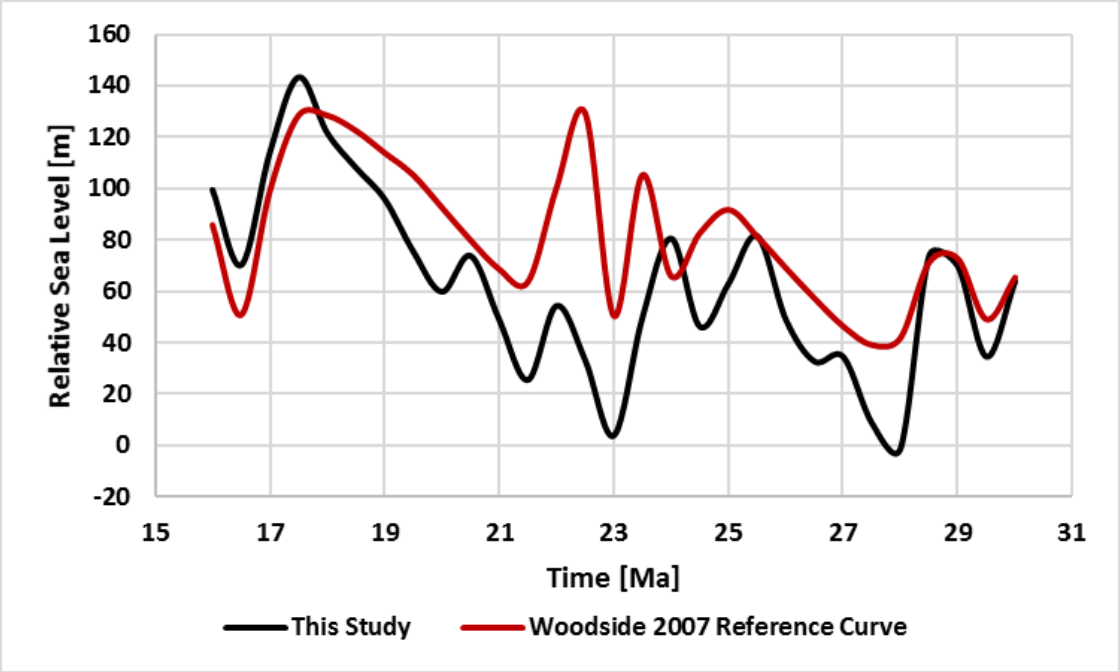

Figure AII.2: Seismically-derived relative sea level curve from this study compared to the reference curve from Woodside Energy (2007). The correlation coefficient between the two curves is 0.81.

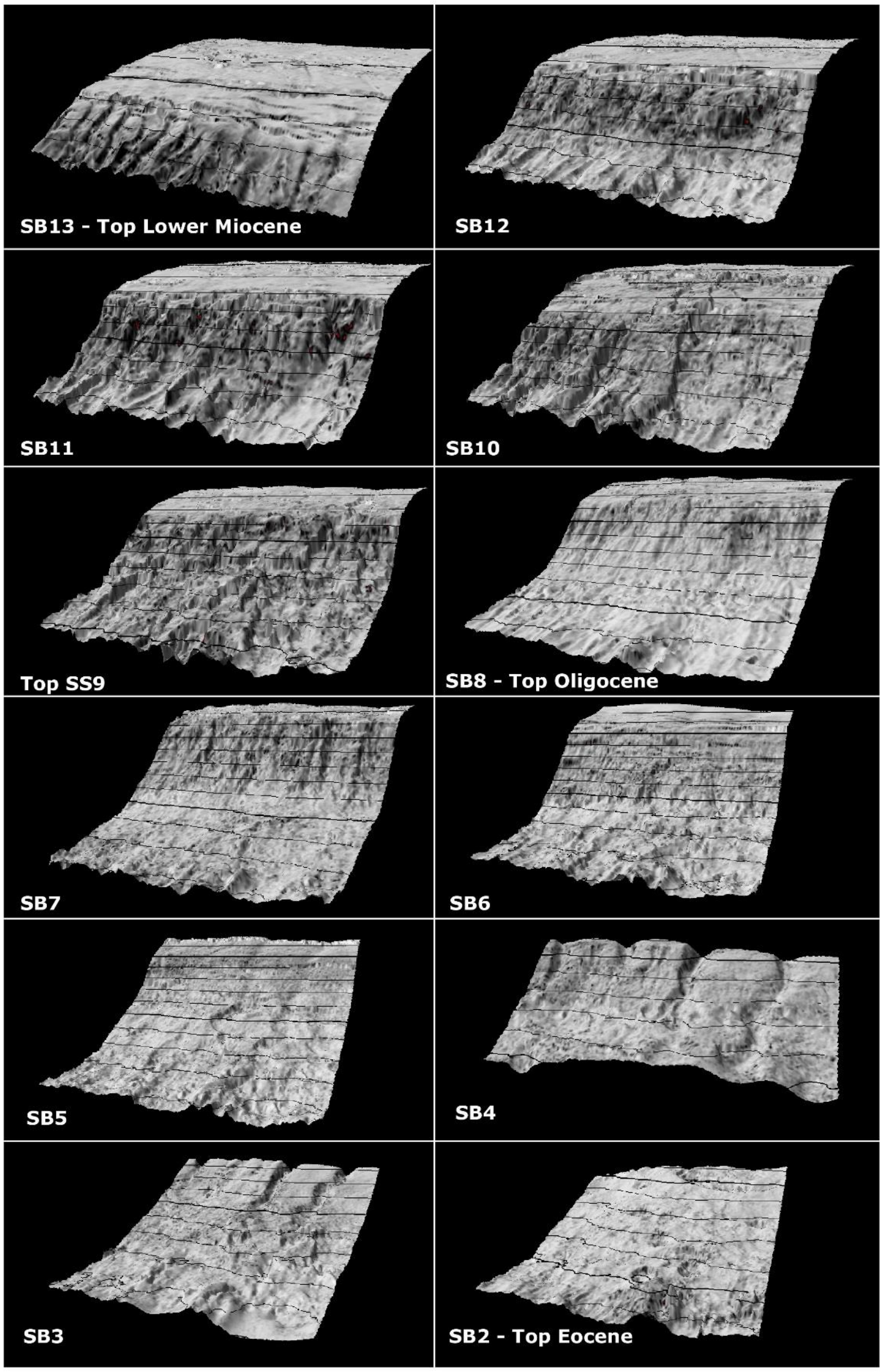

Figure AII.3: Coherency attribute on horizon slices of sequence boundaries SB1-12 visualizing the geomorphological evolution of the ramp system from the Top Eocene (SB1) to Top Lower Miocene (SB12). The slope system switches from few channels during seismic sequences SS1-5 to many channels from seismic sequences SS6-12. Contour interval for SB8-

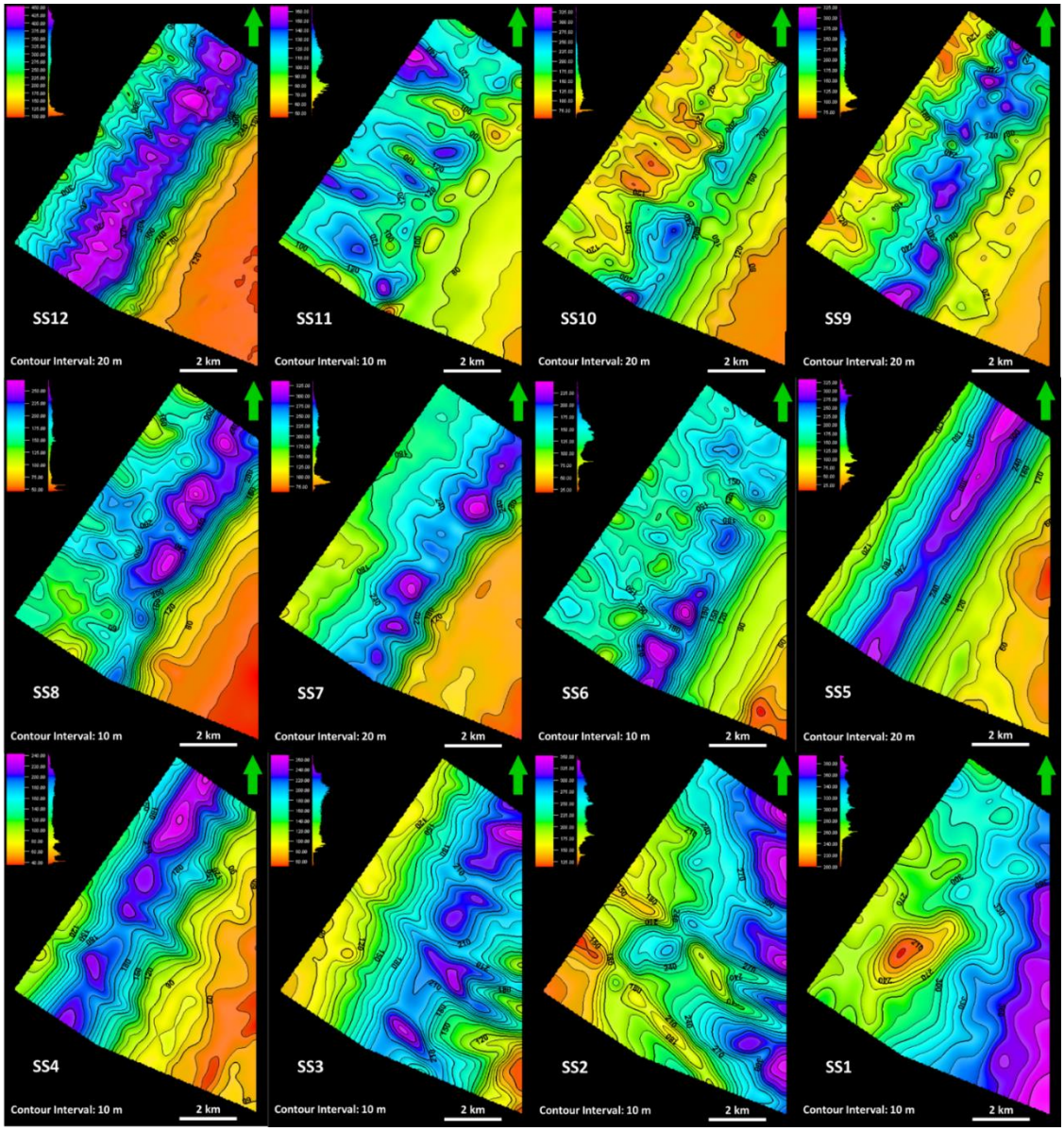

Figure AII.4: Isopach maps of seismic sequences SS1-12. Maximum thickness of deposits (magenta) is oriented north-south for the Eocene and Lower Oligocene deposits in SS1 and 2. Dominant orientation of maximum thickness for the Oligocene through Lower Miocene deposits is southwest-northeast, along the slope. Slope channels are identified as sub-linear features, cutting through the thick slope deposits from the landward shelf edge in the southeast to the basin in the northwest are identified as sub-linear features, cutting through the thick slope deposits from the landward shelf edge in the southeast to the basin in the northwest

APPENDIX B

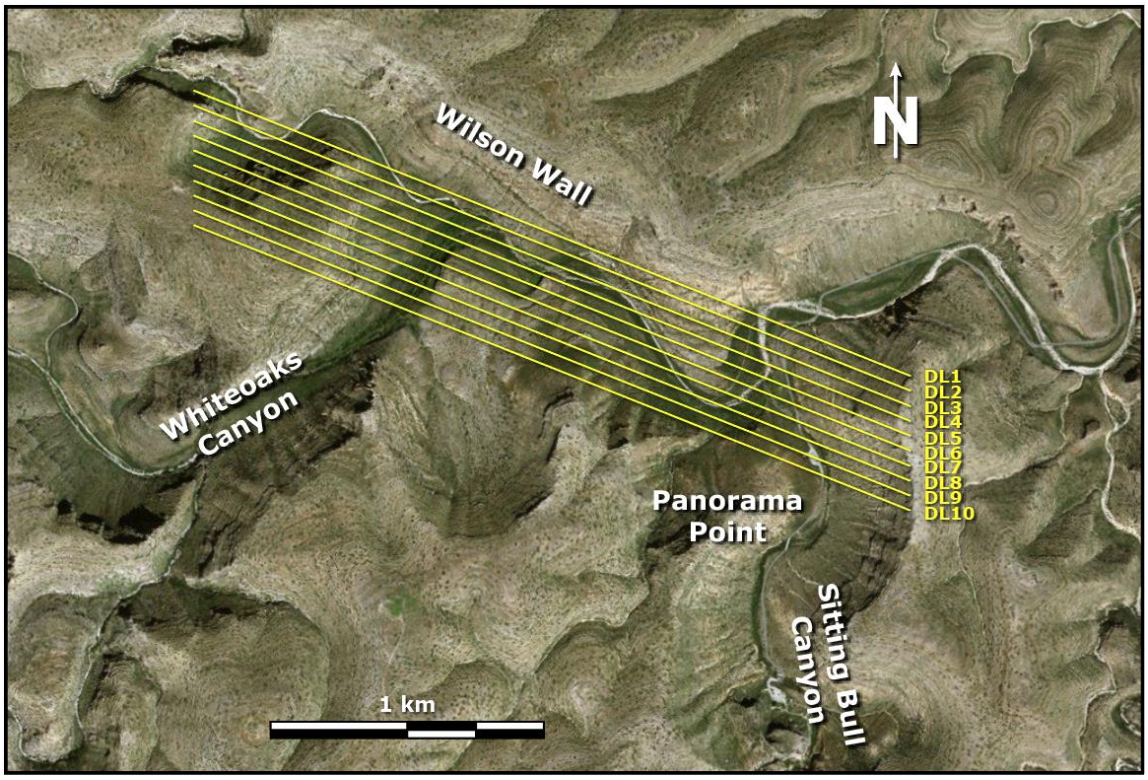

Figure AIII.1: Base map of the study area with the ten dip profiles for the measurement of lateral variability in clinoform progradation and aggradation.

Table AIII.1: Clinoform progradation.

Clinoform	S&C	DL 1	DL 2	DL 3	DL 4	DL 5	DL 6	DL 7	DL 8	DL 9	DL 10	Average	Max	Min
C1	30	231	254	244	222	203	175	146	131	136	147	189	254	131
C2	600	806	743	695	644	590	576	578	585	603	609	643	806	576
C3	420	395	407	393	404	407	398	484	636	680	681	488	681	393
C4	305	92	81	122	181	234	297	250	100	51	42	145	297	42
C5	355	16	12	5	10	15	23	113	193	244	278	91	278	5
C6	385	71	96	88	59	36	45	2	11	58	72	54	96	2

Table AIII.2: Clinoform aggradation.

Clinoform	S&C	DL 1	DL 2	DL 3	DL 4	DL 5	DL 6	DL 7	DL 8	DL 9	DL 10	Average	Max	Min
C1	10.0	9.6	9.8	10.9	12.3	12.7	13.0	13.2	13.2	13.6	14.5	12	14	10
C2	-3.0	-1.6	-1.8	-3.2	-3.6	-3.3	-3.1	-3.6	-3.4	-3.5	-3.1	-3	-2	-4
C3	2.7	1.7	0.2	-0.5	-2.2	-3.5	-4.1	-5.9	-8.6	-9.1	-9.0	-4	2	-9
C4	7.5	5.4	7.5	8.3	8.8	9.0	8.3	9.1	12.0	12.4	11.9	9	12	5
C5	-6.7	4.6	4.6	4.5	5.2	5.8	7.0	5.2	2.7	2.0	1.0	4	7	1
C6	2.0	1.0	1.3	2.3	2.9	3.2	3.1	6.0	7.3	5.5	4.7	4	7	1

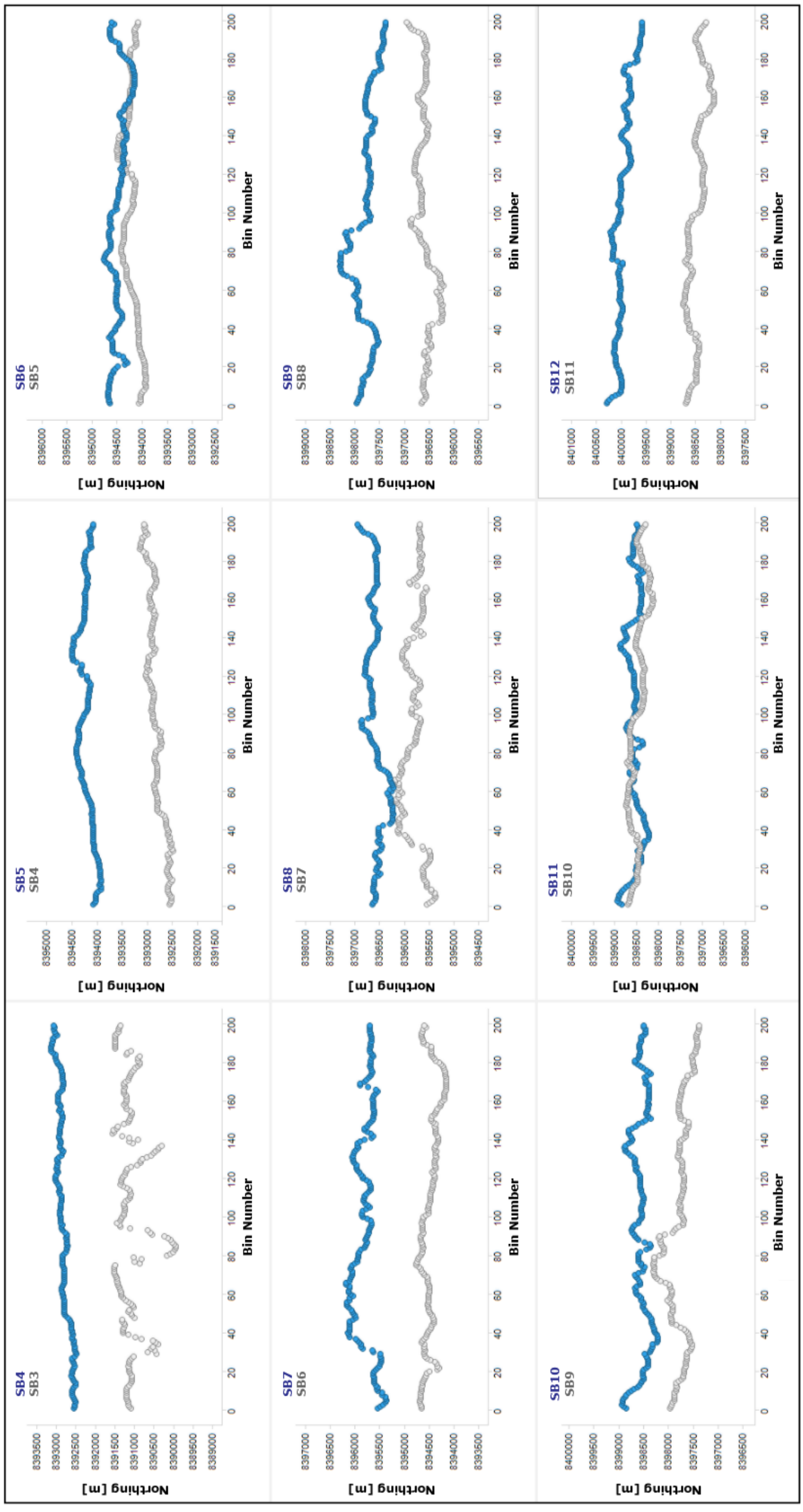

Figure AIV.1: Map view of shelf breaks SB3 to SB12.

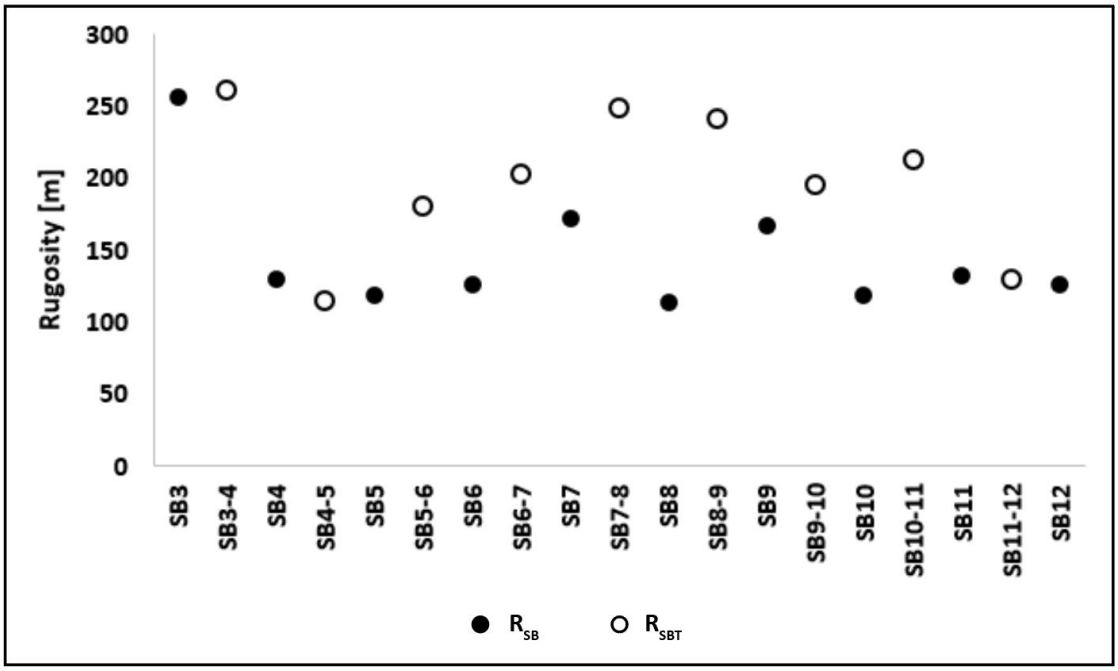

Figure AIV2: Rugosity of all shelf breaks and shelf break trajectories.

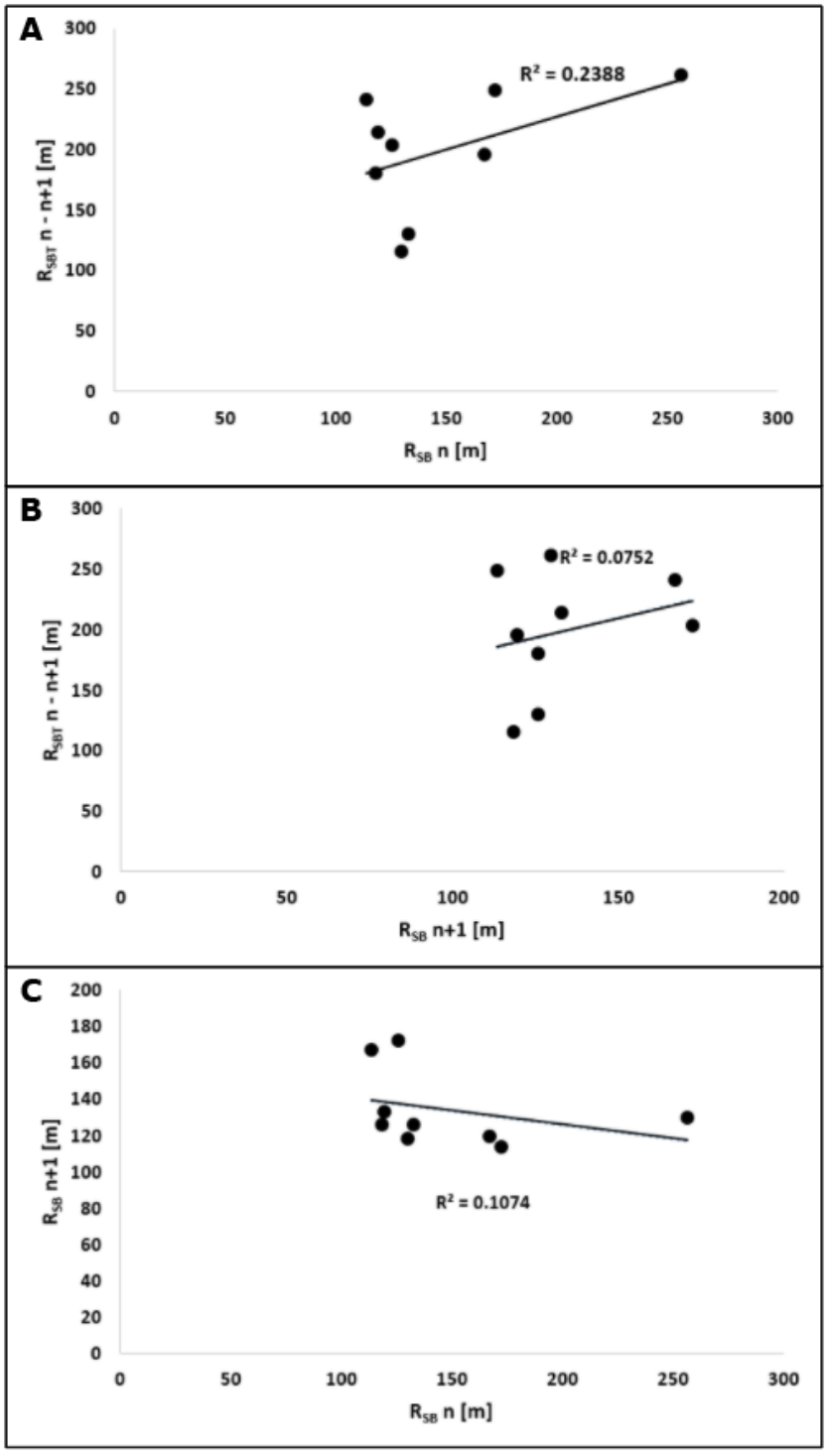

Figure AIV.3: Effect of RSB and RSBT on subsequent shelf breaks.

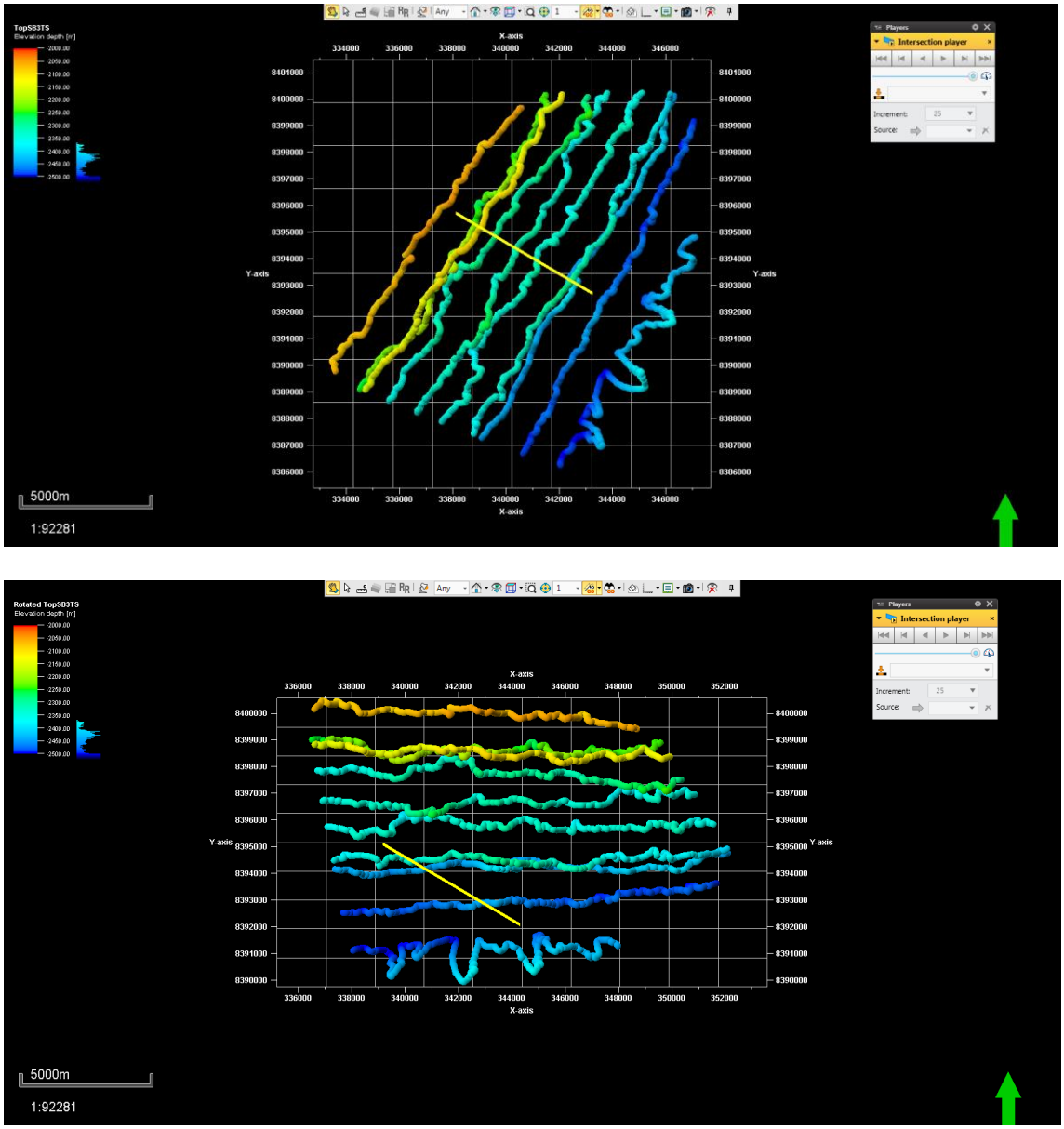

Figure AIV.4: Major changes in average shelf break orientation occur from SB5-6 and from SB9-10. This coincides with the slope channel re-organization phases of Tesch et al. (2018).